Investigating mechanisms behind invasive *Salmonella* infections using an intestinal organ-on-a-chip model

Nadia Baseer

Department of Biosciences
Faculty of Science
University of Sheffield

A thesis submitted in partial fulfilment of the requirements for the degree of Doctor of Philosophy

January 2024

Declaration

I confirm that this thesis is my own work. I am aware of the University's Guidance on the Use of Unfair Means (https://www.sheffield.ac.uk/new-students/unfair-means). This work has not previously been presented for an award at this, or any other university.

Nadia Baseer, January 2024

Acknowledgements

I'm grateful to God for connecting me with the right people at the right time, being my source of light, warmth and comfort in the happiest and most distressing times and guiding me in exploring this beautiful world and in developing a humbling perspective at the countless biological events that happen worldwide in consonance. Every biological experiment I've performed seemed to be a reminder that no matter how many extraneous variables I try to control for, there will always be more unknown factors that I haven't accounted for, but which would critically influence the outcome in an *in vivo* scenario. It has been a treat to realise just how marvellously our biological systems are able to function without us having to consciously check if all the variables are functioning in sync, for e.g. if we've taken enough breaths per minute, reabsorbed enough water in the nephrons of our kidneys back into our bloodstream or if our gut enzymes are being secreted well and in the right amounts during or after mealtimes.

It wouldn't be far-fetched to say it took a village to produce this thesis and complete my PhD journey. I am indebted to my parents, Mr Saiyed Mohammad Ali Baseer and Miss Rumza Farooqui, and siblings Mr Ebrahim Baseer, Miss Hafsa Baseer and Miss Maryam Baseer for their unwavering support, encouragement and love throughout my journey.

Many thanks to my supervisor Dr Daniel Humphreys, who helped me enjoy science despite the COVID-19 pandemic and developed my confidence and creativity as a researcher. Thank you for being amazingly patient with me and seeing my results as something exciting whenever I'd be stuck at a pessimistic pothole wondering if there was anything of worth in my data at all. Thank you for being available any time I had concerns about anything, for your enthusiasm, for providing great ideas and for

creative solutions to things I could have never thought of myself. I thoroughly enjoyed my time thanks to you!

Many thanks to past and present members of the Humphreys team, Dr Angela Ibler, Dr Kate Naylor, Dr Mohamed ElGhazaly, Dr Zhou Zhu, Dr Daniel Stark, Dr Salma Srour, Miss Michelle King, Miss Nataya Deans and Miss Francesca Brown for being patient with me ever since I started as a novice in the lab and teaching me so many cool techniques in science! Thank you for supporting me in innumerous ways, helping me develop critical thinking skills and for providing a safe environment to share thoughts and ideas in no matter how unintelligent they were. Thank you for being especially patient and understanding as I was finishing up, and for providing comfort whenever I felt despair about the future or the cost of living crisis or jobs or a million other things. Thank you for also reminding me to prioritise my mental health every time I was neglectful.

Many thanks to Dr Francesco Boccellato and Boccellato team members Dr Antonella D'Amore, Dr Diana Papp, Miss Claudia Zagami, Mr Jan Traulsen and Miss Camilla Persi at Ludwig, Oxford for hosting me for two months, providing colon organoid cultures, teaching me so many cool things about organoids and making my transition so easy there! Our lunches together and all the laughs and conversations we had despite limited time will always be precious to me.

Many thanks to my advisors, Prof Carl Smythe, Dr Kai Erdmann and my former advisor Prof Bazbek Davletov for supporting me with valuable input and timely advice—project and non-project related—that I couldn't have done without during this PhD.

Many thanks to Miss Weronika Buczek, Dr Hatoon Alamri, Dr Jorge Ferreira, Miss Xianhui Wei, Mr Yazeed Almukhlifi, Dr Alice Zhao, Dr Ola Shehata, Dr Bayan Samman, Miss Chiara Felicita, Dr Amani Alharbi, Miss Isabella Davis, Dr Trong Khoa Pham, Dr Mark Collins and Miss Taan for all the laughs, safe space for conversations, love and support that I couldn't have survived without.

Miss Sundus Jawed, Miss Mariyam Nasrin, Miss Safia Sanaad, Miss Mehvesh Shaikh, Miss Soaad Noman, Miss Tuba Khan, Miss Tuba Khanam, Miss Rabia

Omar—thank you for being amazing lifelines. There's so much you've done for me and given me even when we've been apart for several years!

Dr Heba Ansar, Mr Ali Zaid, Miss Fareeha Arshad, Miss Shabnam Narval, Miss Rekha Singh, Miss Yusra Ahmed, Miss Yusra Nadwi, Dr Oula ElAtat, Miss Asma Ansari, Dr Isra Siraj, Miss Reham Filfilan, Miss Rameeza Salman, Miss Aisha Adil and Dr Anas Adil, you've been absolute gems. I'm truly grateful for your kindness and support and for cheering me through.

Lastly, many thanks to Miss Carol Fordham and Miss Beckii Suttill for their invaluable support and advice towards the end of my PhD.

Abstract

Typhoidal *Salmonellae* establish disease by bypassing innate immune defences in the human gut. Unlike localised gut infections by non-typhoidal *Salmonellae*, typhoidal *Salmonellae* disseminate from the intestinal epithelium to sterile sites, causing a systemic infection that results in acute enteric fever. It is hypothesised that the typhoid toxin encoded by typhoidal *Salmonellae* activate host DNA damage responses (DDR) to manipulate innate gut defences, thereby facilitating *Salmonella* dissemination, yet the mechanisms are unresolved.

Previous studies on the typhoid toxin have been performed on 2D non-polarised human cell cultures, animal models and human challenge models. Human challenge models are subject to stringent regulations, which limit the extent of studies that can be performed and subsequent interpretations. On the other hand, typhoidal *Salmonella* are strict human pathogens and make animal models difficult to interpret. Using cultured human cells remains the most faithful way of studying host-pathogen interactions. However, 2D cell cultures do not account for the 3D polarised micro-environment *in vivo*.

This study sought to establish a 3D intestinal organ-on-a-chip model to elucidate host interactions with purified recombinant typhoid toxin. Multiple 3D gut-on-chips were developed using polarized intestinal epithelial cells such as Caco-2 and DLD-1 cells, and human primary intestinal cells from biopsy-derived colon organoids. Of these, the Caco-2 gut-on-chip was the most sensitive to the typhoid toxin. Toxin nuclease activity is known to activate DDRs that mediate cell-cycle arrest to enable repair. Indeed, toxin-induced DDR marked by γH2AX was observed in both non-polarized 2D Caco-2 cells and the 3D Caco-2 gut-on-chip system. Further

investigation through RNA sequencing revealed a divergence in the transcriptomes of 2D Caco-2 cells and the 3D Caco-2 gut-on-chip in response to the toxin, which was dependent on polarisation in the 3D Caco-2 gut-on-a-chip.

Interestingly, enrichment analyses of genes differentially regulated by the toxin in 2D Caco-2 cells showed cell cycle checkpoint and response to type I interferon as the two most significant biological processes associated with them. On the other hand, the two most significant processes associated with genes differentially regulated by the toxin in the 3D Caco-2 gut-on-chip were sterol biosynthetic process and cholesterol biosynthetic process. Nevertheless, toxin-induced DDRs were observed to reduce intracellular NTS *Salmonella* burden in both 3D and 2D Caco-2 models. Overall, findings in this PhD thesis reveal that the 3D environment of a system plays an important role in the transcriptional programs activated by the typhoid toxin, which may influence the ability of typhoidal *Salmonellae* to disseminate and establish systemic infections *in vivo*.

Table of Contents

List of Figures

List of Tables

List of Abbreviations

2D two-dimensional
3D three-dimensional
AIM2 absent in melanoma 2
AMP antimicrobial peptide
APH aphidicolin
APOL3 apolipoprotein L3
APS ammonium persulfate
ATM Ataxia Telangiectasia Mutated
ATR Ataxia telangiectasia and Rad3 related
BME β-mercaptoethanol
BSA bovine serum albumin
CDK cyclin-dependent kinase
CDKI cyclin-dependent kinase inhibitor
CFU colony forming unit
cGAS cyclic GMP-AMP synthase
CHK checkpoint kinase
CLR C-type lectin receptor
CST cell signalling technology
DABCO 1,4-Diazabicyclo [2.2.2]octane
DAMP damage-associated molecular pattern
DAPI 4′,6-diamidino-2-phenylindole
DDR DNA damage response
DMEM Dulbecco's Modified Eagle's medium
DMSO dimethyl sulfoxide
ECM extracellular matrix

EGF epidermal growth factor
ETP etoposide
FBS Foetal Bovine Serum
FCS Foetal Calf Serum
FGF fibroblast growth factor
GO gene ontology
GSDM gasdermin
HEPES 4- (2-hydroxyethyl)-1-piperazineethanesulfonic acid
HQ toxin catalytically inactive toxin with CdtB-H160Q mutation
IFIT interferon induced protein with tetratricopeptide repeat
IFN interferon
IGF insulin-like growth factor
IL interleukin
IMS industrial methylated spirit
IRF interferon regulatory factor
ISG interferon stimulated gene
LB lysogeny broth
LYZ lysozyme
MEM minimum essential medium
MES 2-(N-morpholino) ethanesulfonic acid
NAC N-acetyl-L-cysteine
NAIP NLR family apoptosis inhibitory protein
NLR NOD-like receptor
p38i p38 inhibitor
SB 202190 4-(4-Fluorophenyl)-2-(4-hydroxyphenyl)-5-(4-pyridyl)-1H-imidazole
PAMP pathogen-associated molecular pattern
PBS phospho-buffered saline
PFA paraformaldehylde
PGE2 prostaglandin E2
PRR pathogen recognition receptors
PVDF polyvinylidene difluoride
ROCKi rho kinase inhibitor
RPMI Roswell Park Memorial Institute Medium

Rspo1 R-Spondin 1

SDS-PAGE sodium dodecyl sulphate–polyacrylamide gel electrophoresis

siRNA short interfering ribonucleic acid

TBK1 tank-binding kinase

TBS tris-buffered saline

TEMED tetramethylethylenediamine

TLR toll-like receptor

WHO World Health Organisation

WT wild type

XDR extensively drug resistant

ZO-1 zonula occludens-1

γH2AX phosphorylated H2A histone family member X

Part I: Introduction

1. *Salmonella enterica*

1.1. Introduction to *Salmonella* serovars

Salmonella enterica is a highly evolved Gram-negative bacterial species that is classified into six subspecies, of which the most relevant to human disease is *S. enterica* subspecies *enterica* (Gal-Mor, 2019). About 1586 serovars or subtypes have been identified and distinguished under this subspecies (Gal-Mor, 2019) based on evolutionary differences in several surface antigens present on structures like lipopolysaccharide (LPS) and flagella (Yang *et al*. 2018). These pathogen serovars have shown to exhibit varied host specificity and disease outcomes, which defines their classification into two major groups: **typhoidal *Salmonella* serovars**, which invade sterile tissues at systemic sites (i.e., invasive disease), and **non-typhoidal *Salmonella*** serovars that cause non-invasive disease, i.e., gastroenteritis (Gal-Mor, 2019).

1.1.1. Non-Typhoidal serovars

The vast majority of *Salmonella* serovars belong to the non-typhoidal *Salmonella* (NTS) group and include serovars such as *S. enterica* subspecies *enterica* serovars Enteritidis (shortened to *S.* Enteritidis), *S.* Typhimurium, of which sequence type 19 (ST19) is best-studied, and *S.* Javiana (Gal-Mor, 2019). NTS infect a broad range of animal hosts to establish their reservoir, which results in zoonotic transmission from animal-to-humans where these pathogens cause acute gastroenteritis (Yang *et al*.

2018, Gal-Mor, 2019). NTS serovars are responsible for ~94 million cases of gastroenteritis infection worldwide annually and represent a significant global disease burden (Majowicz *et al*., 2010). NTS *Salmonellae* are mainly transmitted via contaminated food and initiate infection in the gastrointestinal tract (Gal-Mor, 2019).

1.1.2. Emergence of invasive NTS pathovariants

Most NTS serovars are restricted to the human gut by innate immune responses (Gal-Mor, 2019). The exceptions are human-adapted invasive NTS (iNTS) pathovariants such as anti-microbial resistant (AMR) *S.* Typhimurium ST313 that have emerged due the rise in malnourished and immunocompromised individuals, predominantly in sub-Saharan Africa due to the HIV epidemic, causing ~535,000 global cases annually (Stanaway, Parisi, *et al.,* 2019, Haselbeck *et al*., 2017). These iNTS infections are known to be associated with immunosuppressive diseases such as AIDS and sickle-cell disease (Turgeon *et al*., 2017). ST313 particularly causes an invasive typhoid-like disease in immunocompromised individuals resulting in high fatality rates of ~20% (Haselbeck *et al*., 2017, Stanaway, Parisi, *et al.,* 2019).

The invasive capacity of *S.* Typhimurium ST313 in humans is thought to be attributed to significant loss of bacterial genes found in *S.* Typhimurium ST19 that are associated with triggering host inflammatory responses, which enables ST313 to escape detection by the host immune system (Carden *et al*., 2015). Interestingly, the degraded genes align with those degraded in invasive typhoidal serovars (Carden *et al*., 2015). The ST313 strain also exhibits lower invasion of 3D intestinal cultures as compared to non-invasive NTS ST19 (Barrila *et al*., 2017), along with reduced activation of inflammatory responses and better survival and dissemination in human macrophages *in vitro* (Ramachandran *et al*., 2015). While ST313 bacteria are not known to cause an aggravated systemic infection in patients, there is significant bacteraemia observed which results in fever that is deadly to immunocompromised individuals (Haselbeck *et al*., 2017).

1.1.3. Typhoidal serovars

Typhoidal serovars such as *S.* Typhi and *S.* Paratyphi are human-restricted pathogens (Gal-Mor, 2019) that cause enteric fever (typhoid or paratyphoid fever) in

~27 million people worldwide annually (Stanaway, Reiner, *et al.,* 2019). Like iNTS, typhoidal serovars infect the intestine through contaminated food, after which they disseminate from the intestinal mucosa into the bloodstream causing bacteraemia (Gal-Mor, 2019). However, the bacteraemia is transient as these strains are highly evolved to cause systemic disease where chronic infections can be established in the liver and gallbladder (Yang *et al*. 2018).

1.2. Diagnosis and Treatment

1.2.1. Diagnosis

Current diagnostic tools in endemic regions rely on the clinical symptoms of *Salmonella* infections. However, misdiagnoses are common as the symptoms presented are similar to those observed in febrile illnesses such as malaria and dengue (Crump *et al*., 2015). Typically, blood, stool and urine samples are examined for the presence of *Salmonella* bacteria or their antigens (Gilman *et al*., 1975, Andrews and Ryan, 2015). Bacterial presence is tested by culturing samples in bacterial growth medium such as Lysogeny broth (LB) or LB agar. On the other hand, antigen presence from destroyed *Salmonellae* can be detected via antibody tests such as Widal's Test, where host antibodies circulating in the patient's serum are tested for their reactivity to lipopolysaccharide (O) and flagellar (H) antigens of dead *Salmonellae* (Andrews and Ryan, 2015). However, during early onset of invasive infections such as enteric fever, both tests lack sensitivity for low counts of typhoidal *Salmonella* in blood cultures, especially if patients have been pre-treated with antibiotics (Wain *et al*., 2001, Parry *et al*., 2002). Bone marrow examinations are highly sensitive to bacterial counts, as typhoidal *Salmonellae* are known to localize in the bone marrow during systemic infection and withstand antibiotics (Hussein Gasem *et al*., 1995; Wain *et al*., 2001). Even so, bone marrow extraction is a highly invasive procedure requiring sophisticated equipment and medical personnel trained in sterile technique that are not always available to patients in low-resource settings where enteric fever is endemic. As a result, development of new tools for identifying enteric fever is currently a WHO research priority (World Health Organization, 2018).

1.2.2. Treatment and antibiotic resistance

NTS infections do not require treatment, however, immunocompromised individuals are highly susceptible to disease complications and death due enhanced invasion by NTS, and are treated with antibiotics such as ciprofloxacin, ceftriaxone and ampicillin (Gal-Mor *et al*., 2014, Gut *et al*., 2018). Typhoidal infections, on the other hand, are promptly treated with first-line antibiotics such as cefixime, cefotaxime and ceftriaxone, or second-line antibiotics such as chloramphenicol, trimethoprim with sulfamethoxazole (TMP-SMX), amoxicillin, azithromycin and aztreonam (Kumar and Kumar, 2017).

Unfortunately, the emergence of extensively drug resistant (XDR) strains of typhoidal *Salmonella* has led to treatment failures and difficulties in disease control and management, as these strains display resistance to several antibiotics such as ampicillin, TMP-SMX, chloramphenicol, fluoroquinolones and third generation cephalosporins (Yang, Chong and Song, 2018). With limited treatment options and increased transmission between patients (Walker *et al*., 2023), XDR typhoidal infections are increasing rapidly and are currently classified as a highly-priority threat by the WHO (Tacconelli *et al*., 2018).

1.2.3. Vaccination

Besides antibiotic treatment, vaccines are currently being used as preventive measures for invasive typhoidal infections. There are three vaccines currently licensed by the WHO for enteric fever – a typhoid conjugate vaccine (TCV), unconjugated Vi polysaccharide (ViPS) and a live vaccine (Ty21A) (World Health Organization, 2018).

The TCV vaccine consists of a Vi polysaccharide antigen of typhoidal *S*. Typhi in addition to a tetanus toxoid, which is used to prime the host immune system against future typhoidal infections (Mitra *et al*., 2016). In the case of adults, TCVs were shown to have an efficacy of 54.6% against all symptoms of typhoid fever during clinical trials in the UK (Jin *et al*., 2017). However, TCVs were observed to be particularly safe and effective in Nepalese and Indian children younger than 12 years and older than 6 months, with an efficacy between 81.6% and 100% during clinical trials (Mitra *et al*., 2016, Shakya *et al*., 2019).

The unconjugated ViPS vaccine provides 45-69% protection for 2 years after vaccination (Milligan *et al*., 2018), while Ty21A, a live attenuated strain of *S*. Typhi without virulence genes or the Vi capsule, provides an efficacy of 62-96% for at least 3 years post vaccination (World Health Organization, 2018). However, improvements in diagnostics and treatments are necessary as vaccination alone is not sufficient to eradicate typhoidal infections (Pitzer *et al*., 2014).

Thus, in order to discover novel ways to combat invasive typhoidal infections, we must first develop an understanding of the disease mechanisms involved in NTS and typhoidal infections.

1.3. Pathogenesis

The mechanism of pathogenicity for both NTS and typhoidal serovars is controlled by genomic segments called *Salmonella* pathogenicity islands (SPIs), 17 of which have been recognised to date (Kombade and Kaur, 2021). Virulence genes on SPI-1 and 2 specifically promote bacterial entry into host cells and intracellular survival in M cells in the lymphoid Peyer's patches or non-phagocytic enterocytes **(Fig. 1.0)** (Ribet and Cossart, 2015, Dougan and Baker, 2014, Velge *et al*., 2012). *Salmonellae* utilise a needle-like appendage encoded by SPI-1 known as the type III secretion system (T3SS-1), which injects bacterial effector proteins into target cells (Winter *et al*., 2014). These effectors in turn enable host membrane ruffling and actin cytoskeleton remodelling to facilitate the macropinocytosis of adherent *Salmonellae* (Lorkowski *et al*., 2014, Fàbrega and Vila, 2013). For example, the SPI-1 effector SopE activates Rho GTPases Rac1 and Cdc42 to promote membrane ruffling and *Salmonella* entry (Hardt *et al*., 1998). The T3SS-2 secretion system encoded by SPI-2, on the other hand, helps in the establishment of an endosome called *Salmonella*-Containing Vacuole (SCV) inside host cells and basolateral transcytosis to the lamina propria (Gal-Mor, 2019). For example, the SPI-2 effector SifA is required for maintaining SCV integrity and a *sifA* null mutant strain of *Salmonella* is released into the host cell cytoplasm (Beuzón *et al*., 2002). Thus, T3SS-1/2 inject cocktails of effector proteins into host cells to manipulate cell biology and facilitate intracellular infection and *Salmonella* survival (Agbor and McCormick, 2011).

However, upon entry into host cells, NTS and typhoidal serovars exhibit differences in their disease outcomes based on the host immune defences activated by pathogen invasion.

.

2. Innate immune responses to *Salmonella*

2.1. Introduction to innate immunity

The innate immune system orchestrates the first line of defence against pathogens upon cellular invasion. In contrast to adaptive immune responses which are delayed and involve the production of tailored B and T lymphocytes towards antigens, innate immune responses are rapid and non-specific. The signalling cascade begins when pathogen recognition receptors (PRRs) expressed by host cells discover pathogen-associated molecular patterns (PAMPs) or mammalian damage-associated molecular patterns (DAMPs) released during infection (Broz and Monack, 2013). Upon binding PAMPs or DAMPs, PRRs can activate several signalling pathways to initiate defences against invading pathogens.

2.1.1. Types of PRRs

Several PRRs have been identified and classified based on their structure, binding preferences for ligands and the cellular compartments they are localized in (Platnich and Muruve, 2019). These include Toll-like receptors (TLRs), C-type lectin receptors (CLRs) and cytosolic PRRs.

TLRs and CLRs are membrane-bound receptors that detect extracellular PAMPs such as LPS and flagellin in bacteria and β-glucans in yeast, while cytoplasmic PRRs include proteins such as absent in melanoma 2 (AIM2) and cyclic GMP-AMP synthase (cGAS) which detect cytosolic PAMPs/DAMPs such as pathogen DNA or damaged host DNA, respectively (Broz and Monack, 2013). The NOD-like receptor (NLR) family forms the largest group among cytoplasmic PRRs and is further classified into sub-

families based on modifications in their N-terminal, the most well-known being the NLRC and NLRP groups of proteins (Broz and Monack, 2013).

Certain PRRs activate transcription factors such as NF-κB and interferon regulatory factors (IRFs) to promote the secretion of cytokines such as interferons (IFNs) and interleukins (ILs) via the conventional ER-Golgi protein transport system (Broz and Monack, 2013, Phulphagar *et al.,* 2021). Other PRRs promote the production of inflammatory caspases by recruiting a multi-protein complex called the inflammasome, causing unconventional release of leaderless cytokines and alarmins via a lytic form of cell death called pyroptosis (Broz and Dixit, 2016). While it is not very clear how different routes of cytokine secretion, i.e., conventional and unconventional secretion affect paracrine responses, the recruitment of immune cells by pro-inflammatory cytokines from the infection niche helps in restricting pathogenic activity and mediating the adaptive immune response (Phulphagar *et al.,* 2021, Broz and Monack, 2013).

2.1.2. Activation of the inflammasome

Among all discovered PRRs, only a few are known to be implicated in inflammasome activation and assembly, such as pyrin, NLRP3, NLRC4, AIM2 and NLRP1 (Broz and Dixit, 2016).

The canonical inflammasome is a multimeric complex that comprises an activated PRR such as NLRC4, an adaptor protein for PRRs lacking a CARD domain and the effector protein pro-caspase-1 (Man *et al.,* 2014, Platnich and Muruve, 2019). In human macrophages, the NLRC4 inflammasome is activated by the human NLR family apoptosis inhibitory protein (NAIP) which senses proteins such as *Salmonella* flagellin (Kortmann *et al.,* 2015), while the AIM2 inflammasome is activated by AIM2 detection of double-stranded DNA in the cytosol (Platnich and Muruve, 2019). Cleaved caspase-1 generated by these canonical inflammasomes regulates the maturation of cytokines such as IL-1β and IL-18 and cleaves the pore-forming protein Gasdermin D (GSDMD) to promote plasma membrane perforation (Zito *et al.*, 2020). This leads to an inflammatory form of cell death called pyroptosis (Zito *et al.*, 2020).

Some canonical inflammasomes such as that of NLRP3 require two signals for activation (Zito *et al.*, 2020). A priming signal initiated by PAMPs such as extracellular LPS activates TLR-4, triggering pro-IL-1β and NLRP3 production via the NF-κB signalling pathway, while the second signal induces NLRP3 inflammasome assembly and caspase-1 cleavage (Bauernfeind *et al.*, 2009, Zito *et al.*, 2020). The second signal can be triggered by cellular processes such as organelle rupture, potassium efflux, generation of reactive oxygen species (ROS) and release of mitochondrial DAMPs due to diverse stimuli such as ATP (Platnich and Muruve, 2019). However, low cytosolic potassium has been reported to be crucial and sufficient for activating NLRP3 inflammasome assembly in mouse bone-marrow derived macrophages (Muñoz-Planillo *et al.*, 2013).

2.1.3. Interferons and their role in antimicrobial responses

Interferons are a group of cytokines secreted by infected or damaged cells that were first reported to interfere with viral replication (Isaacs and Lindenmann, 1988). Interferons are classified as type I, II and III interferons, and are responsible for interacting with bystander cells to enhance host defences against pathogens (Alphonse, Dickenson and Odendall, 2021). Some of these defence measures include immune cell recruitment, protection of epithelial barriers from damage, inhibition of bacterial replication and inhibition of bacterial migration through epithelial barriers (Ivashkiv, 2018, Alphonse, Dickenson and Odendall, 2021).

Type I, II and III IFN production can be mediated by a wide array of PRRs such as AIM2, the AIM2-like receptor (ALR) IFI16, cGAS, and several other TLRs and NLRs (Boxx and Cheng, 2016, Dunphy *et al.*, 2018, Li and Wu, 2021, Ka *et al.*, 2021). Upon activation by PAMPs or DAMPs, PRRs such as cGAS and IFI16 activate the adaptor protein STING (stimulator for interferon genes), which in turn recruits the IRF kinase TBK1 (Decout *et al.*, 2021, Ka *et al.*, 2021). Subsequently, TBK1 phosphorylates the transcription factor IRF3 to initiate IRF3 dimerization, nuclear translocation and type I interferon gene expression (Decout *et al.*, 2021, Ka *et al.*, 2021). Other cytoplasmic PRRs such as Ku70 have been reported to stimulate the production of type III IFNs through IRF1 and IRF7 (Zhang *et al.*, 2011).

Upon secretion from infected cells, interferons bind with distinct receptor complexes on the cell surface of bystander cells to trigger a signalling cascade that leads to the expression of interferon stimulated genes (ISGs) (Schneider, Chevillotte and Rice 2014). ISGs are a pool of more than 300 genes, several of which are known to be involved in inflammasome signalling, such as the PRR AIM2 (Man *et al*., 2015, Alphonse, Dickenson and Odendall, 2021). ISGs such as ISG15 have been reported to restrict *Listeria* infection in non-phagocytic mammalian cells (Radoshevich *et al*., 2015). The IFIT (Interferon-induced tetrapeptide repeat) family of ISGs, consisting of IFIT1, IFIT1, IFIT3 and IFIT5 have been reported to play diverse and conflicting roles such as restriction of viral replication, cellular aging, cancer suppression and cancer progression (Zhou *et al*., 2013, Vladimer *et al*., 2014, Kreienkamp *et al*., 2018, Pidugu *et al.,* 2019, Zhang *et al*., 2023).

Besides interferon and inflammasome responses, certain cells in the human intestine such as neutrophils and epithelial cells secrete anti-microbial peptides (AMPs) in response to infection (Fu *et al*., 2023, Lueschow and McElroy, 2020). Human anti-microbial peptides consist of two main families, defensins and cathelicidins, both of which exert anti-microbial activity against Gram-negative and Gram-positive bacteria (Lueschow and McElroy, 2020, Fu *et al*., 2023, van Harten *et al*., 2018). Several α- and β-defensin genes have been identified in humans, whereas the *hCAP-18* gene is the only known cathelicidin gene in humans (Dhaliwal, Bajaj-Elliott and Kelly, 2003, van Harten *et al*., 2018). Together, these AMPs exhibit diverse biological functions, including bactericidal activity, regulation of autoimmunity, immunomodulation of innate and adaptive immunity and immune cell recruitment (Fu *et al*., 2023, van Harten *et al*., 2018).

2.2. Innate immune responses during NTS infection

PAMPs such as T3SS1/2 effectors and flagellin released from NTS *Salmonella* have been reported to initiate inflammasome activation and subsequent pyroptosis in human colonic epithelial monolayers (Knodler *et al*., 2010). Additionally, PRRs such as NLRC4 have been shown to promote defence against NTS invasion and restrict early infection in the mouse intestinal epithelium (Sellin *et al*., 2014, Rauch *et al.,* 2017).

In a mouse infection model, NTS *S*. Typhimurium with persistent expression of flagellin were shown to cause pyroptosis in macrophages (Miao *et al*., 2010) (**Fig 1.0**). The expelled bacteria from these dying macrophages were then eliminated by neutrophils through the production of reactive oxygen species (Miao *et al*., 2010). In immunocompetent individuals, NTS *Salmonellae* cause rapid gastroenteritis, wherein the course of infection is largely symptomatic, inflammatory and self-limiting (Gal-Mor, 2019, Yang *et al*., 2018).

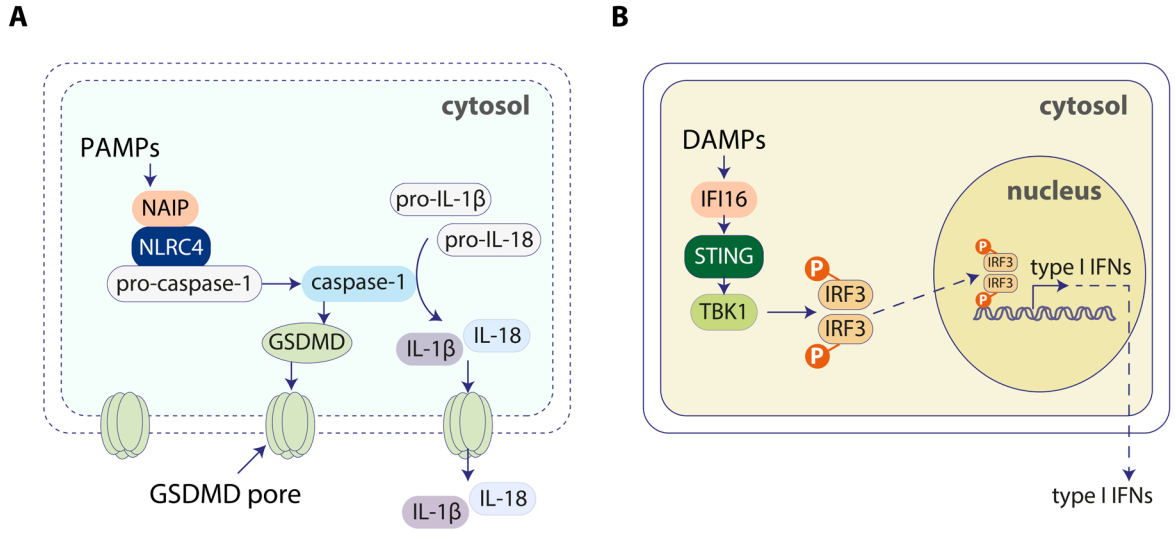

Figure 1.0 Innate immune responses activated by PAMPs or DAMPs during cellular invasion. (**A**) The NLRC4 inflammasome is activated by the PAMP sensor NAIP (Kortmann *et al*., 2015), which leads to the maturation of caspase-1 from its precursor pro-caspase-1 (Zito *et al*., 2020). Caspase-1 is responsible for cleaving gasdermins such as gasdermin D (GSDMD) to initiate gasdermin pore formation, as well as maturation of the cytokines IL-1β and IL-18 (Zito *et al*., 2020). Cytokines are eventually secreted through the gasdermin pores and the cell undergoes a lytic form of cell death called pyroptosis (Zito *et al*., 2020). (**B**) DAMPs arising from damaged host DNA can activate sensors such as IFI16, which activates the adaptor protein STING (Ka *et al*., 2021). STING in turn phosphorylates the IRF kinase TBK1, which phosphorylates IRF3, causing its dimerization, nuclear translocation and the expression of type I IFNs (Ka *et al*., 2021).

2.3. Innate immune responses during typhoidal infection

S. Typhi entry and infection into the intestinal epithelium is similar to that of other *Salmonella* serovars, except upon invasion of the lamina propria, it does not activate the inflammatory response or cause recruitment of sentinel immune cells (Gal-Mor,

2019, Wangdi *et al*., 2012). This is because genome degradation in *S.* Typhi has caused 50% of T3SS secreted effector genes to become pseudogenes or absent entirely, particularly NTS genes implicated in inflammation and animal infection (Yang *et al*. 2018). Moreover, *S.* Typhi has also acquired additional unique virulence factors that are not expressed by prototype NTS serovars, such as the Vi Capsular Polysaccharide (ViCPS), also known as the Vi Antigen. The Vi Capsule is responsible for several anti-inflammatory activities including downregulation of T3SS-1 and flagellar protein expression and blocking detection of inflammasome-activating PAMPs such as LPS and flagellin by toll-like receptors TLR4 and TLR5 (Wangdi *et al*., 2012, Winter *et al*, 2014, Yang *et al*. 2018).

The lack of innate immune detection favours *S.* Typhi in invading the lymphoid tissue and infecting macrophages (Wangdi *et al*., 2012), allowing dissemination to other systemic sites and causing persistent infection **(Fig. 1.1)** (Dougan and Baker, 2014). Nevertheless, how typhoidal infections subvert immune responses in the intestine to spread systemically is yet to be understood.

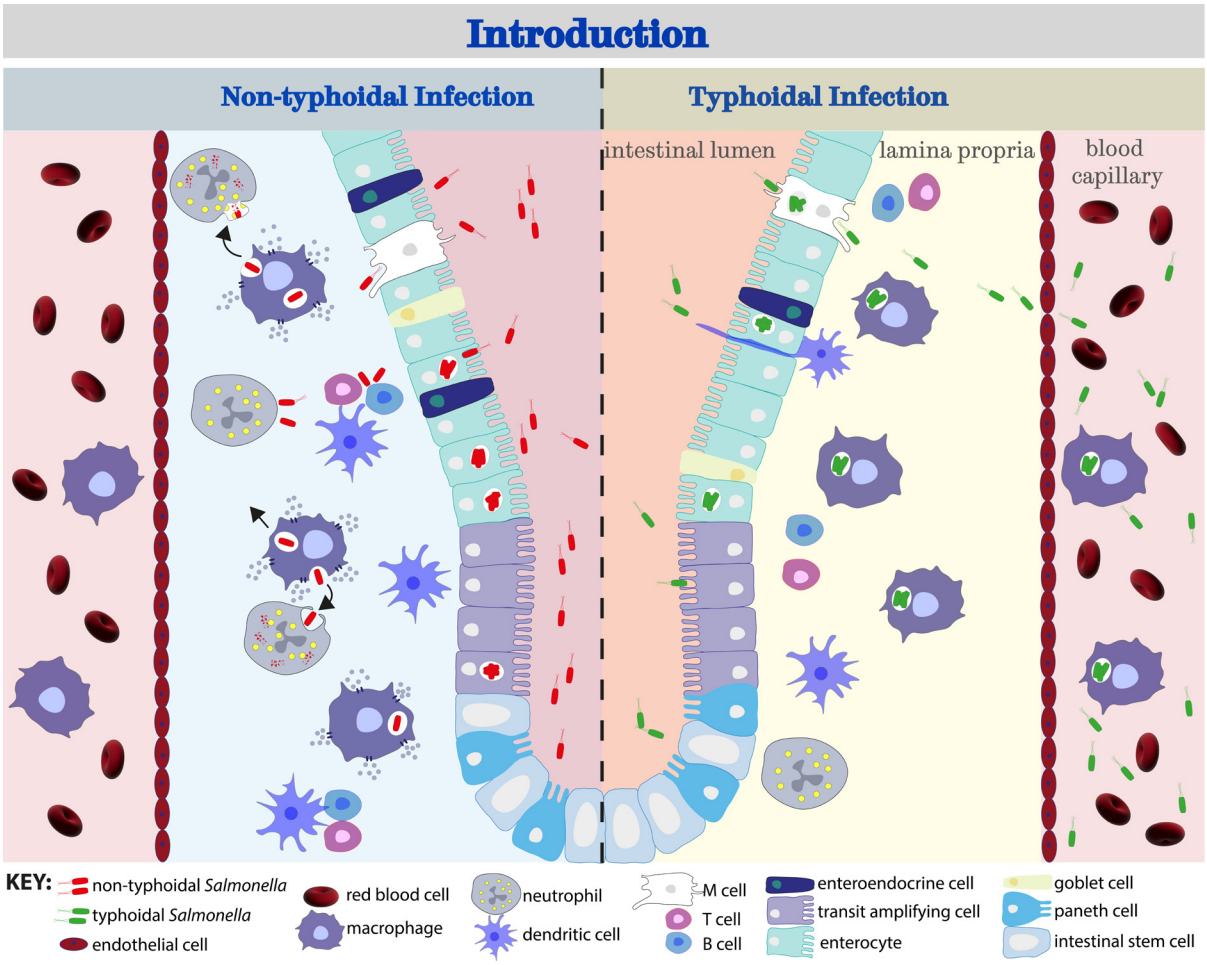

Figure 1.1 Non-typhoidal versus typhoidal *Salmonella* infections. NTS strains such as *S.* Typhimurium activate the innate immune response due to their inflammatory components such as flagellin which serve as PAMPs to the inflammasome (Knodler *et al.*, 2010). The bacteria are phagocytosed by neutrophils (Miao *et al.*, 2010) and are unable to spread systemically, remaining restricted to the gut (Gal-Mor, 2019). *S.* Typhi has modified its genome to exclude most inflammatory genes expressed in NTS serovars, and with the help of virulence factors such ViCPS and typhoid toxin, it escapes detection by the innate immune defences and spreads systemically to cause enteric fever (Yang *et al.* 2018, Gal-Mor, 2019).

3. The typhoid toxin

The virulence factor ViCPS is expressed by *S.* Typhi but not *S.* Paratyphi A, which also causes enteric fever. A major virulence factor encoded by both strains however is the typhoid toxin (Galán, 2016).

3.1. Structure, secretion and entry into host cells

Structure. The typhoid toxin belongs to the family of secreted AB exotoxins, where 'A' stands for the 'active' subunit and 'B' represents the receptor binding subunit (Song *et al*., 2013). In comparison to other AB toxins, the typhoid toxin is composed of two A subunits – Cytolethal distending toxin B (CdtB) and Pertussis-like toxin A (PltA), and one B subunit – Pertussis-like toxin B (PltB) (Song *et al*., 2013). Typhoidal CdtB is homologous to the CdtB subunit of a broad family of bacterial genotoxins known as cytolethal distending toxin (CDTs) that are bound to two B subunits, CdtA and CdtC (Lara-Tejero and Galán, 2001, 2002). Another important aspect of CdtB is its structural and functional homology with the nuclease Deoxyribonuclease I (DNase I) due to similarities in their enzymatic activities (Lara-Tejero and Galán, 2000).

The PltA subunit possesses ADP-ribosylase activity, but no function has been ascribed (Spano *et al*., 2008). Instead, the PltA appears to be a linker subunit bridging PltB to the toxigenic subunit CdtB (Spano *et al*., 2008). Following toxin uptake, disulphide bonds linking PltA to CdtB are reduced, which liberates the CdtB (Spano *et al*., 2008, Song *et al*., 2013). CdtB subsequently undergoes retrograde transport via the Golgi after which the CdtB localises to the nucleus where it exerts its toxigenic effects (Guidi *et al*., 2013).

Secretion. The typhoid toxin is expressed by *S.* Typhi inside the endosome called SCV in infected cells (Spano *et al*., 2008). Upon secretion, the toxin is packaged into vesicle carrier intermediates or outer membrane vesicles (OMVs) derived from the SCV (Guidi *et al*., 2013). Toxin PltB preferentially binds with high-affinity to Neu5Ac-sialylated glycans on host cell surface receptors (Yu *et al*., 2007). PltB binding of Neu5Ac receptors in the OMVs enables toxin packaging, while mutation in *PltB* or lack of Neu5Ac receptors abrogates successful packaging and export of the toxin into the extracellular milieu (Chang, Song and Galán, 2016). Subsequently, OMVs containing the toxin fuse with the plasma membrane via SNARE proteins VAMP7, SNAP23, and Syntaxin 4, resulting in toxin exocytosis (Chang *et al*., 2022).

Internalisation in the host cell. Cellular entry of the toxin is mediated by PltB binding with Neu5Ac receptors on the target cell's surface, whereupon typhoid toxin undergoes receptor-mediated endocytosis (Spano *et al*., 2008, Song *et al*., 2013). The toxin is trafficked via retrograde transport from the Golgi apparatus to the endoplasmic reticulum (Chang *et al*., 2019). Subsequently, the CdtB subunit is released from PltA by host reductases, allowing it to target the nucleus and exert its nuclease activity (Chang *et al*., 2019, Ibler *et al.,* 2019).

Toxin interactions with cell surface receptors. Neu5Ac receptors are abundantly found in the human gut and brain and are predominantly expressed in humans due to a lack of the enzyme CMP-N-acetylneuraminic acid hydroxylase (CMAH), which is responsible for modifying Neu5Ac to Neu5Gc glycans (Schnaar *et al*., 2014, Bell *et al*., 2023, Chou *et al*., 2002). However, small amounts of Neu5Gc receptors can be expressed in human cell cultures upon supplementing growth media with Neu5Gc (Deng *et al*., 2014). In mice, tissues with functional CMAH have both Neu5Gc and Neu5Ac receptors, while other mammals such as chimpanzees primarily have Neu5Gc receptors (Hedlund *et al*., 2007). As the typhoid toxin induces cytotoxicity in cells expressing Neu5Ac surface receptors but not Neu5Gc receptors, it is highly specific for cells with predominant Neu5Ac expression (Deng *et al*., 2014). Additionally, cellular targets for intoxication are not limited to bystander uninfected cells but can also include infected cells in the milieu (Spano *et al*., 2008, Chong *et al*., 2017). Amongst the ~2000 NTS serovars, 54 contain genes for the typhoid toxin (den Bakker *et al*., 2011), of which, the best-studied is *S.* Javiana. Interestingly, the PltB

subunits of typhoidal and Clade B NTS serovars such as *S.* Javiana exhibit 1% amino acid sequence variation, which determines glycan binding preferences and tissue tropism: the PltB in Clade B NTS serovars favour intoxication of intestinal cells, whereas the PltB of typhoidal serovars is more promiscuous with a broad tropism including cells at systemic infection sites (Lee *et al*., 2020).

3.2. Role of the typhoid toxin

Toxigenic effects were initially studied in animal models by injecting 10 µg of purified recombinant typhoid toxin into mice (Song *et al.,* 2013). The CdtB subunit of the toxin induced typhoid fever symptoms and a 100% fatality, as opposed to the mutant derivative of the toxin encoding a H160Q mutation in *cdtB* (Song *et al.,* 2013). This suggests that high concentrations of typhoid toxin promote typhoid fever symptoms. Mutation of the ADP-ribosylase activity of PltA had no effect on mouse fatality while mutation of PltB impaired toxin binding to Neu5Ac-modified glycans, which impeded toxin uptake and toxicity (Song *et al.,* 2013). However, infection experiments with toxin-expressing *Salmonella* in human and animal models consistently show that the toxin protects the host from pathology arising from gut inflammation, thereby enabling invasive, asymptomatic and chronic infections by stealth (Song *et al*., 2013, Del Bel Belluz, *et al.,* 2016, Gibani *et al*., 2019). Studies conducted by Del Bel Belluz *et al.* in 2016 showed that when the typhoid toxin islet was expressed in *S*. Typhimurium, the engineered pathogen reduced intestinal inflammation in mice, thereby promoting host survival and chronic asymptomatic infections at systemic sites. This is also consistent with related CDTs, which promote persistent infections by *Campylobacter* and *Helicobacter* species (Scuron *et al*., 2016). In human infection challenge studies with wild-type *S.* Typhi and a mutant toxin-null strain, *S.* Typhi caused a more aggressive typhoid fever (for e.g., increase in antibody secreting cells, longer duration of bacteraemia) in the absence of the toxin (Gibani *et al*., 2019). Similarly, the pathology score in mice infected with wild-type *S.* Javiana was reduced in comparison to toxin-null *ΔcdtB S.* Javiana (Miller *et al*., 2018).

In summary, conflicting reports make the role of the toxin unclear, however infection experiments point to an immunosuppressive role mediated via unknown mechanisms. What is consistent is that the effects of typhoid toxin are dependent upon

the nuclease activity of CdtB that activates the host DNA damage response (DDR), which is introduced below.

3.2.1. Introduction to cell cycle regulation and the DDR

Cell cycle regulation. A full cycle of cell division comprises 4 phases, G1, S, G2 and M phase. During the course of a cell cycle, the E2F family of proteins regulate transcriptional activation and repression, and together with cyclins and cyclin-dependant kinases (CDKs), play an important role in cell cycle progression (Kent and Leone, 2019, Hume *et al.,* 2020, Fagundes and Teixeira, 2021, Henley and Dick, 2012).

During G0 phase, all E2F factors are inactivated by the Retinoblastoma protein (Rb) and associated pocket proteins (Kent and Leone, 2019). However, in cells progressing through early G1, the cyclin D-CDK4/6 complex inactivates pocket proteins such as Rb via hyperphosphorylation, allowing E2F transcription factors to detach from them (Hume *et al.,* 2020, Kent and Leone, 2019). Repressor E2Fs such as E2F4 and E2F5 are shuttled to the cytoplasm in late G1, while E2F1, E2F2 and E2F3 activate target genes crucial for S phase entry and maintaining Rb hyperphosphorylation (Hume *et al.,* 2020, Kent and Leone, 2019), such as cyclin E (Fagundes and Teixeira, 2021, Henley and Dick, 2012). Increase in cyclin E production causes increased cyclin E-CDK2 complex activity as well as Rb hyperphosphorylation, leading to cell cycle progression (Henley and Dick, 2012) (**Fig. 1.2**). Indeed, silencing of cyclin E gene *CCNE1* has been implicated in cell cycle arrest in patient-derived gastric carcinoma samples (Zhang *et al.,* 2019).

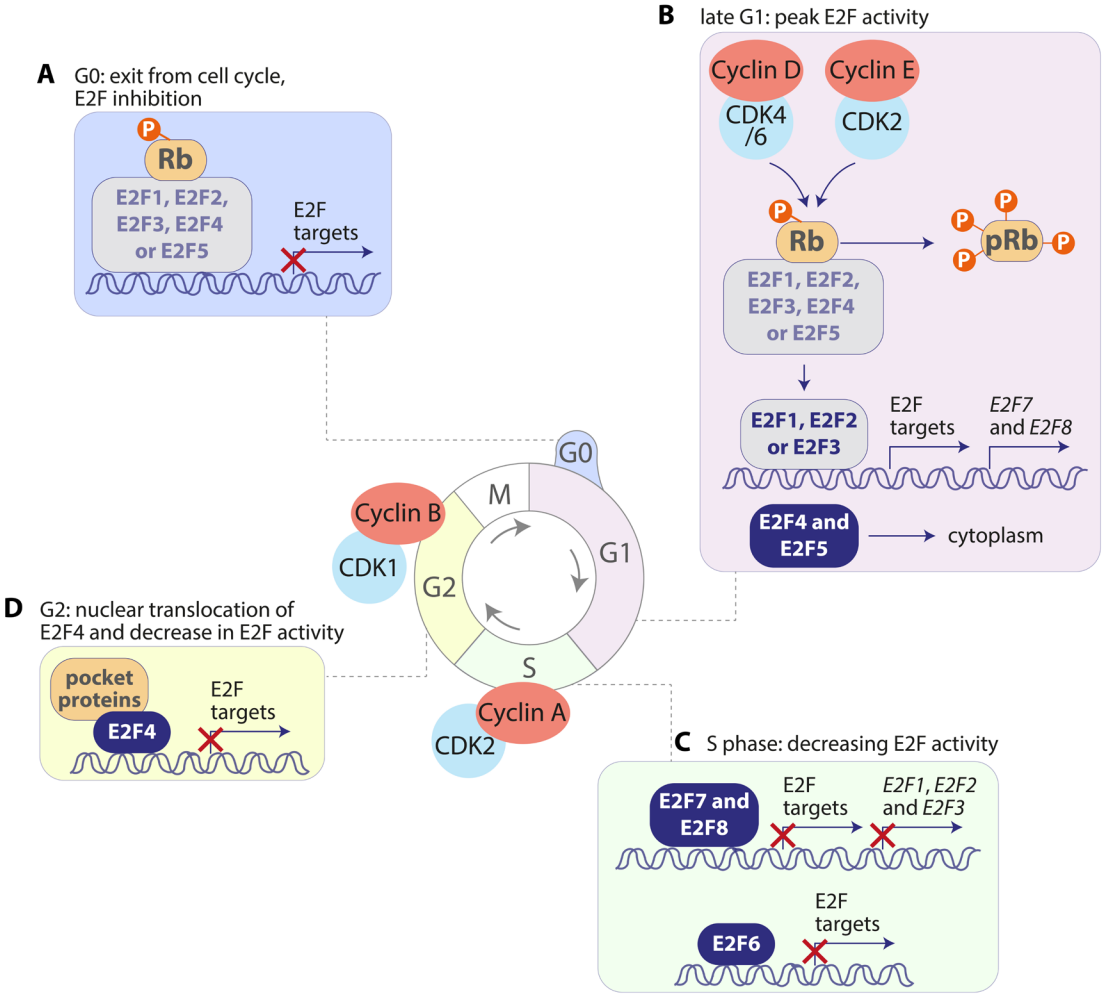

Figure 1.2 E2F regulation through the cell cycle. (**A**) G0 phase: all E2F factors are inhibited by pocket proteins such as Rb, p107 and p130 (Trimarchi and Lees, 2002, Kent and Leone, 2019). (**B**) late G1 phase: pocket proteins such as Rb are phosphorylated during early G1 by the cyclinD-CDK4/6 complex, and hyperphosphorylated at late G1 by cyclinE-CDK2, causing their inactivation and detachment from E2Fs (Hume *et al.*, 2020, Kent and Leone, 2019). Repressors E2F4 and E2F5 are shuttled to the cytoplasm, while activators E2F1, E2F2 and E2F3 bind to target promoters to initiate transcription of G1-S phase genes, including *E2F7* and *E2F8* (Hume *et al.*, 2020, Kent and Leone, 2019). (**C**) S phase: E2F6, E2F7 and E2F8 levels increase and repress the transcription of E2F targets, including *E2F1*, *E2F2* and *E2F3* (Kent and Leone, 2019). (**D**) G2 phase: E2F4 and E2F5 are shuttled back to the nucleus by pocket proteins to further repress E2F-target genes (Kent and Leone, 2019).

During S phase regulation by cyclin A2-CDK2 complex (Sherr and Roberts, 2004), transcriptional repression, particularly *E2F1*, *E2F2* and *E2F3* repression is mediated by E2F7 and E2F8 (Kent and Leone, 2019). As the cell cycle progresses towards late

G2 phase and until re-entry into G1 phase, E2F4 and E2F5 are shuttled from the cytoplasm to the nucleus to further repress E2F-target genes (Kent and Leone, 2019).

However, in the event of DNA damage during G1/S phase, for example, inhibition of CDKs by CDK inhibitors (CDKIs) leads to Rb dephosphorylation, resulting in E2F inactivation by Rb and blockage of S-phase entry (Hume *et al.*, 2020) (**Fig. 1.3**).

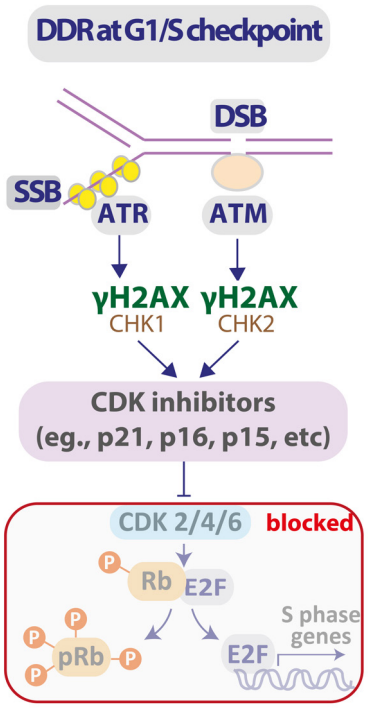

Figure 1.3 DNA damage response at the G1/S cell cycle checkpoint. ATR is recruited to single-stranded DNA breaks, while ATM is recruited to double-stranded DNA breaks during DNA damage (Cimprich and Cortez, 2008, Jazayeri *et al.*, 2006). Besides histone H2AX, ATR and ATM also phosphorylate checkpoint kinases CHK1 and CHK2 respectively (Burma *et al.*, 2001, Cimprich and Cortez, 2008). CHK1 and CHK2 in turn activate CDK inhibitors to prevent Rb hyperphosphorylation, E2F activation and G1/S progression, leading to cell cycle arrest (Abuetabh *et al.*, 2022, Cimprich and Cortez, 2008, Deshpande, Sicinski and Hinds, 2005).

DNA damage response. Genomic damage can occur during everyday cellular activities such as DNA replication and metabolism, and by environmental agents such as radiation and chemical genotoxins (Polo and Jackson, 2011). This damage is mitigated by the DDR which is an orchestrated pathway comprising various apical kinases, mediators and effectors that organize DNA replication, repair, cell-cycle

progression and cell-fate events such as apoptosis in the event of genomic damage (Cimprich and Cortez, 2008).

Two of these important apical kinases are the Ataxia-Telangiectasia Mutated (ATM) and ATM and RAD3-related (ATR) kinases. ATR responds to and mediates the repair of single-stranded breaks (SSBs) of DNA, while ATM mediates the repair of double-stranded DNA breaks (DSBs) (Cimprich and Cortez, 2008, Jazayeri *et al*., 2006).

ATR and ATM kinases phosphorylate the histone protein H2AX at serine 139 to form γH2AX, a prominent DDR marker which initiates the recruitment of repair proteins and cell cycle regulators at sites of DNA damage (Burma *et al*., 2001). Besides phosphorylating H2AX at sites of DNA breaks, ATM and ATR also phosphorylate checkpoint kinases CHK1 and CHK2 (Cimprich and Cortez, 2008). These checkpoint kinases phosphorylate the tumour suppressor p53, which in turn activates CDKIs such as $p21^{Cip1/Waf1}$ to initiate cellular arrest and repair (Abuetabh *et al*., 2022, Cimprich and Cortez, 2008, Deshpande, Sicinski and Hinds, 2005).

3.2.2. Typhoid toxin activates the DDR

The typhoid toxin inflicts extensive DNA damage in replicating cells via the catalytic H160 residue of CdtB, causing DDR activation marked by γH2AX foci, p53 phosphorylation, cellular distension and cell-cycle arrest (ElGhazaly *et al*., 2023, Ibler *et al.,* 2019, Spano *et al.,* 2008, Guidi *et al.,* 2013). These observations go in line with several reports regarding toxin expressing NTS strains (Miller *et al.,* 2018, Guidi *et al.,* 2013) and other bacterial CDTs such as *Haemophilus ducreyi* CDT and *E. coli* CDT that also generate γH2AX foci and induce cell cycle arrest via their CdtB DNase I activity in human cell cultures (Guerra *et al.,* 2011, Fedor *et al*., 2013).

Experiments by Ibler *et al* in 2019 showed that toxin-induced damage in replicating fibroblasts caused replication stress as well as the phosphorylation of ATR, ATM and CHK1. In intestinal cells, this damage stimulated the release of a host secretome containing signalling proteins such as Wnt5a and GDF15, which promoted cell survival, infections of macrophages and paracrine DNA damage in bystander cells (ElGhazaly *et al*., 2023). This supports the view that toxin-induced DDRs can influence

the fate of neighbouring un-intoxicated cells, and can influence the microenvironment across an infection niche, as has been observed in mice infected with toxin-producing NTS *S.* Typhimurium (Martin *et al*., 2021). Additionally, it is interesting to hypothesise that the toxin hijacks host immunity by promoting macrophage infection in order to further *S*. Typhi dissemination from the intestinal mucosa to secondary infection sites via the bloodstream.

3.3. Host-pathogen interaction studies in *Salmonella* infections using 3D tissue culture

The intestinal mucosa represents a barrier to all *Salmonella* serovars and must be penetrated to establish invasive infections. Consequently, intestinal cells represent an important defence against infectious disease. *Salmonella* invasion of the intestinal epithelium was first observed in guinea pigs following infection by *S.* Typhimurium by electron microscopy (Takeuchi, 1967). Infection of cultured mammalian epithelial cells paved the way for landmark discoveries by the laboratory of Stanley Falkow, revealing the requirement of *Salmonella* proteins for invasion into host cells (Finlay *et al*., 1989). This opened up a new field focussed on discovering the identity and role of the *Salmonella* proteins, which include the effector substrates of SPI-1 and SPI-2 T3SSs.

The race for new discoveries on the basis of *Salmonella* infections has been assisted by the advancement in experimental models, which includes the use of three-dimensional (3D) tissue culture. This has several advantages over cells cultured in two dimension (2D), such as replicating tissue architectures, complexity, morphology and mechanistic properties normally found *in vivo*. This is especially important when studying human pathogens such as typhoidal serovars of *Salmonella* and other human-restricted bacterial pathogens (e.g., *Shigella*), where studies in animal models may not be possible or difficult to interpret in the context of human pathology. For example, in comparison to 2D human cell cultures, CMAH knockout mice can mimic the complexity of the gut, present abundant Neu5Ac receptors, and are good models of acute *S*. Typhi infection, but not chronic *S*. Typhi infection typically seen in humans due to low mouse survival rates (Hedlund *et al*., 2007, Deng *et al*., 2014). On the other hand, chronic *S*. Typhi infection can be modelled using humanised mouse models

engrafted with human hematopoietic stem cells (Song *et al*., 2010). However, it is difficult to interpret the role of human immune cells in systemic *S*. Typhi pathology in such models as interactions between human cytokines and mouse tissues is limited (Song *et al*., 2010). Human challenge models are another alternative for studying *Salmonella* infections, however, they are subject to stringent regulations, which limit infection times, infection doses and subsequent interpretations (Gibani *et al*., 2019).

Studies in human donor-derived primary intestinal organoids have shown *S*. Typhimurium to successfully establish intracellular replication and propagate infection into the organoid lumen (Geiser *et al*., 2021). Additionally, in hiPSC (human induced pluripotent stem cell)-derived intestinal organoids, pre-treatment with recombinant human IL-22 was shown to reduce *S*. Typhimurium invasion into the epithelium (Lees *et al*., 2019). Studies in human donor-derived primary gallbladder organoids have also shown toxin-expressing *S*. Paratyphi to induce significantly more DNA damage in cells located paracrine to the site of infection than toxin-null *S*. Paratyphi (Sepe *et al*., 2020). In summary, the use of organoids has led to several advancements in our understanding of *Salmonella* host-pathogen interactions. However, gut organoids require sophisticated equipment to microinject pathogens into their lumen, as opposed to static 2D cultures which can be infected much more easily as the cells and their surfaces are more accessible to bacteria for invasion (Geiser *et al*., 2021, Ibler *et al*., 2019).

Primary gut-on-chips using primary cells isolated from intestinal organoids and grown on platforms such as the 3-lane OrganoPlate® provide luminar access to growth media and pathogens and can be co-cultured with immune or endothelial cells. As a result, primary gut-on-chips are an emerging tool for modelling gastrointestinal disease such as IBD (Beaurivage *et al*., 2020).

3.4. Aims and hypothesis

Given the emerging role of the typhoid toxin in promoting systemic infections and manipulating innate immune responses (Song *et al*., 2013, Lee *et al*., 2020, Del Bel Belluz, *et al.,* 2016), it is interesting to hypothesize that the toxin manipulates innate defences to promote *Salmonella* dissemination from the intestinal mucosa. This would

establish innate immunity as a hijack target of typhoidal *Salmonellae* and toxin-expressing NTS serovars. Infection of mice with *S.* Typhimurium expressing typhoid toxin has shed light on the potential role of typhoid toxin in chronic infection (Del Belluz *et al*., 2016). However, interpreting these findings are difficult and studying how typhoidal *Salmonellae* manipulate the intestinal mucosa is challenging as typhoidal *Salmonellae* are human-restricted pathogens (Gal-Mor, 2019). One approach is to exploit 3D tissue culture that can be performed with human cells and mimics many aspects of the human intestinal mucosa. 3D tissue culture has not previously been used to study the interaction between typhoid toxin and human intestinal cells, which may provide insight into host responses to the typhoid toxin.

This thesis aimed to:

1. Establish a 3D intestinal organ-on-chip model.
2. Investigate DNA damage responses induced by the typhoid toxin in an intestinal organ-on-chip model.
3. Investigate the effect of the toxin on *Salmonella* survival in 2D and 3D intestinal models.

Part II: Results

4. Developing an intestinal organ-on-chip model

4.1. Introduction

Many discoveries have been made in the field of host-pathogen interactions using animal models and human cell cultures, but there are limitations. For example, 2D cultures cannot easily reproduce the tissue organization and polarization observed in 3D culture models that mimic the micro-environment in *in vivo* tissues, as they are static in nature and do not employ fluid flow or perfusion. Animal models, on the other hand, can account for such complexities. However, they cannot replicate the pathogenesis of human-restricted diseases due to fundamental physiological and genetic differences as discussed in the previous sections. Consequentially, results generated from animal models cannot always be extended to human studies. For example, the typhoid toxin was initially shown to trigger typhoid fever symptoms in mice (Song *et al.,* 2013). However, Gibani *et al.* (2019) discovered using a human infection challenge study that the toxin was in fact not implicated in inducing typhoid fever symptoms.

3D organ-on-a-chip systems have recently emerged as a model of choice for studying human disease and performing drug trials due to their ability to recreate tissue organization and function *in vivo* using human cell lines (Edmondson *et al.,* 2014). Microfluidics enables these cultures to be supported with the extracellular

matrix, nutrients and fluid flow, and subsequently manipulated for infection and disease development (Edmondson *et al.,* 2014).

3D organ-on-a-chip systems have not previously been used to model host DNA damage responses to bacterial pathogens. It is possible, likely even, that host cell polarization and tissue organisation influence responses to the typhoid toxin of *Salmonella* Typhi. Thus, the primary aim of this project was to establish a gut-on-chip model using adenocarcinoma or primary intestinal cells, before testing their susceptibility to the typhoid toxin and *Salmonella* invasion.

4.2. Results

4.2.1. A gut-on-chip system using Caco-2 cells

Caco-2 cells are human adenocarcinoma cells that polarize upon growing to confluence and exhibit enterocyte-like behaviour (Natoli *et al.,* 2011). This model was developed due to the ease of culturing Caco-2 cells, short doubling time in comparison to primary cells from colon organoids and their robustness and high survival rate in the OrganoPlate® 3-lane 40 system (**Fig. 4.0 A**). The OrganoPlate® 3-lane 40 (henceforth OrganoPlate®) consists of 40 individual chips, each containing three channels, that can be used to grow at least 40 gut-on-chip models (**Fig. 4.0 B**).

The middle channel of each chip in the OrganoPlate® was first seeded with the extracellular matrix (ECM) comprising 4 mg/ml rat-tail collagen I, 0.1M HEPES and 3.7g/L $NaHCO_3$ to support the attachment, growth, and polarization of cells as per manufacturer's instructions (**Fig. 4.0 C**). Once the ECM had polymerized, cells were seeded the next day in the top cell seeding channel and allowed to sediment on the ECM to accelerate attachment (**Fig. 4.0 D**). After 2 hours, the plate was placed on a rocker and perfused with growth medium every 8 minutes at a 7° angle to allow three-dimensional growth of the cells into tubes (**Fig. 4.0 E**). After three days with no medium change, the tubes were perfused with 150 kDa FITC-dextran and had acquired leakproof barrier function (**Fig. 4.0 F**).

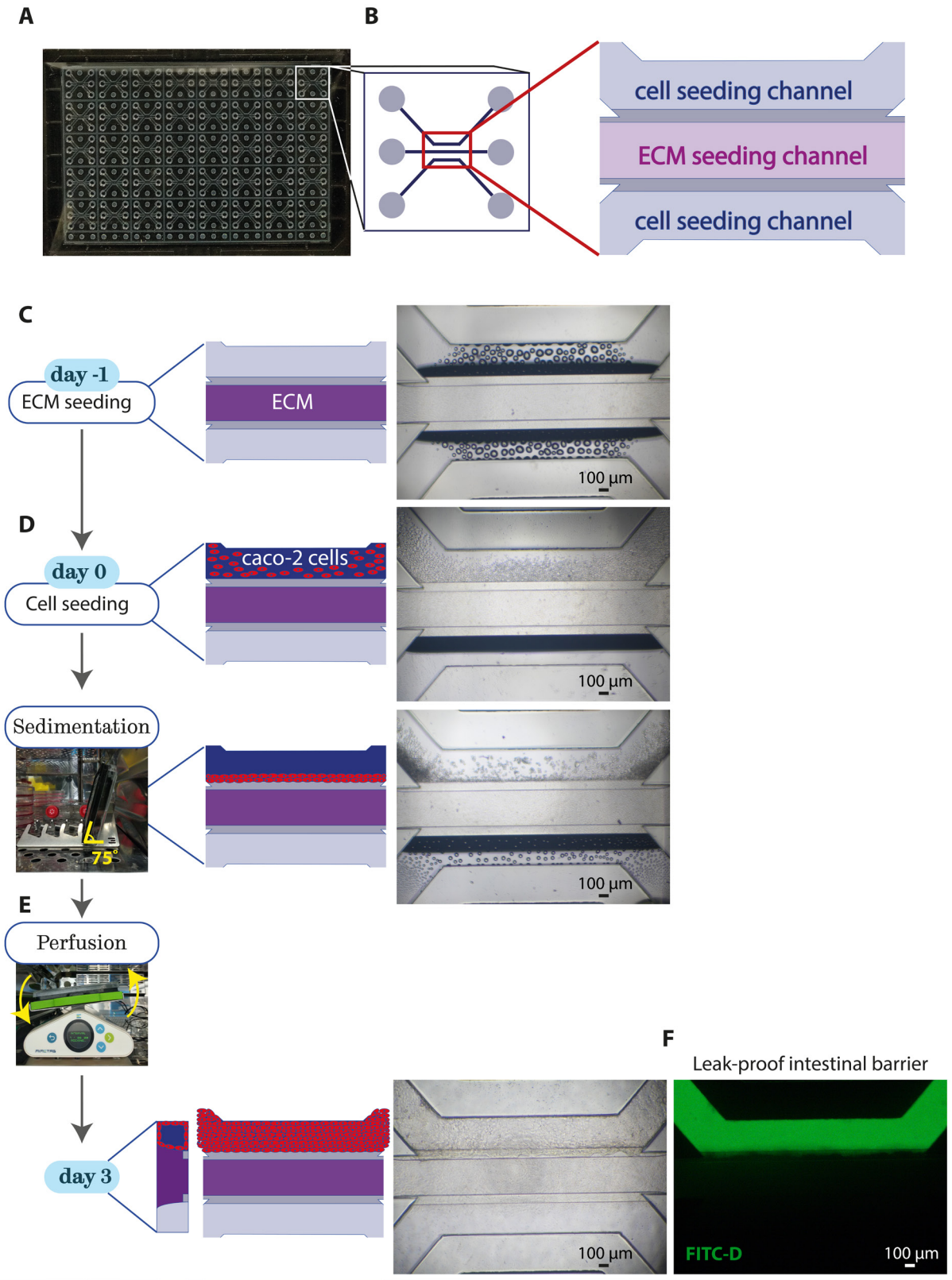

Figure 4.0 Schematic for 3D culture. (**A**) The Organoplate® 3-lane 40 consists of 40 microfluidic chips. (**B**) Diagram of a chip with three seeding channels or lanes. (**C**) The ECM is seeded and polymerized in the middle channel (with the help of guide barriers on each side of the channel) a day before cell seeding. (**D**) Once Caco-2 cells have been seeded, they are allowed to sediment

on to the ECM for a few hours by placing the plate at a 75° angle in the culture incubator. (**E**) Once cells have attached, the plate is moved to the Organoplate® rocker for perfusion at 7° every 8 minutes. The perfusion enabled by the rocking motion promotes three-dimensional growth as depicted in the cross-sectional view of the chip. (**F**) Fluorescence image at day 3 showing a leak-proof Caco-2 tube after perfusion with 150 kDa of FITC-Dextran dye for at least 30 minutes. The dye remains within the Caco-2 tube instead of leaking through it into other channels in the chip. Images are representative of at least three biological replicates and at least three technical replicates.

4.2.2. Optimising barrier function in Caco-2 tubes

Initially, ECM seeding and optimal barrier function of Caco-2 gut-on-chips proved to be challenging (**Fig. 4.1**), prompting several optimizations. To address incomplete filling of the middle ECM channel (**Fig. 4.1 A**), ECM seeding volumes were increased from 2 µl to 2.4 µl per chip. As the microfluidic channels in the OrganoPlate® operate on capillary action, 20 µl filtered pipette tips were used to prevent disruptions in capillary forces and incorrect seeding. Despite this, problems were encountered in developing and maintaining barrier function of the Caco-2 tubes until day 5, with frequent cellular invasion in the ECM (**Fig. 4.1 B, purple arrow**).

Since the ECM plays a crucial role in the growth and barrier function of the tubes, it was hypothesized that improper ECM polymerization may be affecting tube development. As a result, ECM components such as HEPES and $NaHCO_3$ solution were filter-sterilized after preparation, stored at -20°C and thawed only once to minimize pH alterations. Besides this, ECM components were mixed thoroughly before seeding to prevent uneven polymerization of fibres and cellular invasion. Additionally, Caco-2 growth medium was switched from high glucose to low glucose to reduce their potential of invading the ECM, all of which improved the development of Caco-2 tubes and increased their barrier function to day 5 post cell seeding (**Fig. 4.1 C**).

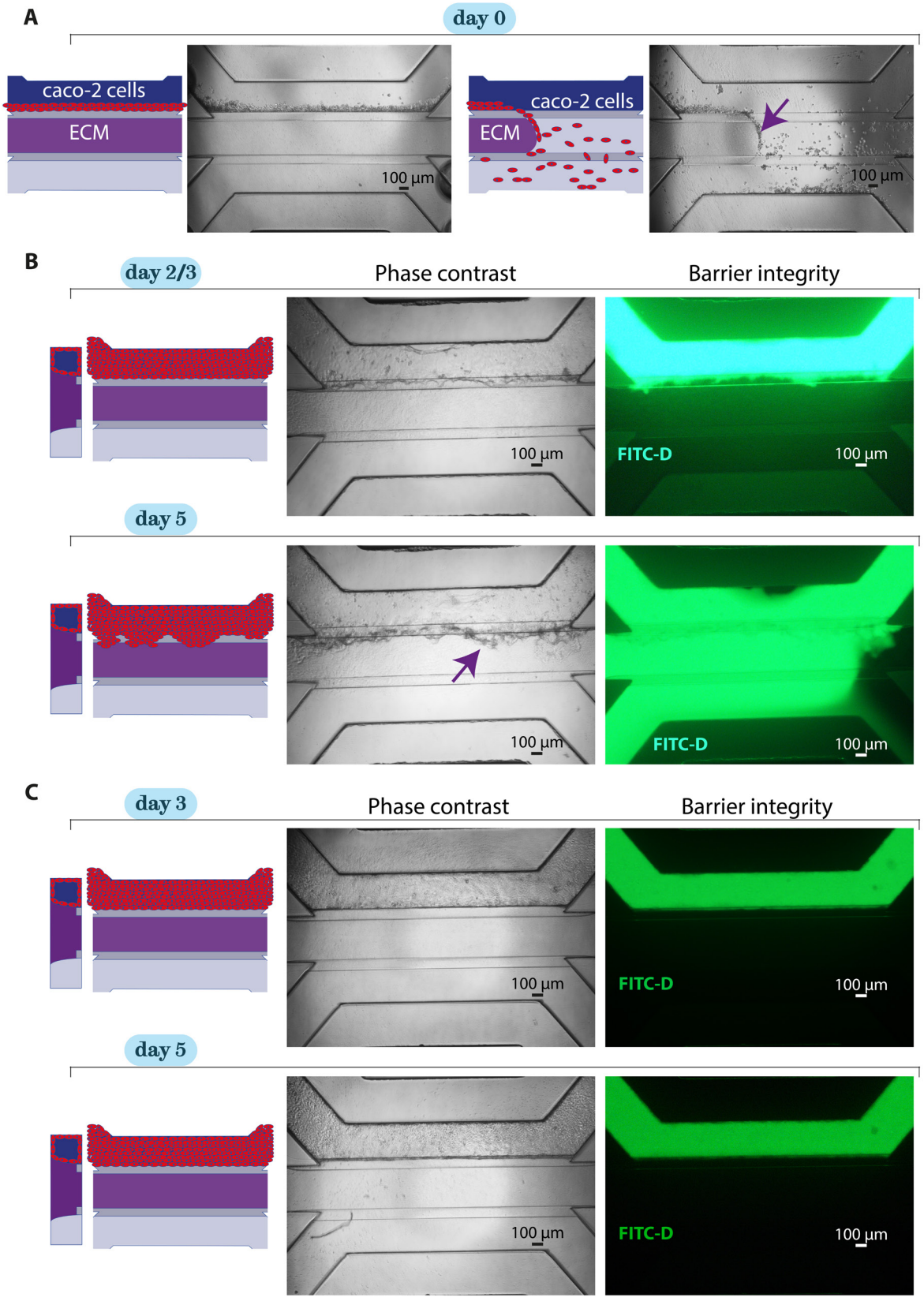

Figure 4.1 Problems encountered during 3D culture of Caco-2 tubes. (**A**) Phase contrast images showing incomplete filling of the middle channel with ECM at day 0. (**B**) Phase contrast images of a tube at day 2 and day 5 post cell seeding, along with fluorescence images of the same

tube perfused with 150 kDa FITC-dextran (green) at day 3 and day 5 post cell seeding. Cellular invasion in ECM indicated with purple arrow. (**C**) Phase contrast and fluorescence images of a tube perfused with 150 kDa FITC-dextran (green) at day 3 and day 5 post cell seeding after optimising culture conditions. All images are representative of at least three biological replicates.

4.2.3. Caco-2 tubes express polarization markers upon developing barrier function

Caco-2 gut-on-chips have previously been reported to exhibit polarization markers (Trietsch *et al.,* 2017). Indeed, upon attaining barrier function at day 3, tubes were observed to express tight junction proteins such as ZO-1 and form microtubules (characterized by acetylated α-tubulin) in a manner similar to what is observed in typical polarized epithelial cells (**Fig. 4.2**) (Bellett *et al.,* 2009, Dogterom and Koenderink, 2019, Trietsch *et al.,* 2017). However, apical-basal polarity as well as the presence of protrusions such as microvilli and cilia were difficult to interpret from the acetylated α-tubulin staining (**Fig. 4.2**).

4.2.4. Typhoid toxin induces DNA damage in Caco-2 tubes

To examine typhoid toxin activity in Caco-2 tubes, it was necessary to first understand how 2D Caco-2 cultures respond to the toxin. This was to determine the toxin concentration that would induce DNA damage in 2D Caco-2 cells and to elucidate if the same concentration would evoke DNA damage in 3D Caco-2 tubes. Additionally, optimising toxin activity in 2D Caco-2 cells first was more cost-effective than in 3D Caco-2 tubes.

The typhoid toxin was first purified from *E. coli* BL21 by Dr Daniel Humphreys as previously described (Ibler *et al*., 2019). As purified wild-type toxin ($toxin^{WT}$) can contain protein contaminants from *E. coli*, a DNase mutant derivative of the toxin encoding a H160Q mutation in *cdtB* ($toxin^{HQ}$) was also purified and used as a control for the effects of these contaminants, as well as the activities of PltB and PltA.

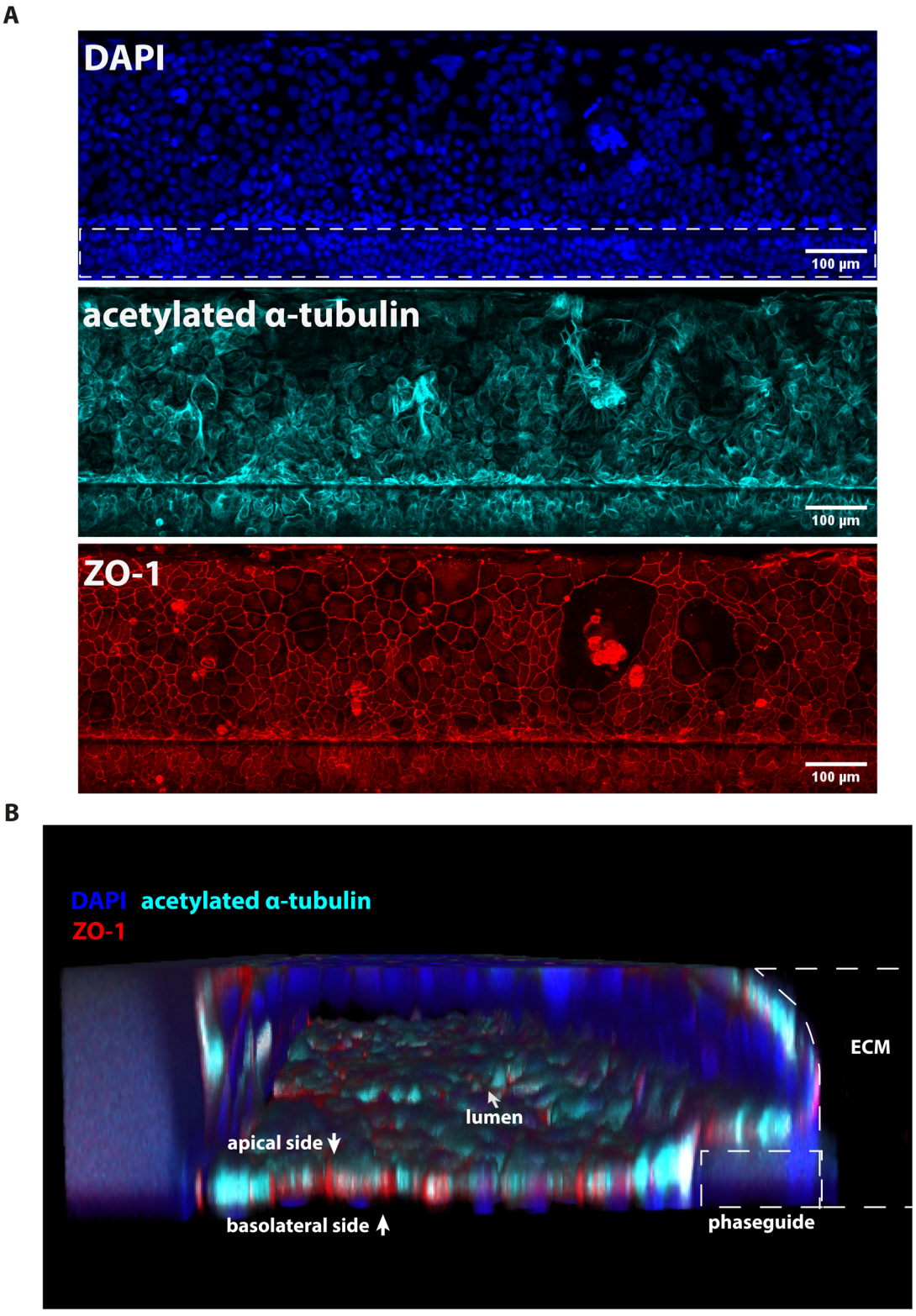

Figure 4.2 Caco-2 tubes express epithelial polarization markers. (**A**) Maximum intensity projections of confocal Z stacks showing intestinal tubes at day 3 stained for nuclei (DAPI), tight junctions (ZO-1) and microtubules (acetylated α-tubulin). Scale bars are 100 µm. (**B**) 3D reconstruction of the Z stacks in (**A**), showing apical and basolateral sides of the tube with a lumen. Phaseguide (a rectangular separator running parallel between the ECM and tube) is depicted by

dashed white rectangle in (**B**) and (**A**). Images are representative of at least three biological replicates (n=3).

Given the toxin^{WT} is known to cause H2AX phosphorylation at serine 139 (γH2AX) upon DNA damage in mammalian cells (**Fig. 4.3 A**) (Ibler *et al.*, 2019, Guidi *et al.*, 2013), γH2AX was used to assess toxin^{WT}-induced DDRs in Caco-2 cells. To begin with, Caco-2 cells were first seeded on plastic tissue culture plates at 30% confluency pre-coated with rat-tail Collagen I and allowed to recover overnight. The next day (day 1), cells were incubated with toxin^{WT} or toxin^{HQ} according to established protocols used in the lab (ElGhazaly *et al.*, 2023). Briefly, cells were incubated with 20 ng/ml of toxin^{WT} or toxin^{HQ} for 2 hours, after which toxin$^{WT/HQ}$ was washed off and cells chased for an additional period of 48 or 96 hours before fixation (**Fig. 4.3 B**). Additionally, the DNA polymerase inhibitor Aphidicolin (APH) was used as a positive control for DDRs in Caco-2 cells.

Subsequent immunofluorescence staining revealed significant damage marked by γH2AX in toxin^{WT}-treated cells compared to untreated or toxin^{HQ}-treated cells at 48 hours, increasing further at 96 hours (**Fig. 4.3 C and D**). Relative to the untreated control, the positive control APH also induced significant γH2AX DDRs in 2D Caco-2 cells (**Fig. 4.3 C and D**).

As Caco-2 tubes gained barrier function by day 3 post cell-seeding but frequently lost it beyond day 5, tubes were intoxicated at day 3 using 20 ng/ml toxin$^{WT/HQ}$ and chased for 48 hours instead of 96 hours before fixing at day 5 (**Fig. 4.3 E**). Significant damage was observed in toxin^{WT}-treated tubes compared to untreated or toxin^{HQ} treated tubes, indicating that cells in 3D were also susceptible to the typhoid toxin at a concentration of 20 ng/ml (**Fig. 4.3 F and G**). Some damage was also observed in untreated tubes, which can be attributed to oncogene-induced DNA damage frequently observed in replicating cancer cells (Polo and Jackson, 2011).

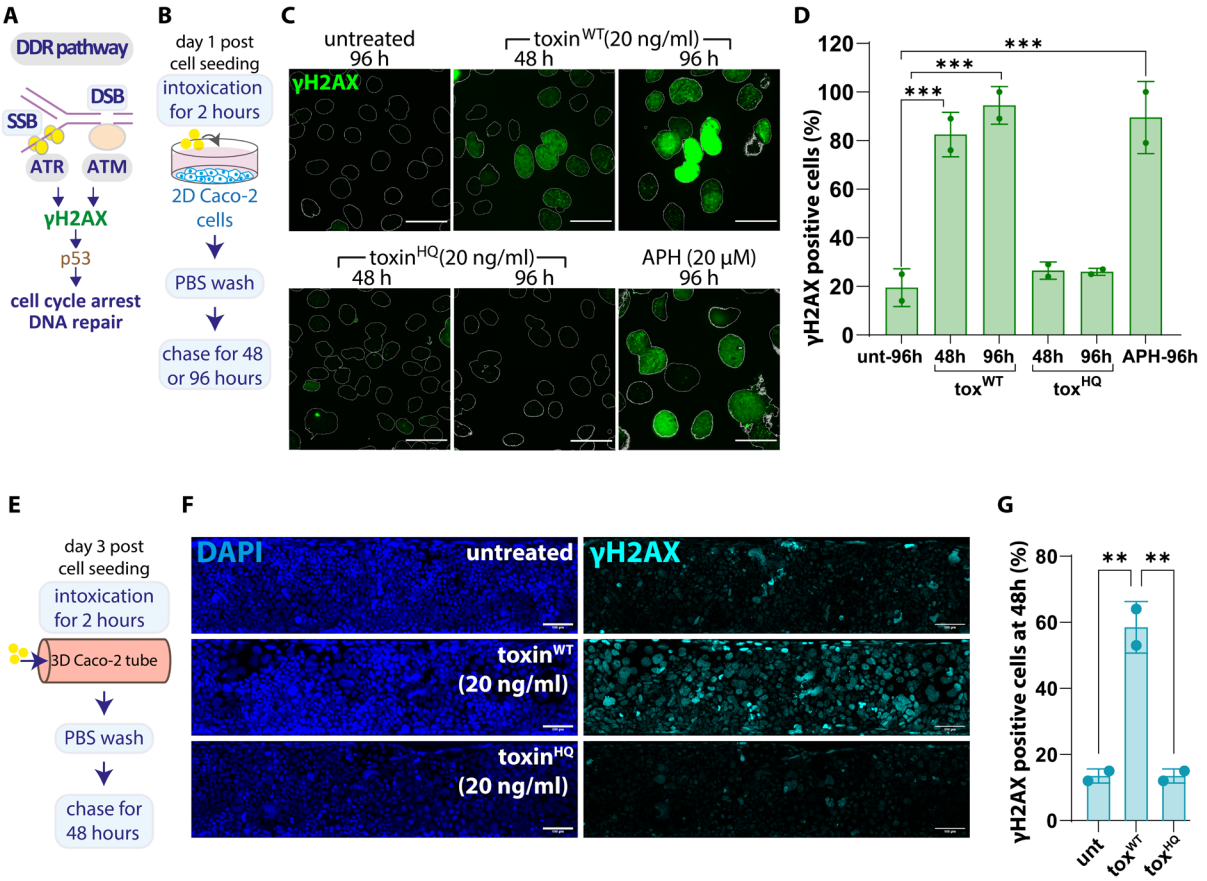

Figure 4.3 Damage induced by the typhoid toxin in 2D and 3D Caco-2 models. (**A**) Schematic summarising the DNA damage response (DDR). (**B**) Experimental plan for intoxicating 2D Caco-2 cells. (**C**) Fluorescence images showing γH2AX (green) in response to toxin^{WT} (20 ng/ml), toxin^{HQ} (20 ng/ml) and APH treatment in 2D Caco-2 cells at 48 hours or 96 hours post treatment. Nuclei depicted by DAPI outline (white). Scale bars are 50 μm. (**D**) Quantification of (C). Dots represent two biological replicates (n=2, ~188 nuclei per condition). (**E**) Experimental plan for intoxicating 3D Caco-2 tubes. (**F**) Fluorescence images showing DAPI stained nuclei (blue) and γH2AX (cyan) in untreated, toxin^{WT} (20 ng/ml) or toxin^{HQ}-treated (20 ng/ml) 3D Caco-2 tubes at 48 hours post-intoxication. Scale bars are 100 μm. (**G**) Quantification of (**F**). Dots represent two biological replicates (n=2, ~1416 nuclei per condition). One-way ANOVA with Tukey's multiple comparisons was used to test for significance. Error bars depict SD.

4.2.5. A gut-on-chip system using DLD-1 cells

DLD-1 cells are human adenocarcinoma cells that have been reported to express a mutant form of the p53 tumour suppressor protein (Lane *et al.*, 1990, Ookawa *et al.*, 2002) as opposed to Caco-2 cells which do not express the p53 protein (Thant *et al.*, 2008). Thus, a DLD-1 gut-on-chip system was an opportunity to study host responses

to typhoid toxin in cells that express p53 while maintaining characteristics of barrier function and polarization.

DLD-1 tubes were cultured the same way as the Caco-2 gut-on-chip on the OrganoPlate® (**Fig 4.0 A-E**). By day 3, tubes were observed to display barrier function and maintain barrier integrity until day 6 (**Fig 4.4**).

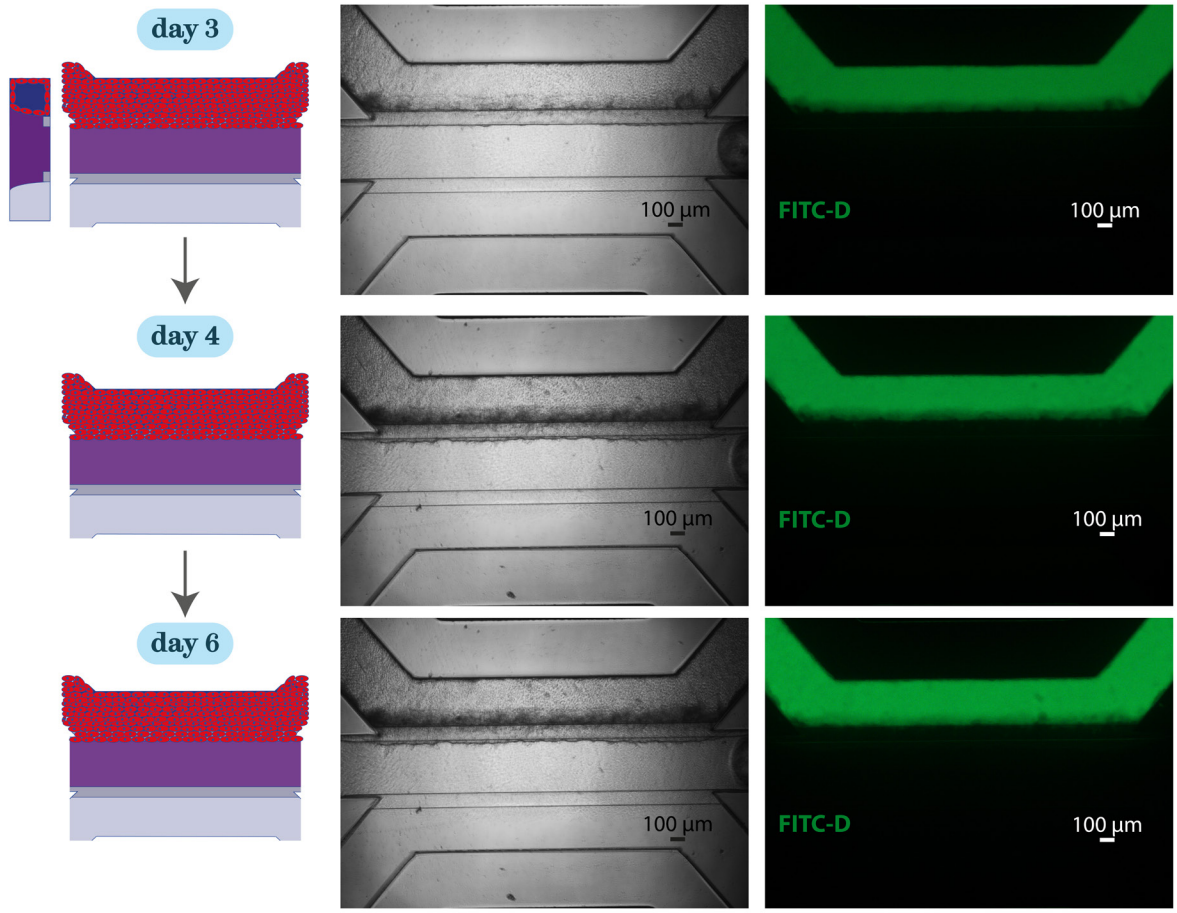

Figure 4.4 DLD-1 tubes develop barrier function by day 3. Phase contrast and fluorescence images of tubes perfused with 150 kDa FITC-dextran (green) at day 3, day 4 and day 6 post cell seeding.

4.2.6. Testing susceptibility of DLD-1 tubes to the typhoid toxin

To determine the concentration of recombinant typhoid toxin needed to activate a DDR response in DLD-1 tubes, toxin^{WT} activity was first tested in 2D DLD-1 cultures by incubating them with a range of toxin^{WT} concentrations. Since p21$^{Cip1/Waf1}$ expression is activated by p53 to promote cell-cycle arrest (Engeland, 2022) (**Fig. 4.5 A**), p21$^{Cip1/Waf1}$ expression was also examined as a proxy for p53 together with γH2AX

to determine the extent of DNA damage induced by the typhoid toxin in DLD-1 cells. To begin with, DLD-1 cells were seeded on 2D culture plates pre-coated with rat-tail Collagen I and incubated the next day (day 1) with 0.2, 2 and 20 ng/ml of $toxin^{WT}$ for two hours, followed by a 48-hour chase (**Fig. 4.5 B**). Additionally, the topoisomerase inhibitor Etoposide (ETP) was used as a positive control for DDRs in these cells. Subsequent immunofluorescence staining displayed a higher amount of cellular distension, γH2AX and $p21^{Cip1/Waf1}$ expression in DLD-1 cells treated with 20 ng/ml of $toxin^{WT}$ compared to cells treated with 0.2 or 2 ng/ml of $toxin^{WT}$ (**Fig. 4.5 C**).

As 20 ng/ml of $toxin^{WT}$ was observed to be more potent in triggering damage and distension in 2D DLD-1 cells (**Fig. 4.5 C**), DLD-1 tubes were also intoxicated with 20 ng/ml of $toxin^{WT}$ or $toxin^{HQ}$ for 2 hours and chased for 48 hours before fixation (**Fig. 4.5 D**). DDR activity was found to be heightened in tubes treated with the positive control APH, however, not much difference was observed between $toxin^{WT}$-treated tubes and negative controls (untreated and $toxin^{HQ}$-treated tubes) (**Fig. 4.5 E**).

As a result, the intoxication assay was modified and varying concentrations of $toxin^{WT}$ were left to incubate with the DLD-1 tubes for the entire 48-hour period, instead of a 2-hour pulse with a 48-hour chase (**Fig 4.6 A**). This time, tubes treated with 20 ng/ml $toxin^{WT}$ displayed a prominent increase in γH2AX phosphorylation in comparison to untreated tubes, which was similar to damage observed in tubes treated with 20 μM ETP (**Fig 4.6 B**). To assess whether the $toxin^{WT}$ was causing cell cycle arrest, tubes were incubated with the nucleotide analogue EdU for the final 24 hours before fixation. However, all DLD-1 tubes were found to be in a state of growth arrest in a damage-independent manner (**Fig 4.6 B**). While both $toxin^{WT}$ and ETP were observed to cause a subtle increase in p53 expression in comparison to untreated DLD-1 tubes, p53 activity remained the same in tubes treated with either 20 ng/ml or 100 ng/ml of $toxin^{WT}$.

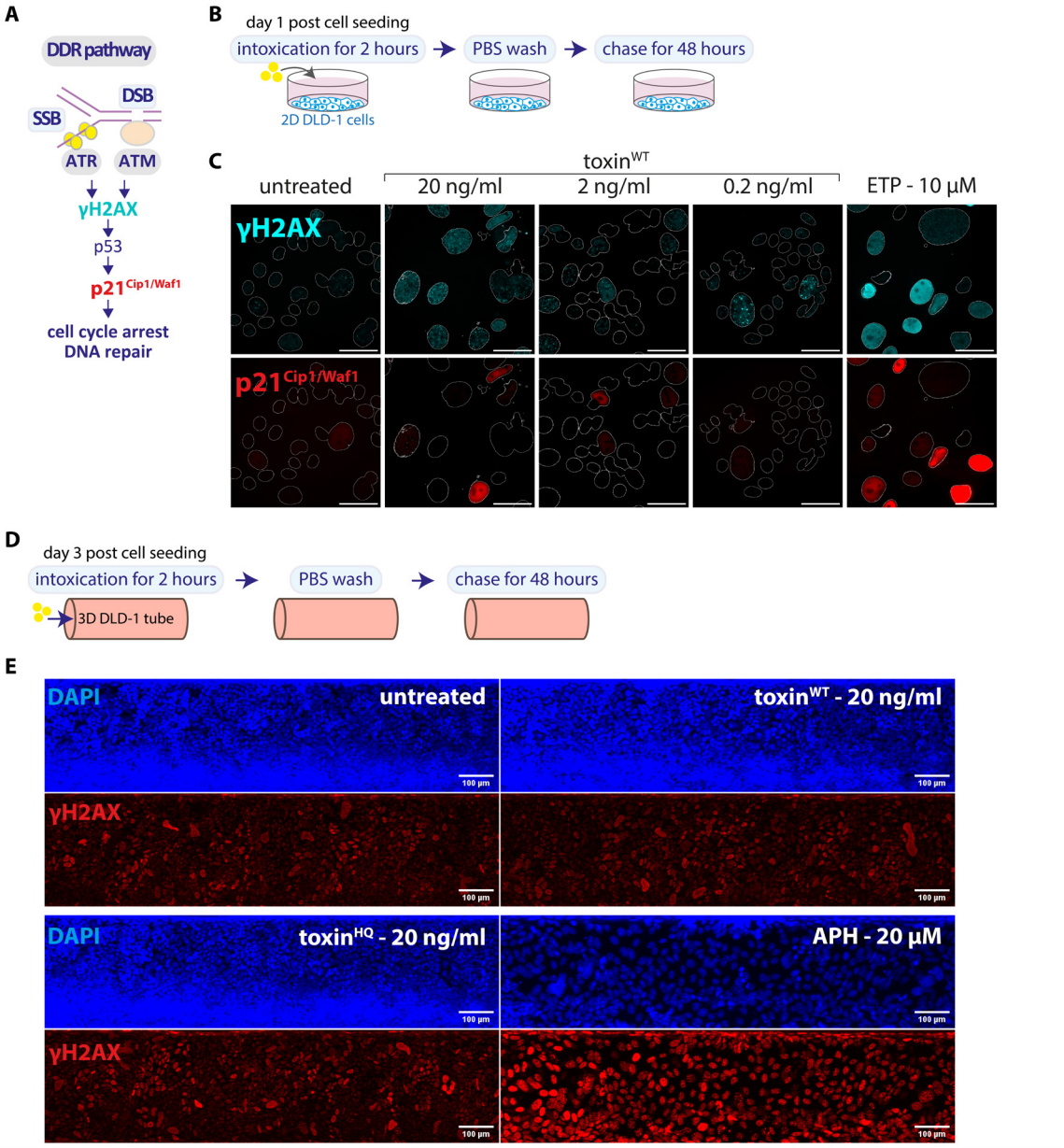

Figure 4.5 Toxigenic DDRs induced in 2D DLD-1 cells but not 3D DLD-1 tubes. (**A**) The cyclin dependent kinase inhibitor (CDI) p21$^{Cip1/Waf1}$ is activated by the transcription factor p53 during DDR. (**B**) Experimental plan for intoxicating 2D DLD-1 cells. (**C**) Fluorescence images showing γH2AX (cyan) and p21$^{Cip1/Waf1}$ (red) in untreated, toxin^{WT}-treated (20 ng/ml, 2ng/ml or 0.2 ng/ml) and ETP-treated (10 µM) DLD-1 cells. Scale bars are 50 µm. Nuclei depicted by DAPI outline (white). Images are representative of two technical replicates (n=1). (**D**) Experimental plan for intoxicating 3D DLD-1 tubes. (**E**) Fluorescence images showing DAPI stained nuclei (blue) and γH2AX (red) in control/untreated DLD-1 tubes and those treated with toxin^{WT} (20 ng/ml), toxin^{HQ} (20 ng/ml) and APH (20 µM). Scale bars are 100 µm. Images are representative of two technical replicates (n=1).

4.2.7. Testing toxin activity in human biopsy-derived intestinal organoids

While Caco-2 and DLD-1 cells are useful for developing gut-on-chip models in a short timeframe, they originate from adenocarcinomas and lack the variety of cell types or self-renewing capacity of the human intestinal epithelium. Organoids derived from intestinal biopsies, as well as gut-on-chip systems based on primary intestinal epithelial cells are promising alternatives in the arena of 3D culture. Thus, efforts were also made to establish intestinal organoids and primary gut-on-chips for studying DDRs by the typhoid toxin.

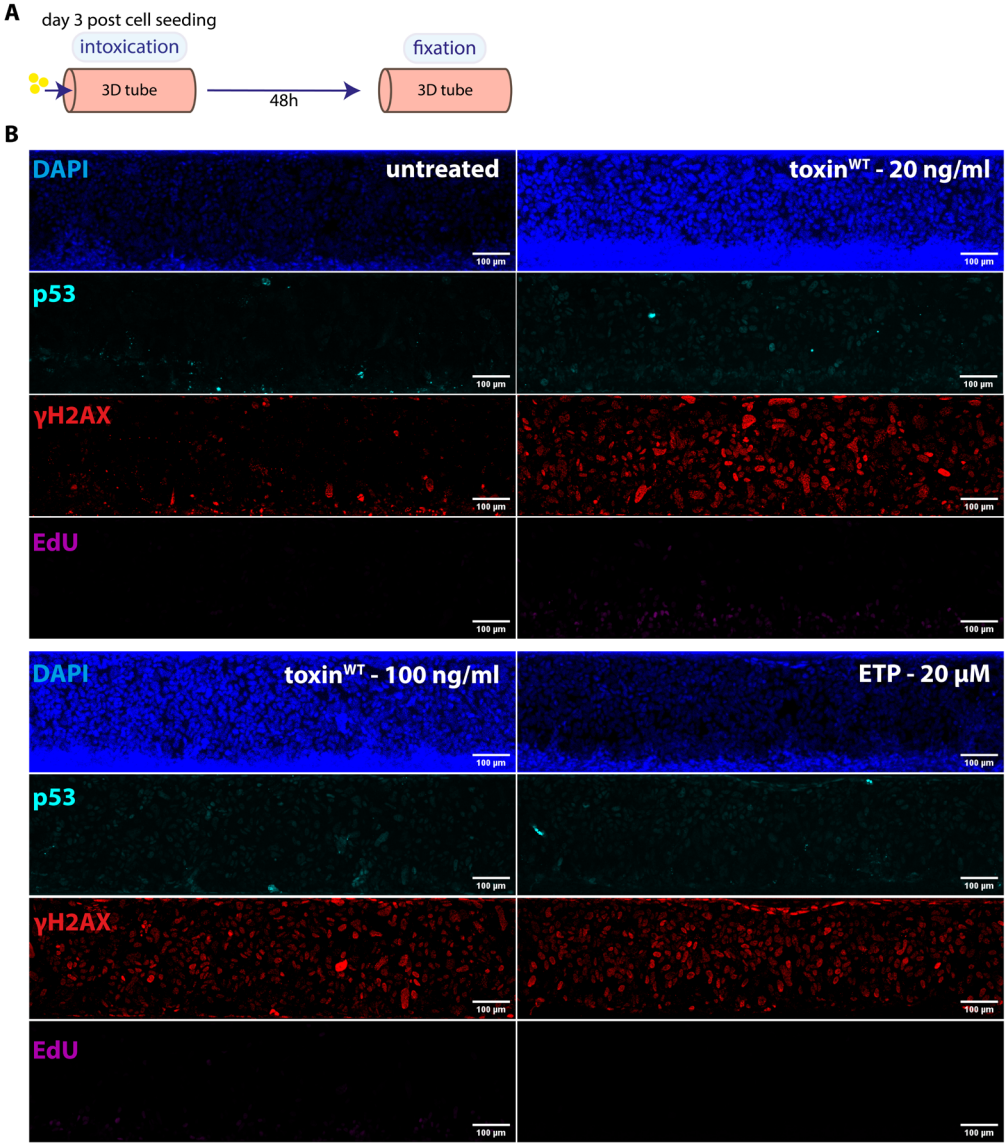

Figure 4.6 Continuous intoxication of DLD-1 tubes for 48 hours induces DNA damage. (**A**) Optimised experimental plan for intoxicating 3D DLD-1 tubes. (**B**) Fluorescence images showing

DAPI stained nuclei (blue), p53 (cyan), γH2AX (red) and EdU activity (magenta) in untreated, toxin^{WT}-treated (20 ng/ml or 100 ng/ml) and ETP-treated (20 μM) DLD-1 tubes. EdU was incubated for the final 24 hours before fixation. Scale bars are 100 μm. Images are representative of two technical replicates (n=1).

Colon organoids were generated in the Boccellato Lab from human tissue material obtained at the Translational Gastroenterology Unit at John Radcliffe Hospital, University of Oxford. Toxin^{WT} sensitivity was first tested in primary colon cells derived from the colon organoids. To do this, primary colon cells were seeded on 2D culture plates pre-coated with Collagen I and incubated the next day with 20 ng/ml of toxin^{WT} for 2 hours, followed by a 72-hour chase (**Fig 4.7 A**). Immunofluorescence images revealed minimal γH2AX activity in toxin^{WT}-treated cells similar to untreated cells, however, cells incubated for 72 hours with positive control ETP displayed more γH2AX activity (**Fig 4.7 B**). Despite a lot of background noise possibly due to interactions between the collagen layer and antibodies, γH2AX foci in ETP-treated cells were distinguishable (**Fig 4.7 B, white arrowheads**). p21$^{Cip1/Waf1}$ was highly expressed in all treatments including untreated cells, indicating potential growth arrest or quiescence (Hatzmann *et al*., 2021).

As a toxin^{WT} dose of 20 ng/ml did not elicit a DDR response, 2D primary colon cells were intoxicated a day after cell seeding (day 1) with a higher dose of 100 ng/ml for 2 hours and chased for 24, 48 or 72 hours before fixation. Additionally, the positive control ETP was incubated with the cells for 24, 48 or 72 hours before fixation. However, despite increasing the toxin^{WT} dose, cells were observed to display a high resilience towards toxin^{WT} with γH2AX levels similar to untreated cells and lower than ETP-treated cells at 24 hours (**Fig 4.7 C**). Despite high γH2AX activity in ETP-treated cells at 24 hours, this activity was reduced at 72 hours post ETP treatment (**Fig 4.7 C**). While p21$^{Cip1/Waf1}$ expression was similar in all treatments, EdU incorporation was reduced in ETP-treated cells at 24 hours in comparison to untreated cells at 24 hours (**Fig 4.7 C**). However, EdU incorporation also declined in untreated cells from 24 to 72 hours. In summary, while untreated cells were observed to undergo growth arrest over time in a damage-independent manner, this arrest seemed to be exacerbated in the presence of ETP. Importantly, the primary cells were insensitive to toxin^{WT} as EdU was

still incorporated in toxin^{WT}-treated cells, which was consistent with γH2AX and p21$^{Cip1/Waf1}$ levels that were indistinguishable from untreated cells (**Fig 4.7 C**).

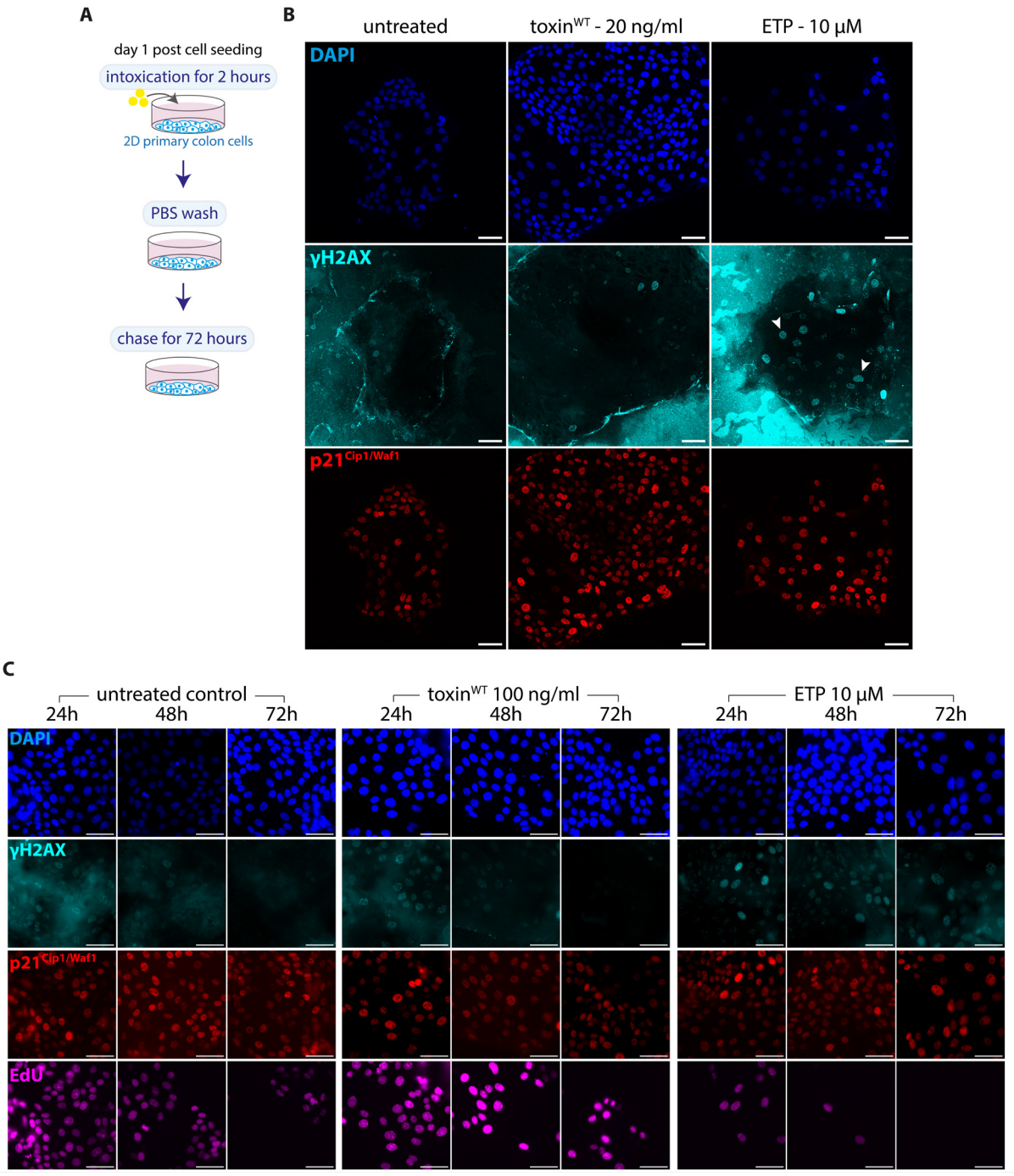

Figure 4.7 Toxin does not elicit DDRs in primary colon cells. (**A**) Experimental plan for intoxicating 2D primary colon cells. (**B**) Fluorescence images showing DAPI stained nuclei (blue), γH2AX (cyan) and p21$^{Cip1/Waf1}$ (red) in untreated, toxin^{WT}-treated (20 ng/ml) and ETP-treated (10 µM) 2D primary colon cells. Scale bars are 50 µm. (**C**) Fluorescence images showing DAPI stained

nuclei (blue), γH2AX (cyan), $p21^{Cip1/Waf1}$ (red) and EdU (magenta) in untreated 2D primary colon cells, 2D primary colon cells treated for 2 hours with 100 ng/ml $toxin^{WT}$ and chased for 24, 48 and 72 hours, and 2D primary colon cells treated with 10 μM ETP for 24, 48 and 72 hours. EdU was incubated for the final 24 hours before fixation. Scale bars are 50 μm. Images are representative of three technical replicates (n=1).

To test $toxin^{WT}$ activity in colon organoids, primary colon cells were sheared from organoids and freshly seeded in Cultrex's reduced growth factor basement membrane extract (RGF BME) type 2 select gel for 3D culture. The same day (day 0), cells were intoxicated for a period of 72 hours with 20 ng/ml of $toxin^{WT}$ (**Fig 4.8 A**). It was hypothesized that if the toxin was able to cause DDR and permanent cell cycle arrest in cells, this would hinder their development into the spherical 3D structure of colon organoids. Moreover, the change in intoxication period from 2 hours to 72 hours was to ensure toxin access to cells in the 3D gel for a longer time.

However, $toxin^{WT}$-mediated DNA damage in terms of γH2AX was minimal despite modifying the duration of intoxication (**Fig 4.8 B**). An increase in DNA damage was observed in cells within the ETP-treated organoid compared to the untreated organoid (**Fig 4.8 B**). Nevertheless, the organoid itself was found to be intact and spherical. The expression pattern of $p21^{Cip1/Waf1}$, on the other hand, was heterogenous from organoid to organoid within each treatment (**Fig 4.8 B, white arrows**), making it difficult to assess if ETP-treated organoids were undergoing arrest in a DDR-dependent manner.

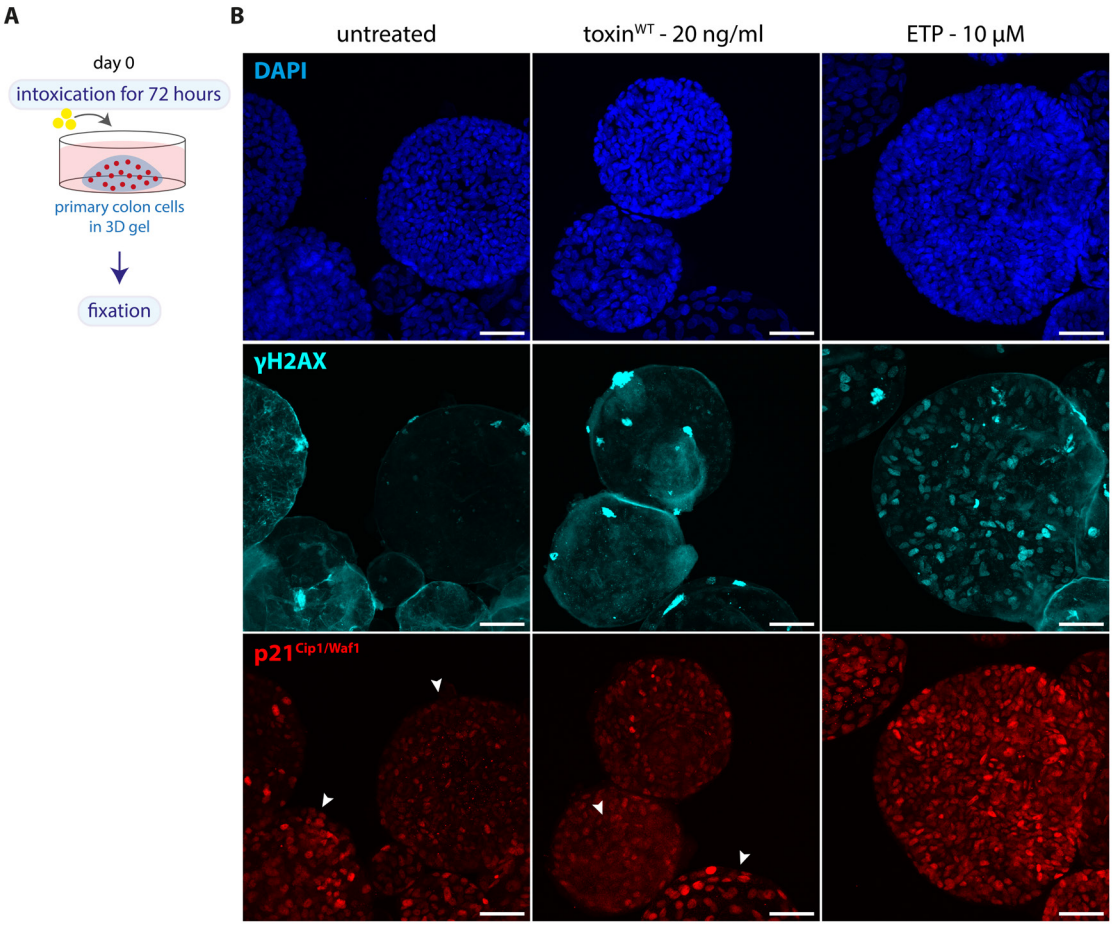

Figure 4.8 No toxigenic DDRs in colon organoids. (**A**) Experimental plan for intoxicating colon organoids. (**B**) Fluorescence images showing DAPI stained nuclei (blue), γH2AX (cyan) and $p21^{Cip1/Waf1}$ (red) in organoids under different conditions. White arrows show variance in $p21^{Cip1/Waf1}$ expression between organoids. Scale bars are 50 µm. Images are representative of three technical replicates (n=1).

4.2.8. A gut-on-chip system using human biopsy-derived intestinal organoids

Intestinal organoids contain diverse epithelial cell types and have the capacity to self-renew (Sato *et al.*, 2009, Drost *et al.*, 2015), making them more physiologically relevant than adenocarcinoma-derived 3D models. However, the spherical architecture of the lumen embedded within an intestinal organoid greatly limits access by invading pathogens or toxins into the lumen, as opposed to a tubular intestine with an accessible lumen found *in vivo*.

Given the difficulties in initiating a response to the typhoid toxin in colon organoids or primary colon cells, efforts were made to develop a gut-on-chip system using

primary colon cells to test potential susceptibility to the toxin. Initially, cells failed to form 3D tubes after seeding in the OrganoPlate® (**Fig 4.9 A**). In order to provide a friendlier environment for primary cells to grow three-dimensionally as a monolayer rather than organoids in the top cell seeding channel (**Fig 4.9 A, black arrowheads**), a second attempt was made where the top channel was pre-coated with Cultrex gel before seeding a higher cell suspension of 50,000 primary colon cells instead of 20,000 cells. The quality of the single cell suspension was also optimised by replacing flamed glass-pipettes with plastic pipette tips for shearing organoids, pre-coating plastic pipette tips with PBS + 1% BSA solution and using DNase 1 and Rho kinase inhibitor (ROCKi) during dissociation with TrypLE to prevent cell clumping and cell death. Moreover, for the first 48 hours post cell seeding, SB431542, a transforming growth factor-β (TGF-β) signalling inhibitor was removed from the culture medium to promote cell attachment as performed previously by Beaurivage *et al.* in 2020 using the TGF-β inhibitor A83-01.

Indeed, upon a second attempt, cells seeded in the top channel were observed to retain the FITC dye within the channel at day 8 post seeding, with unequal distribution of the dye across the channel (**Fig 4.9 B**). Additionally, the dye was observed to leak across channels at day 12 after delays in medium refreshment, with cells clustering into islands instead of a tube (**Fig 4.9 C**). Nonetheless, given that the 3D primary intestinal tubes were grown in medium supplemented with growth factors such as Wnt and Rspo1 that promote self-renewal of intestinal stem cells (Sato *et al*., 2009, Drost *et al*., 2015), it could be possible that they re-develop leak-proof barriers upon continued culture and medium refreshment in the OrganoPlate®. However, due to limited time, this model could not be optimised further or tested for its susceptibility to the toxin^{WT}.

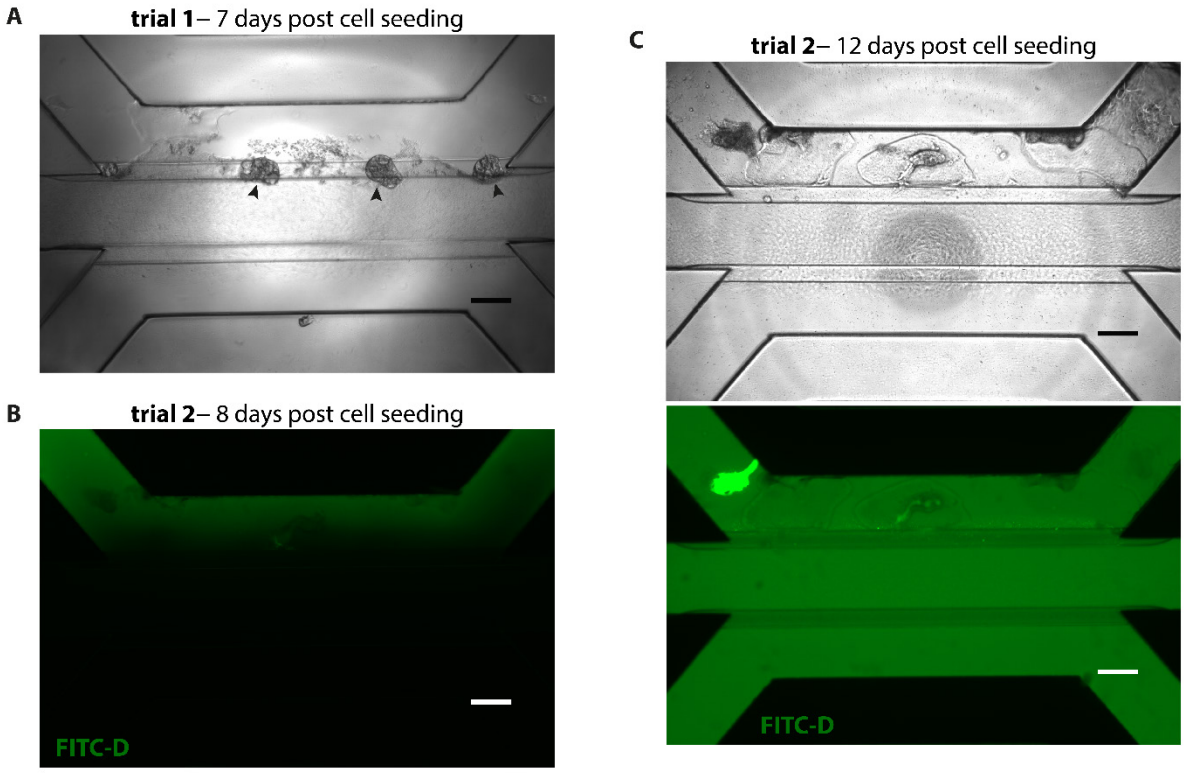

Figure 4.9 Human biopsy-derived primary gut-on-chip model. (**A**) Phase contrast image of first trial showing primary colon cells forming organoids (black arrows) instead of a tube at day 7 post cell seeding. Scale bars are 100 µm. (**B**) Fluorescence image of second trial showing a primary colon tube displaying barrier function upon perfusion with 150 kDa FITC-Dextran at day 8 post cell seeding. Scale bars are 100 µm. (**C**) Phase contrast and fluorescence images of second trial showing loss of barrier function in the primary colon tube at day 12 post cell seeding. Scale bars are 100 µm. All images are representative of three technical replicates (n=1).

4.3. Discussion

This chapter summarizes an exploration of several 3D models using different cellular raw materials. The Caco-2 gut model, due to its ease of culture and accessibility in the lab, was explored the most in terms of epithelial polarization and sensitivity to the typhoid toxin. 3D Caco-2 tubes were observed to express acetylated α-tubulin and ZO-1 (**Fig 4.2**), proteins that are associated with microtubules and tight junctions in polarized epithelial cells (Bellett *et al.,* 2009, Dogterom and Koenderink, 2019, Trietsch *et al.,* 2017). However, unlike previous reports in the literature, the presence of apical-basal polarity, microvilli or cilia were not clear with α-tubulin staining (**Fig 4.2**). Determining the presence of such cellular structures would be more

insightful using antibodies for actin and the cytovillin protein ezrin instead, as they stain these cytoskeletal structures more clearly (Trietsch *et al.,* 2017). Furthermore, the use of Transepithelial Transendothelial Electrical Resistance (TEER) assay to determine the resistance of tissue barriers (Nicolas *et al*., 2020) would strengthen findings regarding barrier function in 3D organ-on-chip models using Caco-2, DLD-1 or primary colon cells, as large molecular sizes of FITC-dextran dye can influence the barriers to appear more leakproof than they may be.

Current literature on the typhoid toxin shows concentrations between 5 and 20 ng/ml as sufficient for inducing DDR responses in human cell cultures (Ibler *et al*., 2019, ElGhazaly *et al*., 2023, Deng *et al*., 2014, Song *et al.,* 2013). Indeed, Caco-2 tubes displayed DDRs when intoxicated with 20 ng/ml of toxin^{WT} for a 2-hour pulse before chasing for 48 hours (**Fig 4.3**). On the other hand, 3D DLD-1 tubes displayed tolerance to DDRs at the same dose of toxin^{WT} for the same pulse and chase period (**Fig 4.5**) but were susceptible to 20 ng/ml toxin^{WT} when incubated continuously for 48 hours instead of a 2-hour pulse (**Fig 4.6**). Furthermore, human colon organoids were resistant to toxin-induced DDRs when incubated with 20 ng/ml of toxin^{WT} for 72 hours (**Fig 4.8**), while 2D primary colon cells were resistant to DDRs at both 20 ng/ml and 100 ng/ml of toxin^{WT} when pulsed for 2 hours with a 72-hour chase (**Fig 4.7**).

The sensitivity of 2D primary colon cells and colon organoids to toxin^{WT} doses greater than 20 ng/ml, with an incubation time of more than 2 hours remains to be investigated. As toxin binding and uptake is largely dependent on the N-Acetylneuraminic acid (Neu5Ac) glycosylation motif at the end of the toxin receptor (Varki *et al.,* 2014, Deng *et al*., 2014), it is possible that a lack of these motifs on surface receptors, lack of receptors themselves or limited access to them could impact toxin uptake and DDRs in these models. Interestingly, the presence of Neu5Gc in bovine serum is known to increase its uptake and incorporation into mesenchymal stromal cells (Pilgrim *et al.,* 2022). Both Caco-2 and DLD-1 cells were cultured in 2D and 3D using medium supplemented with FBS, while 2D primary colon cells and 3D primary colon organoids were cultured in medium supplemented with BSA. Although there is not much literature available regarding the concentration of Neu5Gc in FBS and BSA, the use of bovine serum in primary colon culture could be affecting Neu5Ac receptor distribution on the cell surface and their interactions with the toxin.

Investigating the presence of Neu5Ac receptors via immunostaining or ELISA could reveal more information about their distribution in primary colon cells and organoids. Additionally, toxin interactions with these receptors via flow cytometry or immunostaining will be helpful in determining the extent of toxin uptake in 2D and 3D primary colon cultures.

The CDK inhibitor $p21^{Cip1/Waf1}$ is known to play a prominent role in cell fate decisions such as quiescence to maintain the homeostasis and regenerative capacity of adult stem cells (Urbán and Cheung, 2021), which could explain the activation of $p21^{Cip1/Waf1}$ in untreated cells in both 2D primary colon cells and 3D primary colon organoids despite a lack of DNA damage marked by γH2AX (**Fig 4.7 and 4.8**). Future work could include the use of markers such as RPA and 53BP1 to determine DDRs (Polo and Jackson, 2011, Cimprich and Cortez, 2008) activated by the toxin in primary cell culture models in order to distinguish them from cellular events occurring in parallel in untreated cells such as quiescence.

Given the lack of time in consolidating intoxication data for 3D DLD-1 tubes, primary colon organoids and 3D primary colon tubes, the focus of the project was steered towards diving deeper into DDR responses activated in Caco-2 tubes in response to the typhoid toxin.

5. Toxin-mediated damage in 2D versus 3D Caco-2 models

5.1. Introduction

In the previous chapter, despite differences in culture formats between 2D Caco-2 cells and the Caco-2 gut-on-chip, the typhoid toxin was observed to cause significant γH2AX phosphorylation in both models. As a result, it was hypothesised that toxigenic DDR responses may be similar in the two models regardless of the culture method. To investigate this possibility, an RNA sequencing (RNAseq) experiment was designed to determine transcriptional changes in 2D Caco-2 cells and the Caco-2 gut-on-chip models due to toxin triggered DDR responses. RNAseq is a widely used technique for determining the sequence and abundance of mRNA transcripts expressed in a model of interest, as well as the genes they were transcribed from. Additionally, this technique can be employed to quantify relative abundance of transcripts between two different samples.

5.2. Results

5.2.1. Preparation of samples for RNAseq

Caco-2 gut-on-chips were cultured for 3 days for barrier development, while Caco-2 cells were seeded in tissue culture plates and allowed to attach overnight. Once Caco-2 gut-on-chips displayed barrier function at day 3 and the 2D Caco-2 cells had attached to the plate surface, each model was intoxicated for 2 hours with toxin^{WT} or

toxin^{HQ}, then incubated for a further 48 hours (**Fig 5.0 A**). As additional controls, Caco-2 gut-on-chips were either left untreated or treated with ETP at day 3 for 48 hours. Subsequently, cellular material from all samples was harvested for RNA extraction.

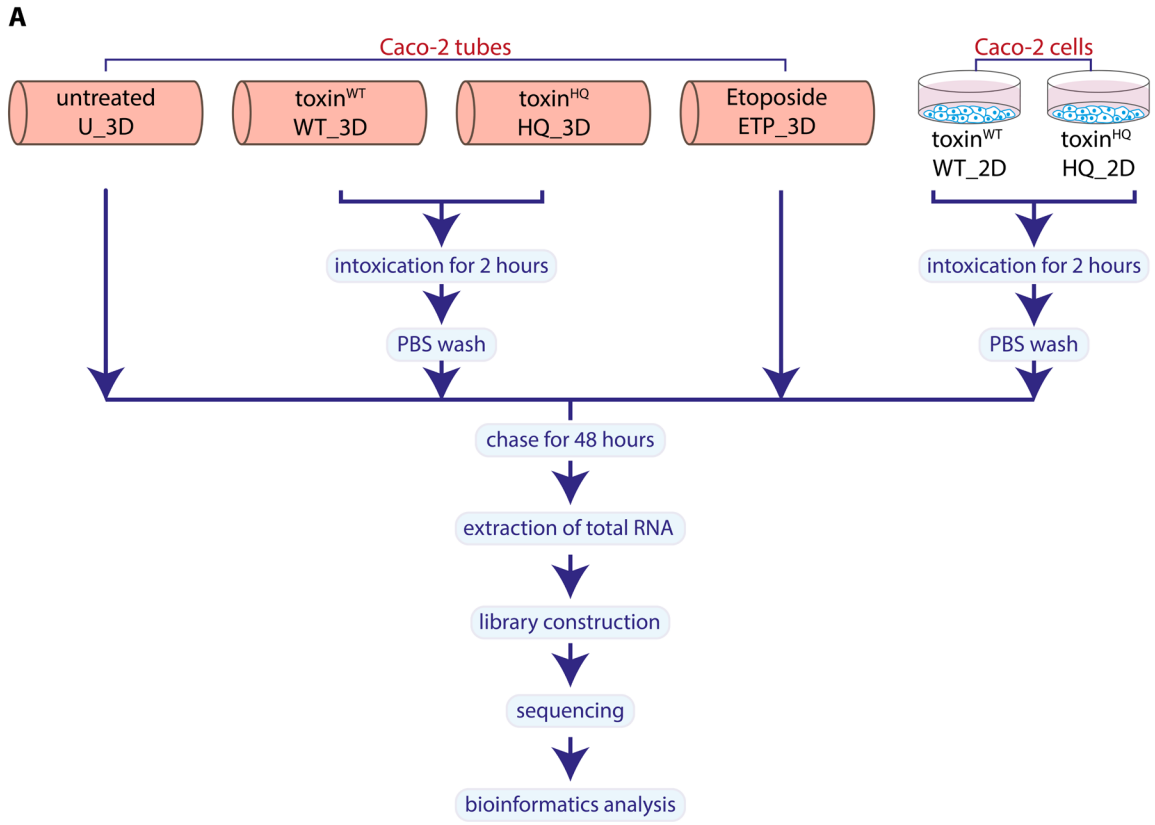

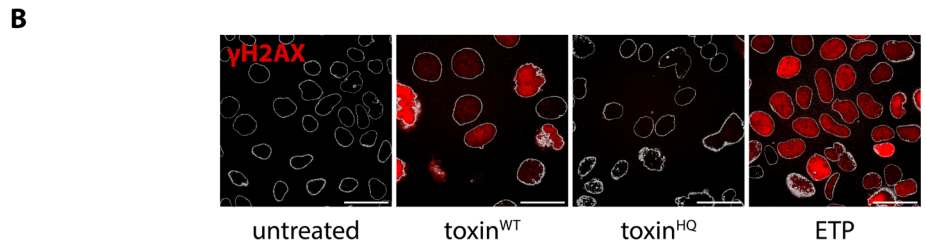

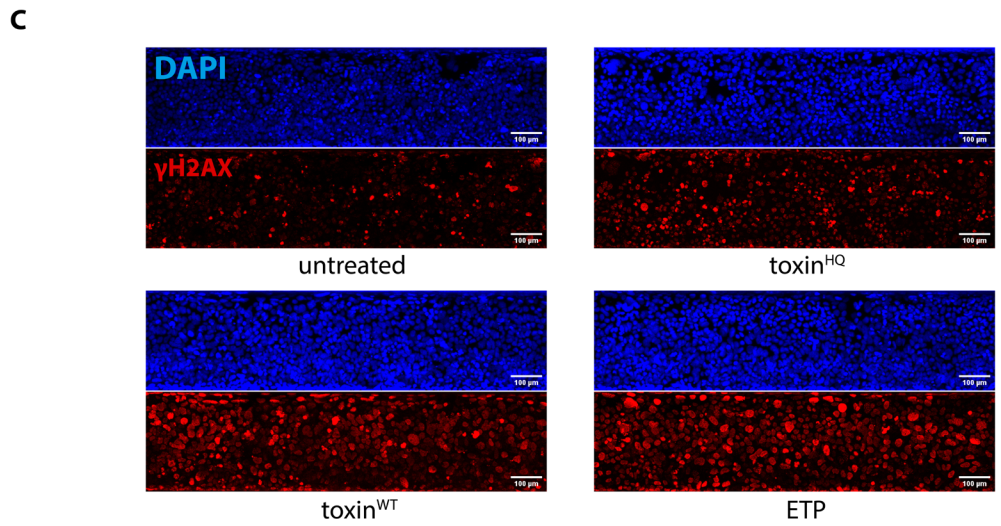

Figure 5.0 Validating toxin activity in RNAseq samples. (**A**) Schematic of the RNAseq experiment. Samples were run in triplicates. (**B**) Representative immunofluorescence images from the RNAseq experiment showing DAPI (blue) and γH2AX (red) stained nuclei in untreated, $toxin^{WT}$ (20 ng/ml), $toxin^{HQ}$ (20 ng/ml) and ETP (10 μM) treated 2D Caco-2 cells at 48 hours post treatment. Scale bars 50 μm. (**C**) Representative images from the RNAseq experiment showing DAPI (blue) and γH2AX (red) stained nuclei in untreated, $toxin^{WT}$ (20 ng/ml), $toxin^{HQ}$ (20 ng/ml) and ETP (10 μM) treated 3D Caco-2 tubes at 48 hours post treatment. Scale bars 100 μm.

The isolated RNA was then fragmented to a 150 basepair (bp) length, converted to cDNA strands for stability and prepared for multiplexing by Novogene. To ensure the samples collected for RNAseq had truly undergone DNA damage, replicates of each sample were analysed in parallel by immunofluorescence of γH2AX and fluorescence microscopy (**Fig 5.0 B and C**). Both 2D and 3D samples treated with the wild-type toxin or ETP displayed characteristics of DNA damage such as increased γH2AX phosphorylation and cellular distension, as opposed to untreated or $toxin^{HQ}$ controls (**Fig 5.0 B and C**), which was in line with DNA damage data in chapter 4 (**Fig 4.3**). Thus, it was clear that Caco-2 cells in both 2D and 3D culture formats were responsive to the typhoid toxin when exposed to the same concentration for the same time period, which provided confidence in utilising these samples for subsequent RNA sequencing.

5.2.2. Sequenced fragments display high quality scores

For sequencing single-stranded cDNA fragments (or sequences or reads) on the Illumina sequencing platform (or flow cell), nucleotide probes are introduced by the sequencer along with a DNA polymerase into this flow cell, where each probe fluoresces to a unique wavelength based on the nucleotide base that they bind with (Illumina, 2023, Bentley *et al.,* 2008). These probes bind with the unknown bases on the cDNA fragment sequentially, and at each binding step, the fluorescence emitted by the probe is used to identify the complementary nucleotide that it bound with, a technique also known as Base calling (Illumina, 2023).

For the sequenced reads to be reliable and usable for mapping to a reference genome, the quality of base detection needs to be high. This quality is logarithmically linked to the probability of the base call being wrong by the following equation –

$$Q = -10\log_{10}(e)$$

where *Q* is the quality score assigned by the sequencer to a detected base, and *e* is the probability of the base call being incorrect (or error rate) (Illumina, 2023).

Lower error rates indicate higher quality scores and higher base call accuracy, as indicated below (**Table 5.1**).

Base call error rate	Quality Score	Base call success rate
1 in 10 bases or 0.1	10 (Q10)	90%
1 in 100 bases or 0.01	20 (Q20)	99%
1 in 1000 bases or 0.001	30 (Q30)	99.9%
1 in 10000 bases or 0.0001	40 (Q40)	99.99%

Table 5.1 Error rates and their relationship with Quality scores.

The distribution of error rate for each base along all reads was less than 0.05% in every 3D and 2D Caco-2 sample (**Fig 5.1, 5.2**) indicating towards a base call accuracy of at least 90% for all raw reads in all samples. While the error rate was observed to increase slightly with the increase in read length, this has been reported to be common occurrence in the Illumina sequencing platform (Erlich Y *et al.,* 2008, Jiang L *et al.,* 2011).

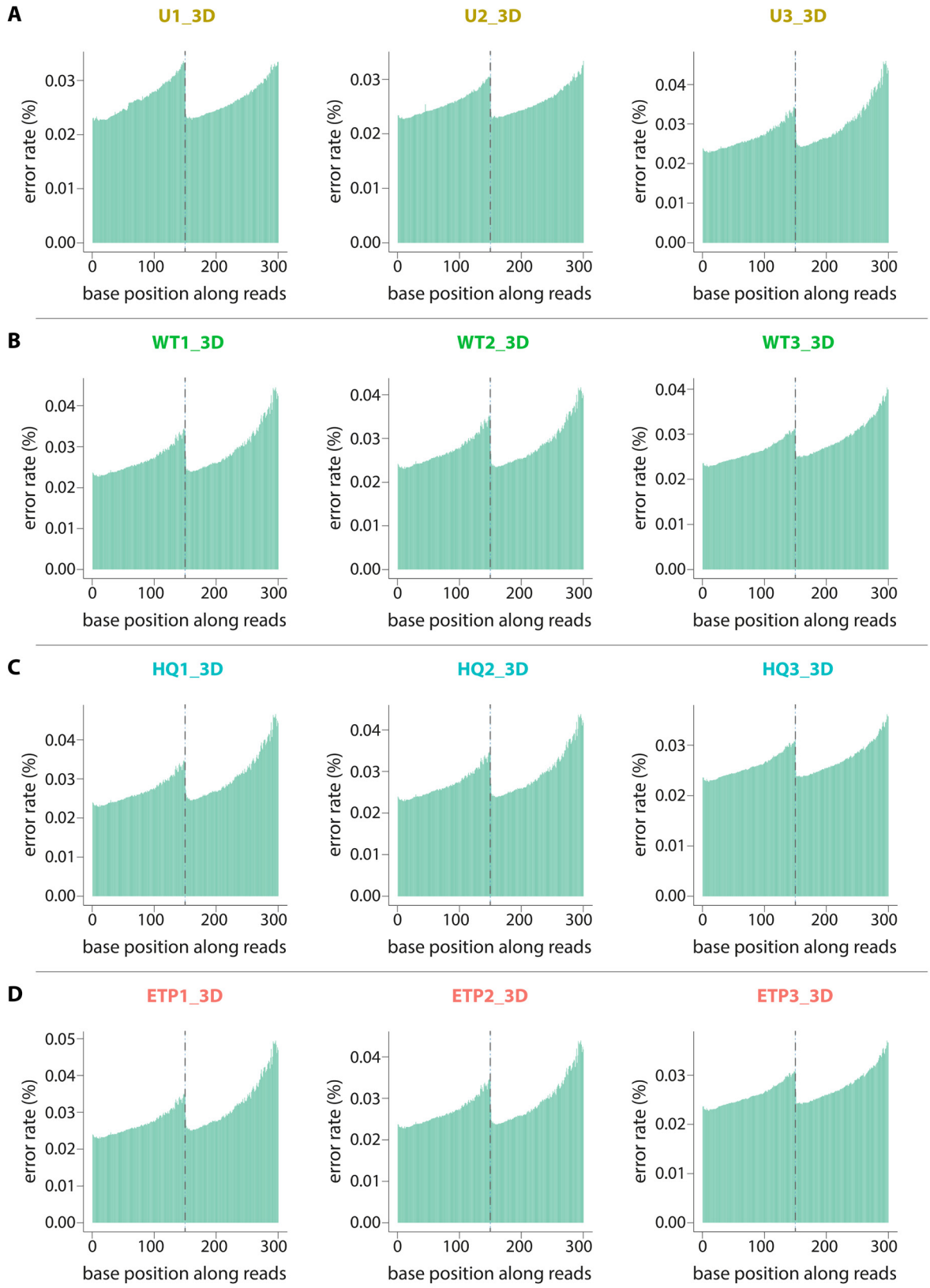

Figure 5.1 Error rates of 3D Caco-2 samples by Novogene. Graphs depict the error rate of each nucleotide base in each read in (**A**) untreated (**B**) toxin^{WT} treated (**C**) toxin^{HQ} treated and (**D**)

Etoposide treated tubes. Numbers 1, 2 and 3 after sample name, e.g., U1, U2 and U3 indicate individual replicates.

Additionally, raw reads were filtered by Novogene for reads with adapter contaminants or uncertain/low quality nucleotides, resulting in clean reads with more than 90% of bases having a *Q* score of 30 (**Table 5.2**). The standard for acceptable reads is a quality score of Q30 for at least 85% of bases for paired end 150 bp sequencing on the Illumina Novaseq 6000 System. Thus, reads post filtering were deemed reliable for use in genome mapping and subsequent analyses.

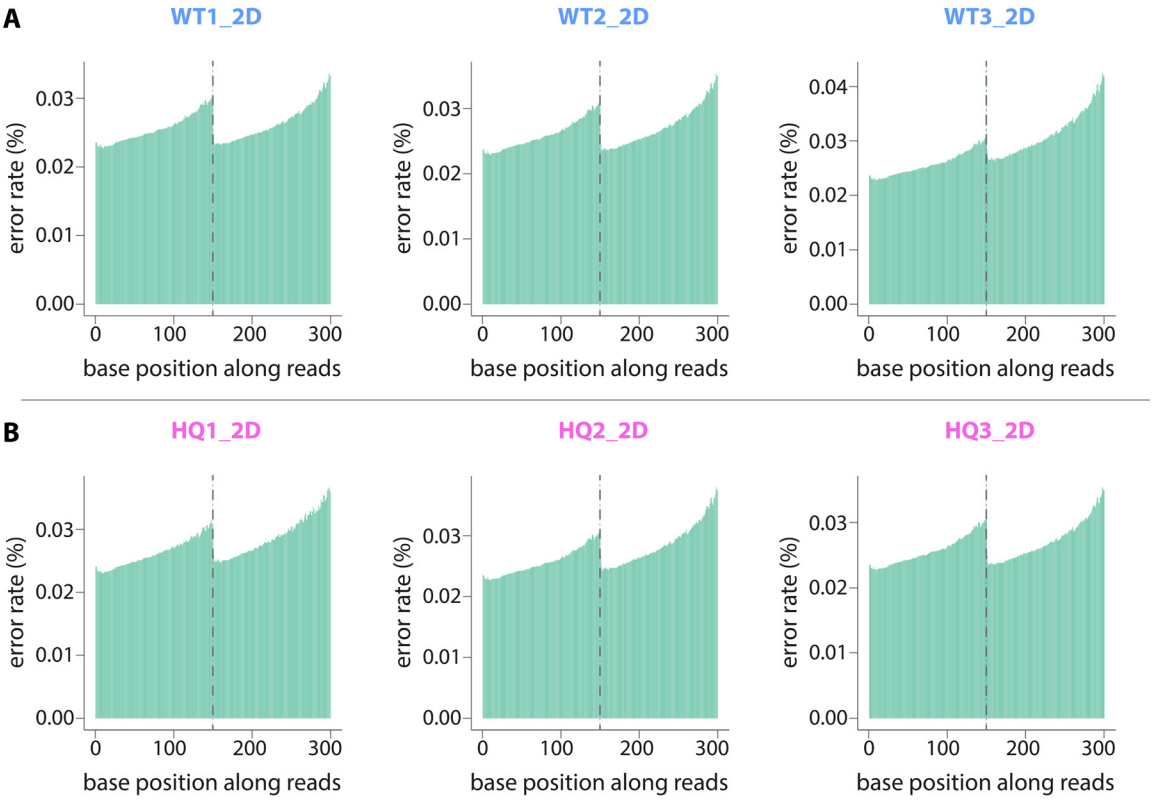

Figure 5.2 Error rates of 2D Caco-2 samples by Novogene. Graphs depict the error rate of each nucleotide base in each read in (**A**) toxin^{WT} treated (**B**) toxin^{HQ} treated cells. Numbers 1, 2 and 3 after sample name, e.g., WT1, WT2 and WT3 indicate individual replicates.

Reference mapping was performed using HISAT2 software by Novogene. The depth and alignment of clean reads was observed to vary between replicates of each treatment and across treatments as well (**Table 5.2**, **Fig 5.3**). Within each sample,

about ~90% of the reads mapped to unique positions on the reference genome, while about 3% mapped to multiple locations on the reference genome (**Fig 5.3**).

Sample	Raw reads	Clean reads	Total number of bases in clean reads	Percentage of bases with Quality score of Q30
ETP1_3D	53740426	53267272	7.99G	90.47
ETP2_3D	62141568	61590028	9.24G	91.51
ETP3_3D	53257118	52081318	7.81G	92.53
U1_3D	63713338	62287712	9.34G	92.83
U2_3D	46293548	45940100	6.89G	93.45
U3_3D	57381710	56864280	8.53G	91.14
WT1_3D	74435464	73760386	11.06G	91.45
WT2_3D	54878422	54334238	8.15G	91.64
WT3_3D	79436004	77881018	11.68G	91.87
HQ1_3D	52780882	52343274	7.85G	90.91
HQ2_3D	55284574	54839084	8.23G	91.39
HQ3_3D	62569176	61199370	9.18G	92.75
WT1_2D	51339850	50284482	7.54G	93.32
WT2_2D	72928966	71446038	10.72G	92.85
WT3_2D	67432300	66100136	9.92G	91.3
HQ1_2D	54202628	53601526	8.04G	91.96
HQ2_2D	58579910	57367668	8.61G	92.4
HQ3_2D	67420938	65996410	9.9G	92.98

Table 5.2 Summary of filtered reads and their quality scores in all samples.

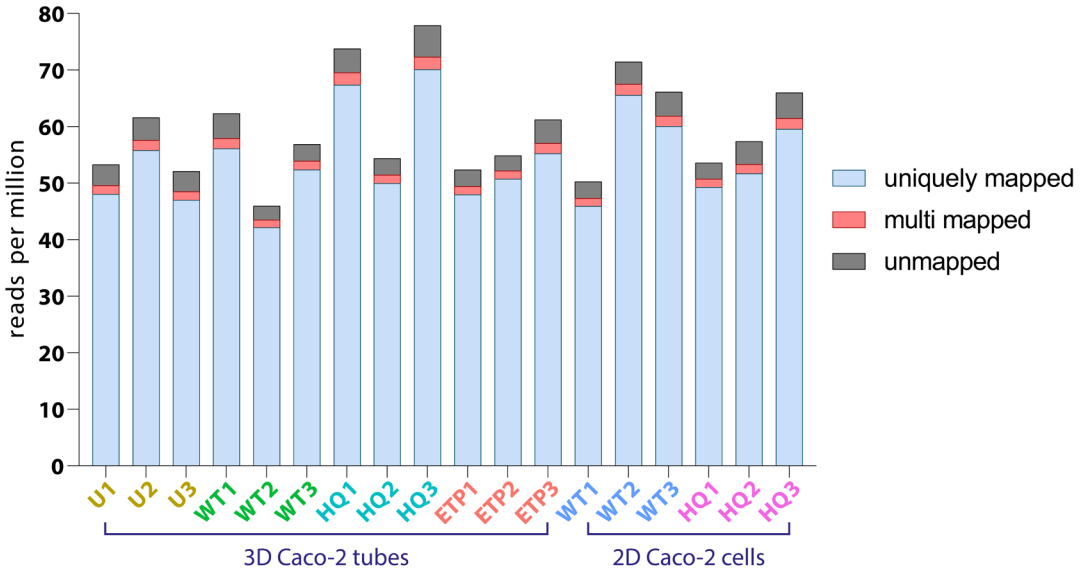

Figure 5.3 Read alignment across various samples. The graph depicts the number of clean reads that mapped to unique or multiple positions on the reference genome in 2D and 3D Caco-2 samples under different conditions. Y axis depicts the read number in millions, while X axis shows sample replicates, where individual colours represent individual sample conditions.

5.2.3. Correlation analysis of transcriptomes

As highly expressed genes have multiple reads that map to a single gene, the abundance of transcripts expressed by each gene was determined by quantifying the number of reads mapped per gene, also called the read count. In this instance, reads that mapped to several locations on the reference genome were filtered, and only uniquely mapped reads were used for quantification.

Samples with a higher number of clean reads (or sequencing depth) may have a high read count for a gene, while samples with a lower number of good quality reads may have a low read count for that gene. Similarly, longer genes may have more reads that map to them, giving the illusion that they have been transcribed much more than shorter genes. Thus, normalising read counts to the length of the gene and the sequencing depth of a sample becomes necessary to prevent biases during correlation and co-expression analyses. This normalised count is calculated in terms of RPKM (reads per kilobase of gene per million of mapped reads). For paired end RNAseq where two reads (forward and reverse) are generated from the same cDNA fragment, the read count is also normalised for the number of reads per fragment. This

normalised count is called FPKM (fragments per kilobase of gene per million of mapped fragments).

FPKM counts for all genes were calculated and used by Novogene to determine intergroup and intragroup correlations between samples before proceeding with differential expression analysis. To reduce multi-dimensionality from thousands of gene variables and plot them two-dimensionally for correlation analysis, best fit lines were created by Novogene using the linear algebra calculation method to summarize transcriptomic data in all samples simultaneously. The first line created was termed Principal Component 1 and was projected using a linear combination of gene values in FPKM, where projected values display the highest variance. The next best fit line termed Principal Component 2 was created the same way, but orthogonally to PC1.

The graph generated using PC1 and PC2 showed sample triplicates clustered in the same quadrant for each condition (e.g., U1_3D, U2_3D, U3_3D), highlighting minimal differences between their transcriptomes (**Fig 5.4**). Along PC1, 2D Caco-2 samples (toxin^{WT}-treated and toxin^{HQ}-treated) were clustered separately from 3D Caco-2 samples. On the other hand, all DNA damaged samples (ETP and toxin^{WT}-treated) were clustered separately from untreated and toxin^{HQ}-treated controls along the PC2 axis. As PC1 and PC2 account for the largest and second largest variance of projection respectively, the largest variation in gene expression was due to differences in the culture format of the samples, while the second largest variation was due to differences in DDR responses between the samples (**Fig 5.4**). Additionally, 2D and 3D Caco-2 samples treated with toxin^{WT} (WT_3D and WT_2D) overlapped minimally along PC2, indicating that divergent responses were elicited by the toxin^{WT} in the two models due to Caco-2 polarisation in the 3D gut-on-a-chip.

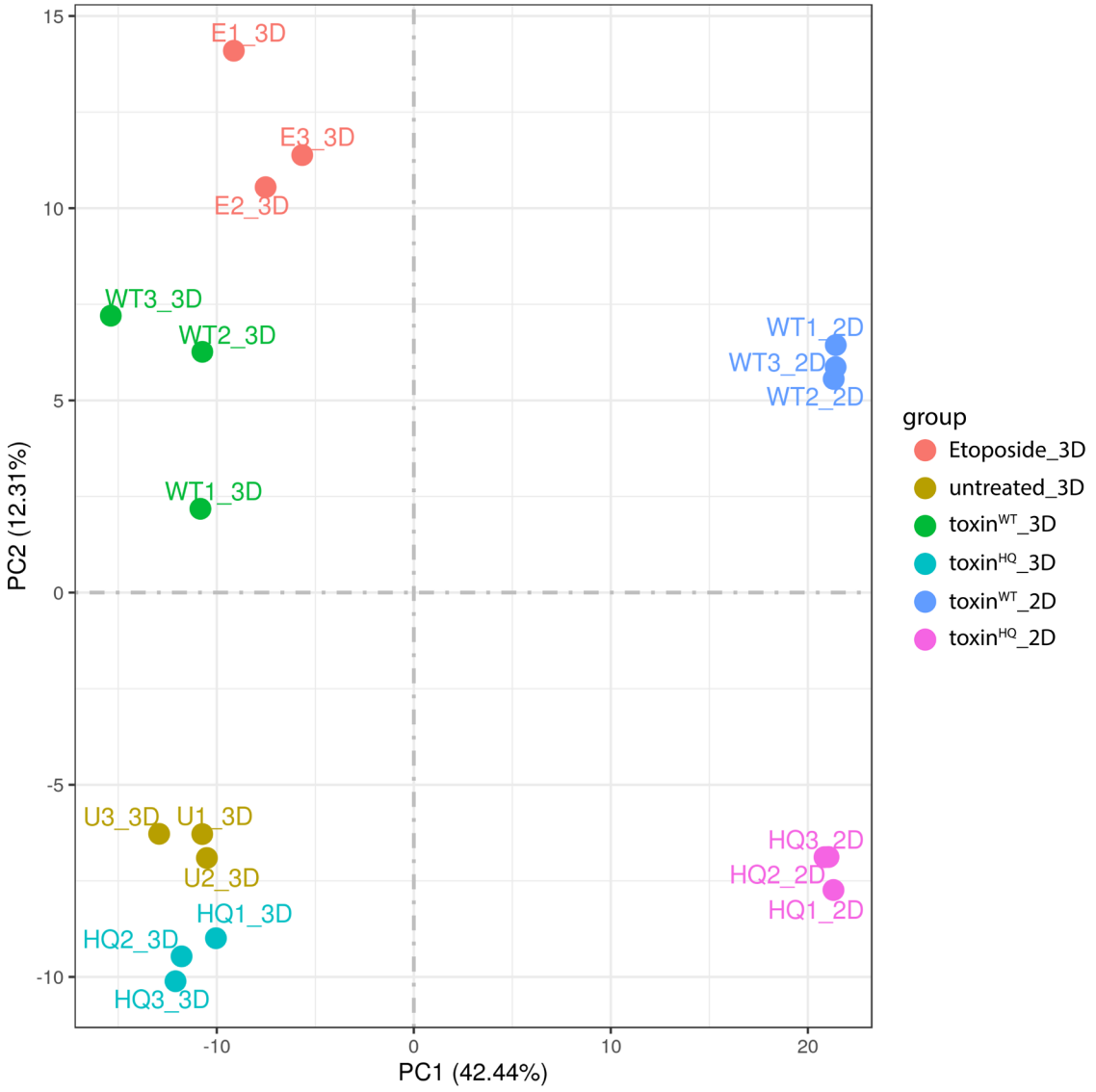

Figure 5.4 Principal Component Analysis of all sample transcriptomes by Novogene. X and Y axes denote the distance of projected values of each data point from the origin (or centre of the dataset) and highlight variation or correlation between samples in terms of their transcriptomes. PC1 accounts for 42.44% of transcriptomic variation around the PC axes, while PC2 accounts for 12.31% of that variation. Colours represent individual sample conditions, and numbers after sample name, e.g., HQ1, HQ2 and HQ3 represent sample replicates.

5.2.4. Co-expression analysis reveals unique hits in 3D Caco-2 transcriptome

To identify uniquely expressed genes within samples, a co-expression analysis was performed by Novogene by selecting genes that had expression levels of more than 1 FPKM. Several genes were co-expressed between samples as depicted in

Venn diagrams by Novogene (**Fig 5.5**). To further look at unique hits expressed by 3D Caco-2 samples that may be involved in polarization, genes commonly expressed by all 3D samples in (**Fig 5.5 B**) were compared with genes discovered in toxin^{WT} and toxin^{HQ}-treated 3D tubes but not in 2D cells (**Fig 5.5 A**), yielding 318 genes uniquely expressed by all 3D Caco-2 tubes (**Table 5.3**).

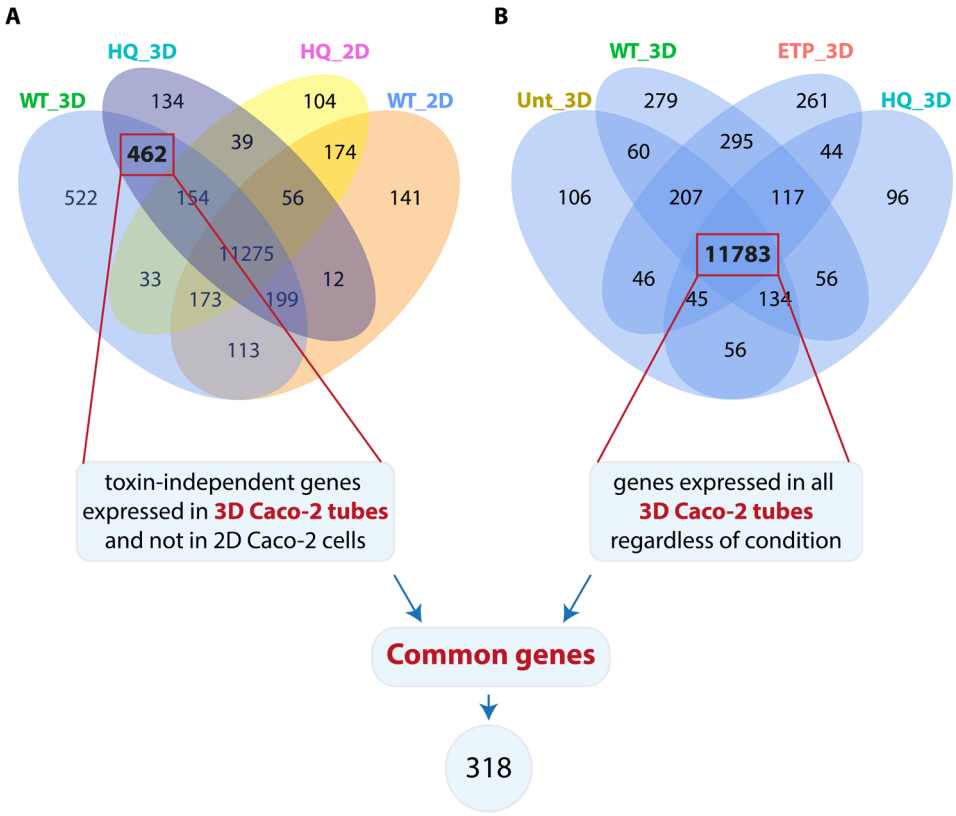

Figure 5.5 Co-expression data by Novogene. (**A**) Venn diagram of genes co-expressed between 2D and 3D Caco-2 samples treated with toxin^{WT} or toxin^{HQ}. (**B**) Venn diagram of genes co-expressed between 3D Caco-2 samples under different conditions (untreated, toxin^{WT}, toxin^{HQ}, and Etoposide-treated).

Genes expressed in all 3D Caco-2 samples but not 2D Caco-2 samples						
PLEKHN1	*PRORSD1P*	*HCG4B*	*TNFRSF11B*	*LINC01559*	*RRN3P1*	*PTK6*
RNF223	*LINC01293*	*TRIM31*	*CASC19*	*HIST4H4*	*SMG1P2*	*SRMS*
MIR34AHG	*FLJ42351*	*C6orf222*	*LDHAP4*	*FAR2*	*FBXL19-AS1*	*AC005391.1*
FAM131C	*MYO7B*	*AL109615.3*	*TTC39B*	*AMN1*	*PRSS36*	*RFX2*
AL451042.2	*LCT*	*ADGRF2*	*RF00019*	*AC048344.4*	*AC026470.2*	*AC008763.1*
ZBTB40-IT1	*CXCR4*	*C6orf141*	*MIR3153*	*DDN*	*MT2A*	*AC006128.1*
AL451139.1	*GAD1*	*AL590652.1*	*MIRLET7D*	*AC026124.2*	*AC012181.2*	*UCA1*
NR0B2	*DNAJC19P5*	*RRAGD*	*AL354726.1*	*FAHD2P1*	*AC009090.6*	*SLC7A9*
GPR3	*RF00134*	*LINC02518*	*RNF183*	*HAL*	*RF00019*	*LGI4*
LAPTM5	*AC013476.1*	*AL023284.4*	*CEL*	*RNY1P16*	*EMC6*	*AC002128.2*
AL365277.1	*SNORA75*	*ZC3H12D*	*CELP*	*NT5DC3*	*SHBG*	*AC022144.1*
MFSD2A	*AQP12B*	*AL353747.3*	*MIR210HG*	*TMEM116*	*ADPRM*	*LGALS7B*
TSPAN1	*VIPR1*	*AC092171.3*	*MIR210*	*TESC*	*PIGL*	*LGALS4*
AL356289.1	*COL7A1*	*AC004130.1*	*AC068580.2*	*HNRNPA3P5*	*RF00019*	*EGLN2*
AL109659.1	*FLNB-AS1*	*AC004593.1*	*SNORA3B*	*AL138689.1*	*SNORD3A*	*AXL*
AC104170.1	*CP*	*RASA4CP*	*SNORA23*	*AL442125.2*	*AC010761.3*	*CEACAM7*
AL139156.2	*TM4SF1-AS1*	*GABPAP*	*AC026250.1*	*SNORA79B*	*SEZ6*	*CEACAM5*
ELOCP19	*LINC01214*	*CCT6P3*	*SBF2-AS1*	*TSSK4*	*AC243732.1*	*ZNF575*
ATXN7L2	*AADACP1*	*AC004980.1*	*RNU7-49P*	*EGLN3*	*TBC1D3L*	*PLAUR*
RNY1P13	*ARL14*	*MIR93*	*AC087276.1*	*RF00019*	*KRT20*	*KCNN4*
CCT8P1	*PLD1*	*TFR2*	*AC090589.3*	*RF00019*	*KRT15*	*RNU6-611P*
MTMR11	*LINC00501*	*MUC17*	*MS4A10*	*AL133299.1*	*RF00004*	*NKPD1*
CIART	*FAM131A*	*LHFPL3-AS2*	*AP001458.1*	*HIF1A-AS2*	*MPP3*	*IGFL2-AS1*
ECM1	*PSMD10P2*	*LINC01004*	*RASGRP2*	*ZBTB25*	*NAGS*	*NPAS1*
RF00405	*AC112907.3*	*CDHR3*	*TMEM151A*	*CLMN*	*AC003070.1*	*CARD8-AS1*
S100A9	*TMEM207*	*SLC26A3*	*C11orf86*	*LINC02320*	*RNU6-826P*	*FAM83E*
BX470102.1	*SLC51A*	*AC000111.2*	*AC004923.1*	*SNORA28*	*AC037487.3*	*SPACA4*
RNU7-57P	*AC096720.1*	*LINC00513*	*BIRC3*	*SNORD116-18*	*CCDC57*	*LHB*
EFNA3	*CXCL2*	*MKLN1-AS*	*AP002800.1*	*AC039056.2*	*NDUFV2*	*SNORD88A*
HSPA6	*MTTP*	*AC009275.1*	*SNORD14E*	*GATM*	*GAREM1*	*GNAZ*
GPA33	*RNU1-138P*	*KDM7A*	*RF00096*	*AC092756.1*	*MAPRE2*	*AP000344.2*
RABGAP1L	*ANKRD37*	*SHH*	*AL365356.4*	*PIGHP1*	*PIK3C3*	*Z95115.1*
PCAT6	*MIR4458HG*	*IL3RA*	*CDNF*	*CA12*	*EBF4*	*TTC28-AS1*

PPFIA4	*FOXD1*	*S100G*	*AL391839.2*	*AC015871.3*	*GNRH2*	*AC003072.1*
RF00019	*SNORA13*	*PHEX*	*ZNF487*	*UBE2Q2P2*	*AL121761.1*	*PIK3IP1*
CAPN8	*AC006077.2*	*PDK3*	*RF00019*	*MIR3174*	*AL117381.1*	*AL022322.1*
SNORA14B	*RNA5SP195*	*SRPX*	*RNU6-883P*	*HAGHL*	*FER1L4*	*Z83840.1*
LINC01954	*RF02039*	*LINC01186*	*KAT6B*	*MSLN*	*TLDC2*	*AL021878.2*
KCNF1	*TIMD4*	*ZNF674-AS1*	*RNA5SP323*	*AC009041.2*	*SNORA71D*	*RF00012*
DNAJC27	*AC008609.1*	*RPL36A*	*AL138921.2*	*SOX8*	*AL021578.1*	*AF124730.1*
PLB1	*CDHR2*	*NUP62CL*	*COL17A1*	*SSTR5*	*PREX1*	*AF064858.2*
AL121658.1	*PPP1R3G*	*XPNPEP2*	*BBIP1*	*AC120498.4*	*UBE2V1*	*AP001469.1*
RF00272	*HIST1H4C*	*MIR503HG*	*AL731566.1*	*AC093525.8*	*ADNP-AS1*	
AC007388.1	*HIST1H4E*	*FMR1-IT1*	*AC005911.1*	*AC004233.2*	*PCK1*	
AC010883.1	*HIST1H3F*	*DKK4*	*APOBEC1*	*TMC7*	*LINC00659*	
AC093110.1	*HIST1H4H*	*PAG1*	*EMP1*	*MIR3680-1*	*BIRC7*	

Table 5.3 List of 318 genes specifically expressed by 3D Caco-2 samples regardless of condition.

Out of these 318 genes involved in Caco-2 polarization, PANTHER (Protein ANalysis THrough Evolutionary Relationships) cellular component analysis revealed 83 genes as entities of the cellular machinery, and 16 genes as part of protein-containing complexes (**Fig 5.6 A**). Moreover, PANTHER protein class analysis (**Fig 5.6 B**) revealed genes such as *LGALS7B* (Galectin-7), *LGALS4* (Galectin-4), *COL7A1* (Collagen alpha-1 (VII) chain) and *COL17A1* (Collagen alpha-1 (XVII) chain) to be involved in the expression of extracellular matrix proteins, which could be indicative of tissue organization in the 3D Caco-2 tubes. Additionally, genes such as *CDHR3* (Cadherin-related family member 3), *CEACAM5* (Carcinoembryonic antigen-related cell adhesion molecule 5), *CDHR2* (Cadherin-related family member 2), *MSLN* (Mesothelin), *CXCR4* (C-X-C chemokine receptor type 4), *CEACAM7* (Carcinoembryonic antigen-related cell adhesion molecule 7) and *CEL* (Bile salt-activated lipase) were classified as those involved in cell adhesion, while genes such as *TIMD4* (T Cell Immunoglobulin and Mucin Domain Containing 4) and *MT2A* (Metallothionein-2) were classified as those involved in the expression of defence/immunity proteins.

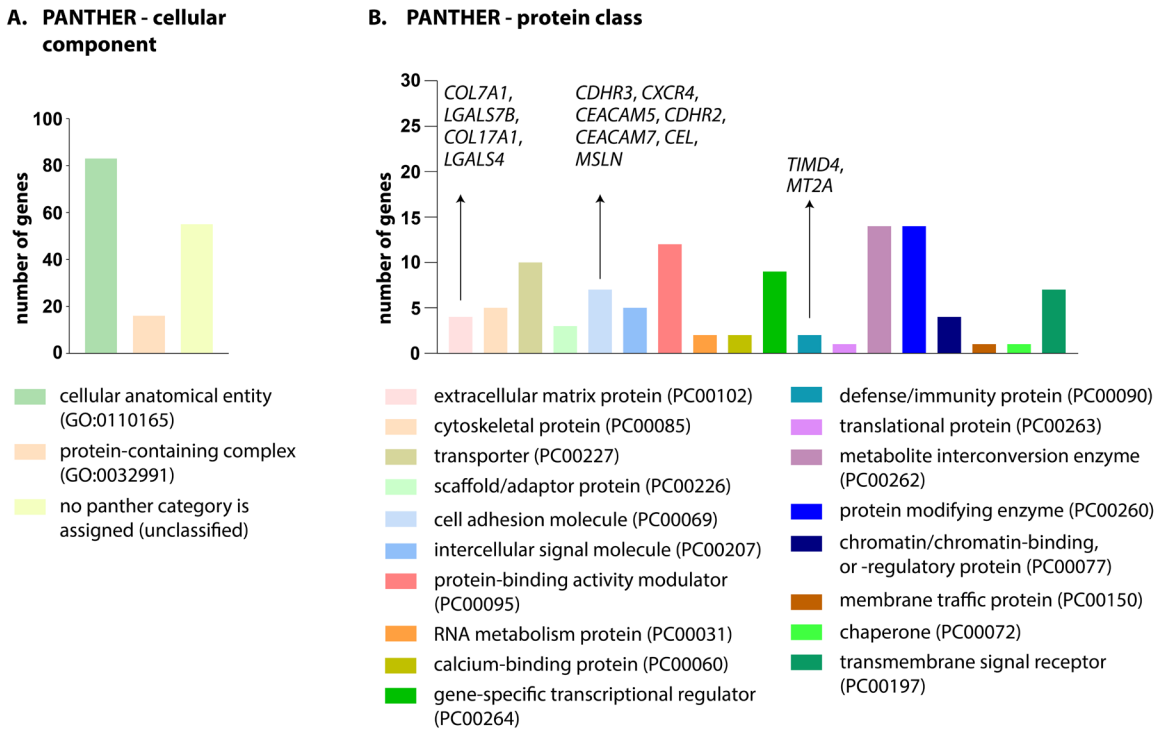

Figure 5.6 PANTHER analysis of uniquely expressed genes in all 3D Caco-2 tubes irrespective of treatment. (**A**) PANTHER analysis of genes listed in table 5.3 for cellular localization (**B**) PANTHER analysis of genes listed in table 5.3 for the protein class that they belong to.

Other genes involved in cellular differentiation (GO:0030154) based on PANTHER biological process analysis are mentioned in **table 5.4**. The conserved expression of these genes across all 3D tubes but not 2D cells could be indicative of differentiation or polarization activity in the 3D model.

gene ID	gene name
FOXD1	Forkhead box protein D1
KRT15	Keratin, type I cytoskeletal 15
AXL	Tyrosine-protein kinase receptor UFO
CDNF	Cerebral dopamine neurotrophic factor
SOX8	Transcription factor SOX-8
PCK1	Phosphoenolpyruvate carboxykinase, cytosolic [GTP]

CXCR4	C-X-C chemokine receptor type 4
KRT20	Keratin, type I cytoskeletal 20
LGI4	Leucine-rich repeat LGI family member 4
EFNA3	Ephrin-A3
SHH	Sonic hedgehog protein

Table 5.4 List of 11 genes involved in cellular differentiation based on PANTHER biological process analysis of genes in table 5.3.

5.2.5. Distribution of differentially expressed genes between sequenced samples

To identify genes whose expression levels were significantly different between samples, differential gene expression analysis was performed by Novogene using DESeq2 software, with a screening threshold of $|\log_2$ fold change$|$ greater than 0 and *p* value less than or equal to 0.05. Transcriptomic comparison of 3D Caco-2 tubes to 2D Caco-2 cells treated with the same toxin, such as toxin^{WT} (**Fig 5.7 G**) or toxin^{HQ} (**Fig 5.7 H**), revealed a high number of differentially expressed genes, i.e., ~9000 to 10,000 with very low p values and high fold changes. However, in comparisons between two samples with the same culture format but treated with either a DDR agent or a negative control for DDR (**Fig 5.7 A, C, D, F**), the total number of differentially expressed genes was lower, i.e ~3500 to 7000. These results align with the PCA data in figure 5.4 where the largest variation in gene expression was due to differences in the culture format of the samples, while the second largest variation was due to differences in DDR responses between the samples. Furthermore, comparisons between negative controls (**Fig 5.7 B**) or between DDR agents (**Fig 5.7 E**) revealed less than ~3000 differentially expressed genes, indicating a modest difference in their transcriptomic profiles.

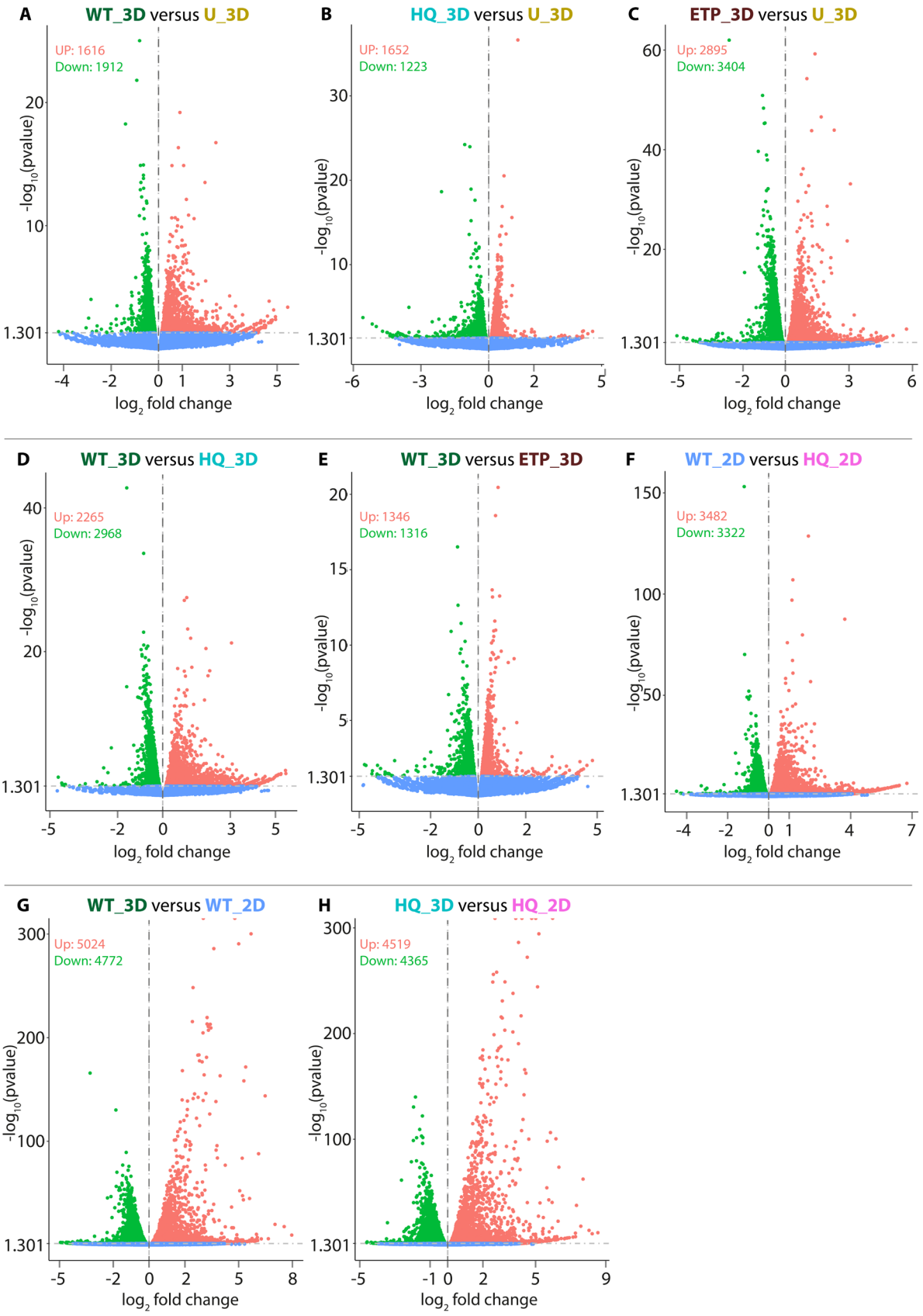

Figure 5.7 Volcano plots generated by Novogene displaying differentially expressed genes between indicated samples. (**A**) toxin^{WT} treated compared to untreated 3D Caco-2 tubes (**B**)

toxin^{HQ} treated compared to untreated 3D Caco-2 tubes (**C**) Etoposide treated compared to untreated 3D Caco-2 tubes (**D**) toxin^{WT} treated compared to toxin^{HQ} treated 3D Caco-2 tubes (**E**) toxin^{WT} treated compared to Etoposide treated 3D Caco-2 tubes (**F**) toxin^{WT} treated compared to toxin^{HQ} treated 2D Caco-2 cells (**G**) toxin^{WT} treated 3D Caco-2 tubes compared to toxin^{WT} treated 2D Caco-2 cells, and (**H**) toxin^{HQ} treated 3D Caco-2 tubes compared to toxin^{HQ} treated 2D Caco-2 cells. X axis depicts $\log_2$ fold change calculated by the DESeq2 software, and Y axis depicts p values on a negative $\log_{10}$ scale. Upregulated genes are in red, while downregulated genes are in green. Genes in blue are those filtered after applying a screening threshold of |log2 fold change| greater than 0 and p value less than or equal to 0.05.

5.2.6. Functional analysis of differentially expressed genes between sequenced samples

Enrichment analyses of differentially expressed genes between RNAseq samples reveal the biological pathways and functions associated with these genes. Thus, GO enrichment analysis was performed by Novogene using differential gene expression data highlighted in the previous section (**Fig 5.7**). In 2D Caco-2 cells, the most significant biological process associated with differentially expressed genes in toxin^{WT}-treated cells relative to mutant toxin^{HQ}-treated cells was cell cycle checkpoint, involving 132 differentially expressed genes (**Fig 5.8 A**). The next highly significant process was type I interferon, followed by type I interferon signalling pathway (**Fig 5.8 A**). On the other hand, in 3D Caco-2 tubes, the most significant biological process associated with differentially expressed genes in toxin^{WT}-treated tubes relative to mutant toxin^{HQ}-treated tubes was sterol biosynthetic process, involving 49 genes (**Fig 5.8 B**). The next most significant process was cholesterol biosynthetic process, followed by RNA localization (**Fig 5.8 B**).

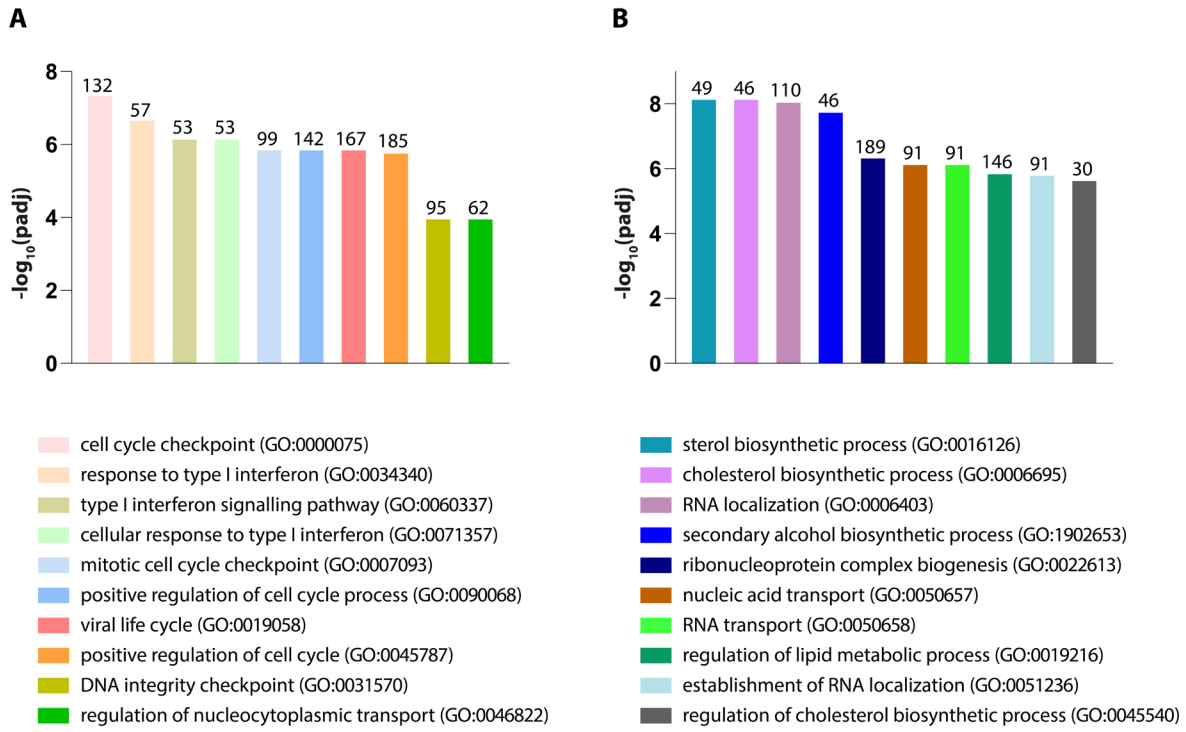

Figure 5.8 GO enrichment analysis for biological processes associated with differentially expressed genes in (**A**) toxin^{WT}-treated 2D Caco-2 cells relative to toxin^{HQ}-treated 2D Caco-2 cells, and (**B**) toxin^{WT}-treated 3D Caco-2 tubes relative to toxin^{HQ}-treated 3D Caco-2 tubes. X axis depicts GO categories of biological processes in order of most significant to least significant. Y axis depicts significance in -log10(padj), where padj is the adjusted p value of the GO category.

5.2.7. Typhoid toxin triggers distinct DDR-driven transcriptomes in 2D and 3D Caco-2 models

Following on from **Figure 5.8**, genes involved in cell cycle regulation were investigated further. As depicted in **Figure 5.9 A**, CDK and cyclin complexes regulate distinct parts of the cell cycle. Entry into S-phase is mediated by phosphorylation of Rb, which drives expression of E2F-regulated genes involved in S phase. Since the typhoid toxin is known to induce cell-cycle arrest via DDRs in mammalian cells (Ibler *et al*., 2019, ElGhazaly *et al*., 2023), it was hypothesised that genes involved in S phase would be repressed in intoxicated host cells relative to negative controls (untreated and toxin^{HQ}-treated), especially in 2D cultures (**Figure 5.8A**). This would likely be coincident with the expression of DDR-mediators such as CDK inhibitors (CDKIs) during cell cycle checkpoints (**Fig 5.9 B**). Hence, in order to examine the

effect of typhoid toxin-induced DDR on cell cycle progression in 2D and 3D Caco-2 models, the differential gene expression patterns of cyclins, CDKs, CDKIs and E2Fs were examined while comparing transcriptomes of intoxicated 2D and 3D Caco-2 samples.

Certain genes were differentially upregulated in a toxin^{WT} dependent manner in both 2D Caco-2 cells and 3D Caco-2 tubes in comparison to toxin^{HQ} (**Fig. 5.9 C**). These include CDKIs such as *CDKN1C* (p57^{Kip2}) and *CDKN1B* (p27^{Kip1}). p57^{Kip2} is known to predominantly inhibit cyclin-CDK complexes of G1/S phase, contributing to G1/S arrest (Rossi and Antonangeli, 2015), while unphosphorylated p27^{Kip1} inhibits CDK2 (Razavipour *et al.,* 2020, Sherr and Roberts, 2004), Notably, cyclin D genes such as *CCND3* (cyclin D3) were upregulated in both models (**Fig. 5.9 C**). *CCND1* (cyclin D1), on the other hand, was upregulated in intoxicated 2D cells, and downregulated in intoxicated 3D tubes (**Fig. 5.9 C**). However, CDKs activated by cyclin D, i.e., *CDK4* and *CDK6* were downregulated by toxin^{WT} in both Caco-2 models (**Fig. 5.9 C**). Furthermore, E2F genes associated with transcriptional repression during and post-S phase, i.e., *E2F4*, *E2F5* and *E2F7* (Kent and Leone, 2019) were also downregulated by toxin^{WT} consistent with cell cycle arrest (**Fig. 5.9 C**).

Certain CDKs involved in the regulation of RNA Polymerase II based transcription such as *CDK13* and *CDK8* (Lim and Kaldis, 2013) were found to be commonly downregulated by toxin^{WT}, while *CCNL2*, an RNA Polymerase II associated cyclin L2 involved in pre-mRNA splicing and apoptosis (Yang *et al.,* 2004), was upregulated in both models in a toxin-dependent manner (**Fig. 5.9 C**). *CDK1*, an E2F target gene and important component involved in G1/S and G2/M progression was also upregulated in both models in response to toxin^{WT} (Wang *et al.,* 2023).

Genes involved in the positive regulation of the Wnt signalling pathway during G2/M phase, such as *CCNY* and *CDK16* (Wang *et al.,* 2016), were found to be downregulated by toxin^{WT} in both models (**Fig. 5.9 C**). Other regulatory genes essential for G2/M progression such as *CDK10* (Guen *et al.,* 2017) were also downregulated in both intoxicated models (**Fig. 5.9 C**).

In terms of differentially expressed genes unique to the intoxicated 2D model, a noteworthy discovery was the downregulation of *CDKN2C* (p18^{INK4c}) and the

upregulation of the p53 effector *CDKN1A* ($p21^{Cip1/Waf1}$) and *CDKN2B* ($p15^{INK4b}$) (**Fig. 5.9 D**). As Caco-2 cells are known to have a point mutation in both alleles of the TP53 gene with a predicted loss of p53 function (Ahmed *et al.,* 2013), *CDKN1A* expression may have been activated through p53-independent pathways (Galanos *et al.,* 2016, Abbas and Dutta, 2009) in intoxicated 2D Caco-2 cells. This data indicates that CDKIs such as $p21^{Cip1/Waf1}$ may play a role in toxin-dependent cell-cycle arrest.

However, many factors associated with cell-cycle progression were upregulated, though they could admittedly be inhibited by CDKIs such as $p21^{Cip1/Waf1}$ as illustrated in **figure 5.9 B**. This included genes involved in both transcriptional activation (*E2F1* and *E2F2*) and repression (*E2F8*) during G1/S transition (Kent and Leone, 2019) which were uniquely upregulated in intoxicated 2D Caco-2 cells (**Fig. 5.9 D**). Additionally, *CDK5*, known to be inactive during cell cycle but involved in DDR and apoptosis in neurons (Batra *et al.,* 2023, Liu *et al.,* 2013) was also upregulated along with multiple cyclins such as *CNNM1* (cyclin M1), *CCNE2* (cyclin E2), *CCNB1* (cyclin B1) and *CCNA2* (cyclin A2) specifically in intoxicated 2D Caco-2 cells (**Fig. 5.9 D**).

In intoxicated 3D Caco-2 tubes, the only CDK inhibitor *INCA1* (inhibitor of CDK interacting with Cyclin A1) was uniquely upregulated (**Fig. 5.9 E**). Cyclins such as *CCNL1* (cyclin L1), *CCNG2* (cyclin G2), *CCNJL* (cyclin J-like) and *CNNM4* (cyclin M4), and CDKs *CDK15*, *CDKL5* and *CDK14* were differentially expressed (**Fig. 5.9 E**).

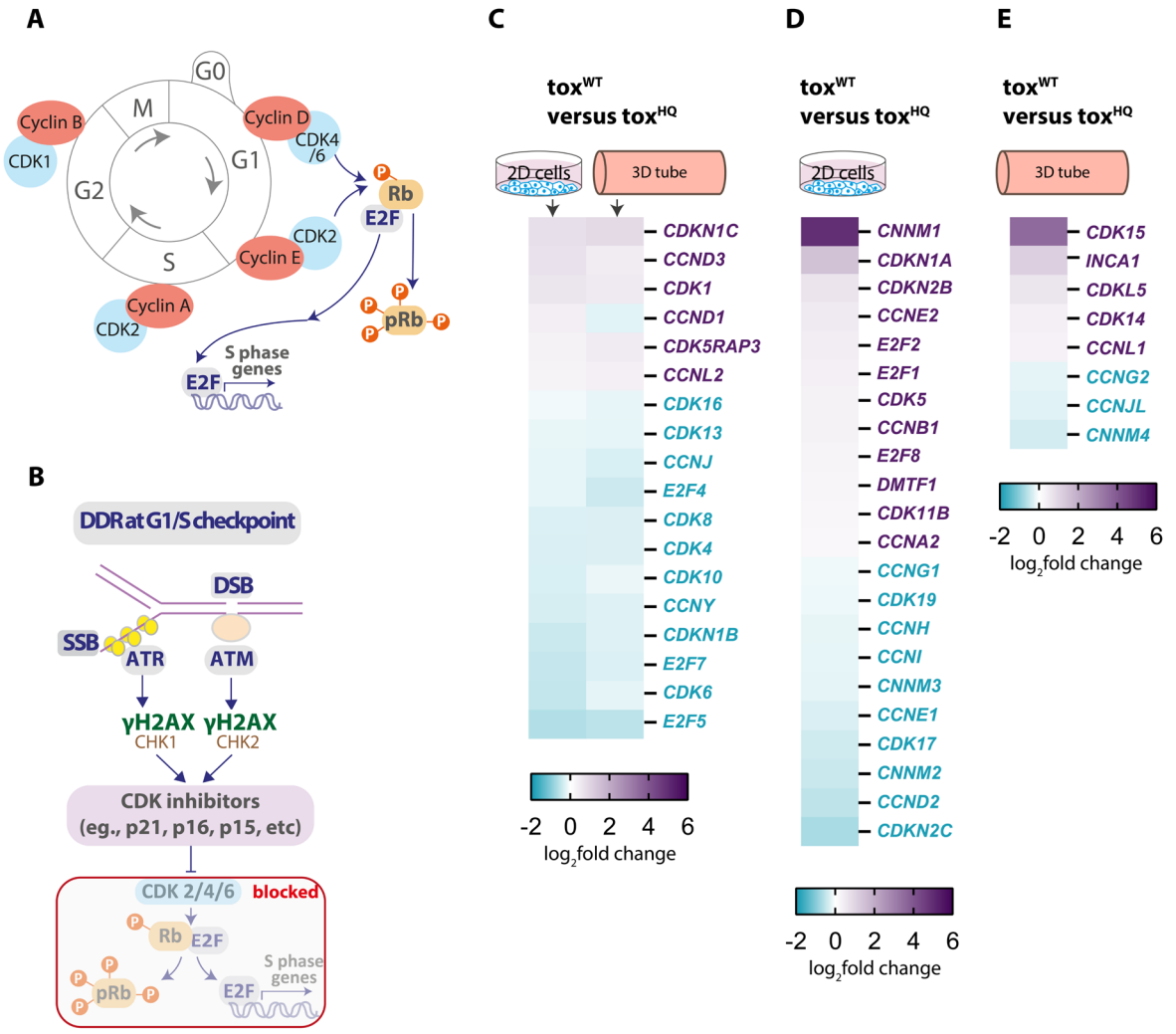

Figure 5.9 Differentially expressed E2F and cyclin-related genes in 2D and 3D Caco-2 models. (**A**) Schematic depicting cell cycle progression through G0, G1, S, G2 and M phase and the cyclins and CDKs involved in each phase. The hyperphosphorylation of Rb by cyclin D-CDK2/4 and cyclin E-CDK2 complexes is a key event for E2F release and G1/S progression. (**B**) DDR at the G1/S cell cycle checkpoint causes the activation of CDKIs, which inactivate CDKs and halt Rb phosphorylation, causing arrest. (**C**) Heatmap of differentially expressed cell cycle genes that are upregulated or downregulated in both toxin^{WT}-treated 2D Caco-2 cells (left) and 3D Caco-2 tubes (right) in comparison to toxin^{HQ}-treated 2D Caco-2 cells(left) and 3D Caco-2 tubes (right). (**D**) Heatmap of differentially expressed cell cycle genes upregulated or downregulated in toxin^{WT}-treated 2D Caco-2 cells in comparison to toxin^{HQ}-treated 2D Caco-2 cells (**E**) Heatmap of differentially expressed cell cycle genes upregulated or downregulated in toxin^{WT}-treated 3D Caco-2 tubes in comparison to toxin^{HQ}-treated 3D Caco-2 tubes. All heatmaps were generated by manually filtering differentially expressed gene lists for cyclin, *CDK*, *CDKI* and *E2F* genes.

5.2.8. Exploring p21$^{Cip1/Waf1}$ activity during toxin-induced DNA damage in 2D and 3D Caco-2 models

The findings in **Fig 5.9** indicate divergent cell-cycle responses to the typhoid toxin, which are difficult to interpret. From **Fig 5.9**, it was hypothesized that 2D Caco-2 cells may be undergoing toxigenic arrest in a p21$^{Cip1/Waf1}$-dependent manner while cell-cycle arrest in 3D Caco-2 tubes may be due to INCA1. A role for p21 was further supported by toxin-induced replication stress and cell cycle arrest in previous studies (Ibler *et al.,* 2019), and the implication of p21$^{Cip1/Waf1}$ in toxigenic cell cycle arrest via Rb dephosphorylation (ElGhazaly *et al.,* 2023) (**Fig 5.9 B**). However, immunofluorescence staining of Caco-2 cells intoxicated with toxin^{WT} (2-hour pulse, 48-hour chase) revealed minimal expression of p21$^{Cip1/Waf1}$ (**Fig 6.0 A** and **B**). This was despite toxin-induced DDRs marked by γH2AX and stalled synthesis of DNA labelled with the nucleotide analogue EdU confirming cell-cycle arrest by toxin^{WT} (**Fig 6.0 A** and **B**). The same trend was also observed with ETP treatment in Caco-2 cells (**Fig 6.0 A** and **B**).

Though p21$^{Cip1/Waf1}$ expression in toxin^{WT}-treated cells was not significantly increased relative to negative controls, it was slightly elevated nonetheless, supporting RNA seq data (**Fig 5.9 D, 6.0 A** and **B**). The role of p21$^{Cip1/Waf1}$ was therefore investigated further by immunoblotting intoxicated cells following p21$^{Cip1/Waf1}$ depletion via siRNA transfection (**Fig 6.0 C**). In all samples without siRNA treatment, p21$^{Cip1/Waf1}$ was beyond detection in the immunoblot, which was in line with immunofluorescence data in **figure 6.0 A**. This made interpretation difficult as siRNA-mediated p21$^{Cip1/Waf1}$ depletion could not be confirmed (**Fig 6.0 C**). Nevertheless, the immunoblot yielded interesting findings. Relative to negative controls (untreated, toxin^{HQ}-treated), both toxin^{WT}-treated and ETP-treated 2D Caco-2 cells transfected with non-targeting siRNA (NT) displayed signs of DDRs as indicated by elevated γH2AX and pCHK2, and cell-cycle arrest as indicated by decrease in phosphorylated Rb$^{Ser807/811}$ (pRb$^{Ser807/811}$). In 2D Caco-2 cells transfected with p21$^{Cip1/Waf1}$ siRNA, pRb$^{Ser807/811}$ remained unchanged in negative controls but increased in cells treated with toxin^{WT} and ETP, indicating G1/S progression due to the presence of p21$^{Cip1/Waf1}$ siRNA. This would likely cause more DNA damage as DNA is more vulnerable during replication, which was

supported by increased γH2AX and pCHK2 in p21$^{Cip1/Waf1}$ siRNA-transfected cells (**Fig 6.0 C**). The effects of p21$^{Cip1/Waf1}$ siRNA transfection in toxin^{WT} and ETP-treated cells (i.e., increased pCHK2 and pRb$^{Ser807/811}$) were ameliorated by chemical inhibition of ATM and ATR kinases. In summary, while p21$^{Cip1/Waf1}$ was beyond detection, immunoblotting phenotypes indicate a role for p21$^{Cip1/Waf1}$ in toxin-driven DDRs and cell-cycle arrest in Caco-2 cells.

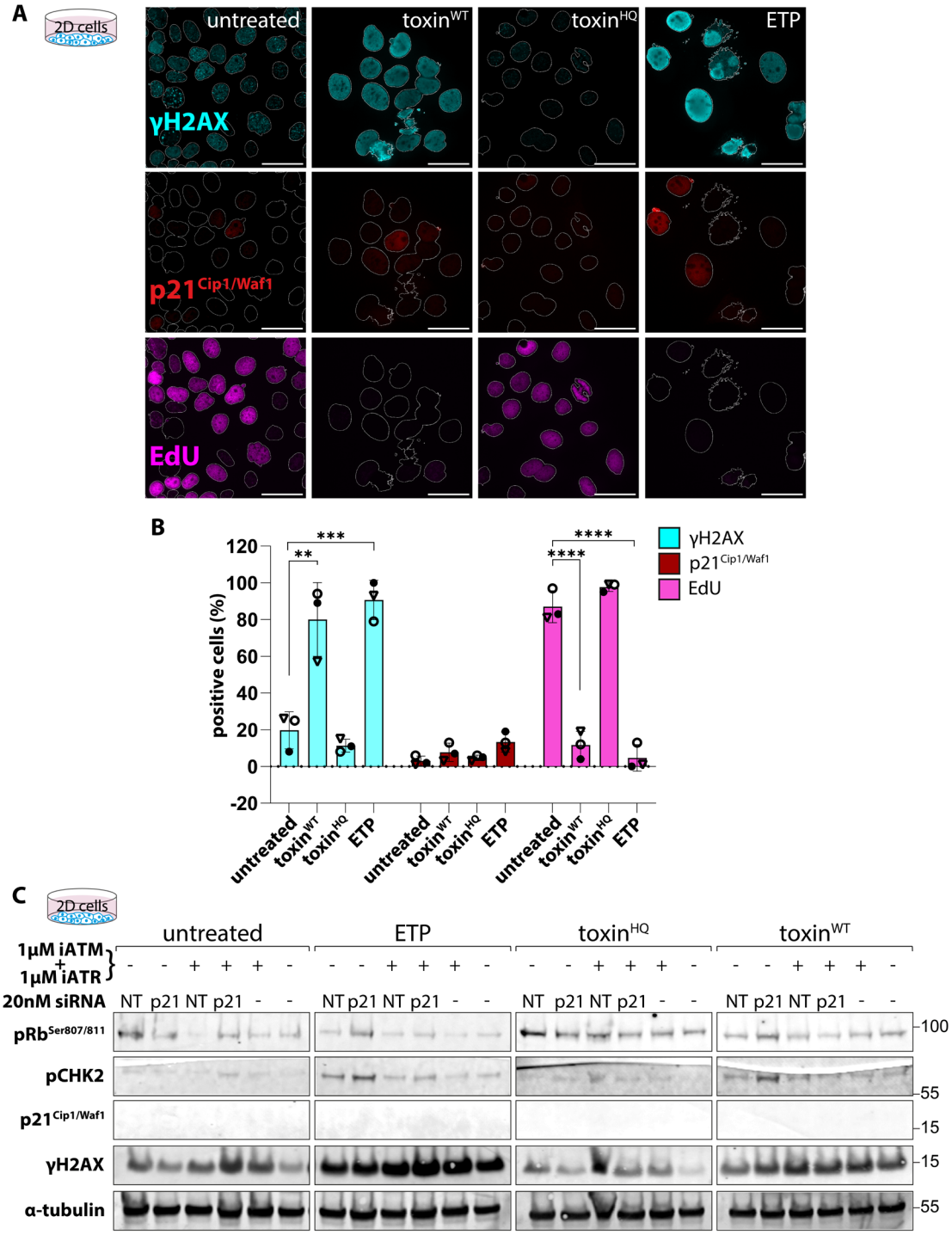

Figure 6.0 Exploring p21$^{Cip1/Waf1}$ activity during toxin^{WT}-induced DNA damage in 2D Caco-2 cells. (**A**) Representative immunofluorescence images showing DAPI (blue), γH2AX (cyan), p21$^{Cip1/Waf1}$ (red) and EdU (magenta) stained nuclei in untreated, toxin^{WT} (20 ng/ml), toxin^{HQ} (20 ng/ml) and ETP (10 μM) treated 2D Caco-2 cells at 48 hours. Cells intoxicated using standard intoxication assay (2-hour pulse, 48-hour chase). EdU incorporation performed 24 hours before fixation. Scale bars 50 μm. (**B**) Quantification of images in (A). Individual points are biological replicates (n=3, ~100 nuclei per condition) represented by a triangle, hollow circle or black dot. Statistical significance determined using one-way ANOVA with Tukey's multiple comparison test. Error bars denote SD. (**C**) Immunoblot of 2D Caco-2 cells intoxicated using standard intoxication assay (2-hour pulse, 48-hour chase) and treated with inhibitors or transfected with siNT or siP21 at indicated concentrations before analysis at 48 hours.

In the case of intoxicated Caco-2 tubes as well, p21$^{Cip1/Waf1}$ expression was minimal and insignificant compared to untreated or toxin^{HQ}-treated controls (**Fig 6.1 A and B**). However, EdU incorporation was reduced in toxin^{WT} and ETP-treated tubes, indicating towards a decrease in cell cycle progression upon DDR activation (**Fig 6.1 A and B**).

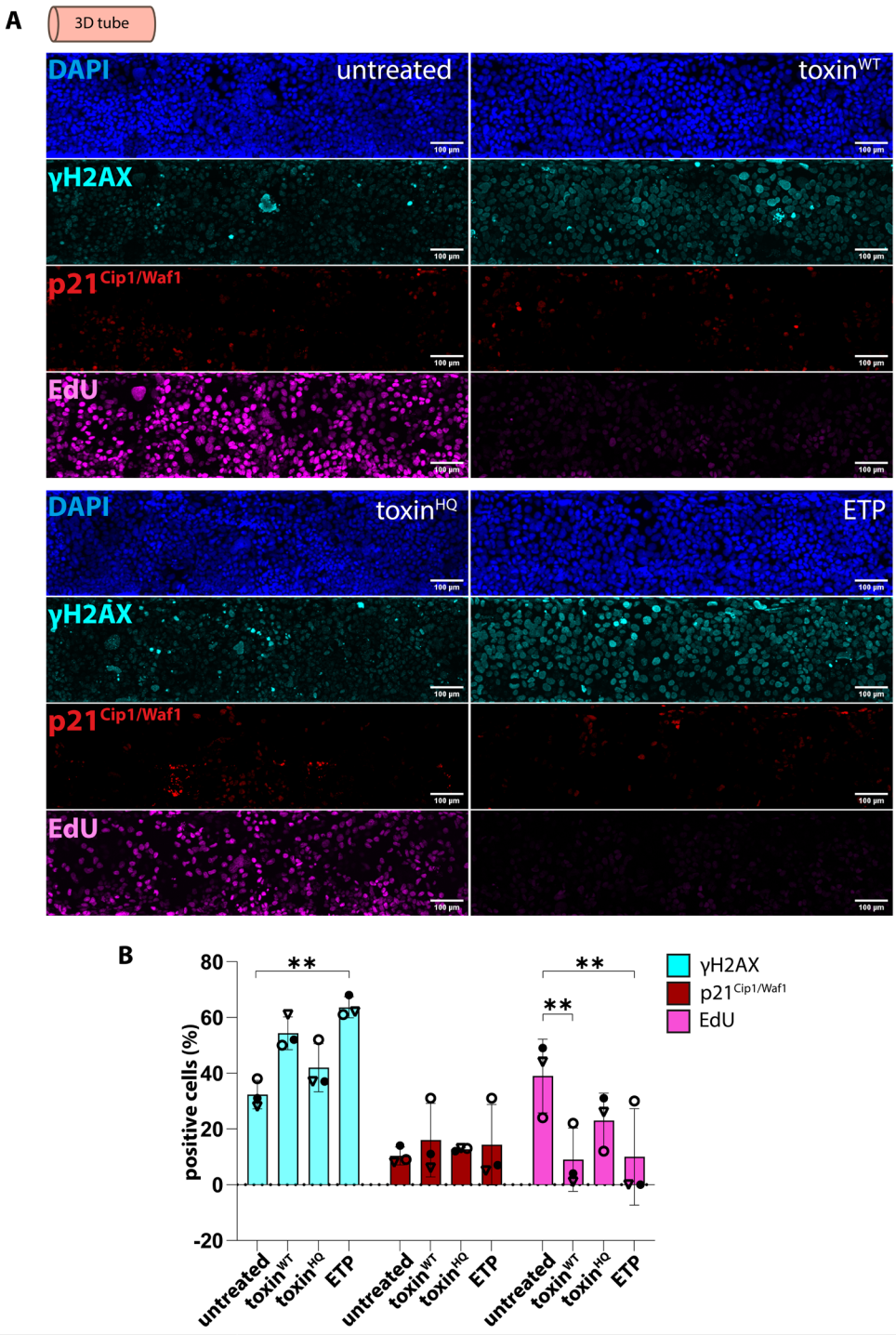

Figure 6.1 Exploring p21$^{Cip1/Waf1}$ activity during toxin^{WT}-induced DNA damage in 3D Caco-2 tubes. (**A**) Representative immunofluorescence images showing DAPI (blue), γH2AX (cyan), p21$^{Cip1/Waf1}$ (red) and EdU (magenta) stained nuclei in untreated, toxin^{WT} (20 ng/ml), toxin^{HQ} (20 ng/ml) and ETP (10 μM) treated 3D Caco-2 tubes at 48 hours. 3D tubes intoxicated using standard intoxication assay (2-hour pulse, 48-hour chase). EdU incorporation performed 24 hours before fixation. Scale bars 100 μm. (**B**) Quantification of images in (A). Individual points are biological replicates (n=3, ~2198 nuclei per condition) represented by a triangle, hollow circle or black dot.

Statistical significance determined using one-way ANOVA with Tukey's multiple comparison test. Error bars denote SD.

5.3. Discussion

Understanding the effect of the typhoid toxin on the host is crucial for investigating its role in the systemic dissemination of typhoidal *Salmonella* and the establishment of enteric fever (Miller *et al.,* 2018, Del Bel Belluz *et al.,* 2016). In the previous chapter, the development of several 3D models was attempted to investigate toxin-induced DDR responses, however, the most optimized model was the Caco-2 gut-on-chip, with polarized cells displaying barrier function and sensitivity to the typhoid toxin (**Chapter 4**, **Fig. 4.2**, **Fig. 4.3 C** and **E**).

This chapter presents differences between Caco-2 tubes and Caco-2 cells in their transcriptomes (**Fig 5.4**), with 318 genes discovered to be uniquely expressed in 3D Caco-2 tubes (**Fig 5.5 A** and **B**) (**Table 5.3**). PANTHER analyses reveal some of these genes, such as *LGALS7B*, *LGALS4*, *COL7A1* and *COL17A1* to be involved in the expression of extracellular matrix proteins (**Fig 5.6 B**), and genes such as *FOXD1*, *KRT15*, *AXL*, *CDNF*, *SOX8*, *PCK1*, *CXCR4*, *KRT20*, *LGI4*, *EFNA3*, and *SHH* in cellular differentiation. However, the influence of these genes at the proteomic level and their role in tube development and polarization is unclear and needs further exploration, as one limitation of transcriptomic analysis is that it does not provide a complete picture of the events that unfold at the translational or post-translational level post transcription. For example, although the expression of tight junction protein *ZO-1* by Caco-2 tubes was not detected at the transcriptomic level (**Table 5.3**), the protein expression of ZO-1 in Caco-2 tubes was distinct as reported in the previous chapter (**Fig 4.2**).

While DNA damage mediated by the typhoid toxin was previously elicited in both 2D Caco-2 cells and 3D Caco-2 tubes (**Chapter 4**, **Fig. 4.3**), this chapter highlights a divergence in toxigenic DDR responses between 2D Caco-2 cells and 3D Caco-2 tubes at the transcriptomic level (**Fig 5.4**). As DDR activation can lead to cell cycle arrest (Cimprich and Cortez, 2008), it was expected for certain CDK inhibitors to be activated in response to toxin-induced damage in the two models. Interestingly, the

CDK inhibitor *CDKN1A* ($p21^{Cip1/Waf1}$) was uniquely upregulated in intoxicated Caco-2 cells, while *INCA1* was uniquely upregulated in Caco-2 tubes in response to the toxin (**Fig 5.9 D** and **E**). However, certain genes were differentially expressed in both intoxicated models, such as *CDKN1C* ($p57^{Kip2}$) (**Fig 5.9 C**). Previous studies in 2D Caco-2 cells treated with mycotoxins show upregulation of CDK inhibitors such as *CDKN2B* ($p15^{INK4B}$), which was also found to be upregulated in Caco-2 cells treated with wild-type typhoid toxin (He *et al.,* 2021). However, previous transcriptomic data on DNA damage responses in Caco-2 tubes could not be found in the literature. Immunofluorescence data from Caco-2 cells revealed a drastic decrease in cell cycle progression in a toxin-dependent manner, despite low detection of $p21^{Cip1/Waf1}$ regardless of treatment (**Fig 6.0 A** and **B**). Furthermore, $p21^{Cip1/Waf1}$ was undetectable in the Caco-2 immunoblot as well (**Fig 6.0 C**), yet upon $p21^{Cip1/Waf1}$ siRNA transfection, an increase in G1/S progression (marked by increased pCHK2 and $pRb^{Ser807/811}$) was observed in a toxin-dependent manner (**Fig 6.0 C**). As the blot was performed only once, it is difficult to interpret if $p21^{Cip1/Waf1}$ expression itself was negligible or if it may be playing a role in mediating DDR-driven cell cycle arrest in 2D Caco-2 cells but was simply undetected due to problems with protein transfer during immunoblotting. Besides collecting additional biological replicates of the immunoblot (**Fig 6.0 C**), *CDKN1A* ($p21^{Cip1/Waf1}$) expression in untreated and siP21-treated samples will also need to be verified via qPCR in order to establish this.

The expression of $p21^{Cip1/Waf1}$ was low in Caco-2 tubes as well, regardless of treatment (**Fig 6.1 A** and **B**). However, these tubes displayed a decrease in cell cycle progression in a DDR-dependent manner. While the underlying cause of this phenomenon could not be investigated due to time constraints, preliminary data obtained via immunofluorescence in these tubes indicate that it may be worth exploring the potential role of CDKIs $p21^{Cip1/Waf1}$, INCA1, or $p57^{Kip2}$ in toxin-mediated arrest in 3D Caco-2 tubes with the help of siRNA treatments, qPCR validation of gene expression and immunoblotting experiments to explore protein expression levels.

Besides cell cycle genes, several genes implicated in innate immune responses were also differentially expressed in intoxicated 2D and 3D Caco-2 models, which are presented in the next chapter.

6. Toxigenic immune responses in 2D versus 3D Caco-2 models

6.1. Introduction

In the previous chapter, the toxin elicited DDR-dependent transcriptional changes in Caco-2 intestinal cells, which differed depending on whether the cells were cultured on a flat 2D plane or 3D polarised tubes within organ-on-chip devices. Furthermore, after cell cycle checkpoint, the most significant biological process associated with differentially expressed genes in toxin^{WT}-treated 2D Caco-2 cells relative to mutant toxin^{HQ}-treated cells was response to type I interferon, which was not the case in toxin^{WT}-treated 2D Caco-2 tubes relative to toxin^{HQ}-treated tubes (**Fig 5.8 A** and **B**). Since the toxin is known to suppress host inflammatory responses and promote systemic *Salmonella* dissemination in mice (Song *et al*., 2013, Lee *et al*., 2020, Del Bel Belluz, *et al.,* 2016), we dived into the RNAseq data of intoxicated 2D and 3D Caco-2 models from the previous chapter (**Fig 5.0**, **Fig 5.7**) to explore any divergence in innate immune responses, before exploring the effect of the typhoid toxin on *Salmonella* survival in each model.

6.2. Results

6.2.1. Typhoid toxin induces distinct innate immune transcriptomes in 2D and 3D Caco-2 models

To investigate how DDRs elicit toxin-driven innate immune responses, specifically anti-microbial and interferon responses, differentially expressed genes in toxin^{WT}-

treated 2D Caco-2 cells relative to toxin^{HQ}-treated cells (**Fig 5.0**, **Fig 5.7**) were filtered for *IFN*, *IRF*, *IFIT* and *IL* genes, as well as potent anti-microbial genes such as *B2M*, defensins, cathelicidins, *APOL3*, *C3* and *LYZ* (Chiou *et al*., 2021, Holch *et al*., 2020, Machado and Ottolini, 2015, Williams *et al*., 2013, Gaudet *et al*., 2021, Nordahl *et al*., 2004, Naveed *et al*., 2023). These genes were then explored in toxin^{WT}-treated 3D Caco-2 tubes relative to toxin^{HQ}-treated tubes to investigate if their differential expression by the typhoid toxin was conserved regardless of cell culture model (**Fig 6.2 A**). The expression of ISGs such as *IRF1/6/8* and members of the *IFIT* family increased in response to typhoid toxin in both 2D and 3D Caco-2 models, despite a lack of interferon (*IFN*) genes themselves. Additionally, cytokine genes such as the interleukin (IL) *IL18* were also differentially expressed in both models in response to the typhoid toxin (**Fig 6.2 A**). As IL-1B and IL-18 are known to be secreted through Gasdermin pores generated following inflammasome activation (Zhou *et al*., 2020, Zito *et al*., 2020), differential gene expression data from toxin^{WT}-treated 2D and 3D Caco-2 samples relative to toxin^{HQ}-treated samples (**Fig 5.7**) was explored for Gasdermin genes as well. Interestingly, *GSDMB* (Gasdermin B) was also upregulated in both 2D and 3D Caco-2 models in response to the typhoid toxin (**Fig 6.2 A**). Moreover, *IL-1B* was upregulated in toxin^{WT}-treated Caco-2 cells (**Fig 6.2 B**).

Anti-microbial genes *B2M* (MHC class 1 component) and *DEFB1* (β-defensin 1) were upregulated in both intoxicated models, however, the ISG *APOL3* and complement *C3* were upregulated in toxin^{WT}-treated 2D Caco-2 cells specifically (**Fig 6.2 B**). While *APOL3* was the most significantly upregulated in toxin^{WT}-treated Caco-2 cells, many other upregulated genes belonged to the IL family or their receptors, and included *IL5, IL1B, IL15, and IL32.* Overall, the number of differentially expressed immune-related genes unique to intoxicated 2D Caco-2 cells were greater than those in intoxicated 3D Caco-2 tubes (**Fig 6.2 B** and **C**). In toxin^{WT}-treated Caco-2 tubes specifically, the anti-microbial gene *LYZ* (lysozyme) was downregulated (**Fig 6.2 C**). In contrast, genes such as the *IFI16* (Interferon Gamma Inducible Protein 16), a sensor of DNA breaks and replication stress (Ka *et al*., 2021) and *LUARIS,* a long noncoding RNA that mediates antiviral responses by regulating ISG expression (Shirahama *et al*., 2020, Suarez *et al*., 2020) were upregulated (**Fig 6.2 C**).

In summary, innate immune responses to toxin nuclease activity were predominantly characterised by IFN-like responses, though model-specific responses were also observed, perhaps most notably the bactericidal *APOL3* gene in toxin^{WT}-treated 2D Caco-2 cells.

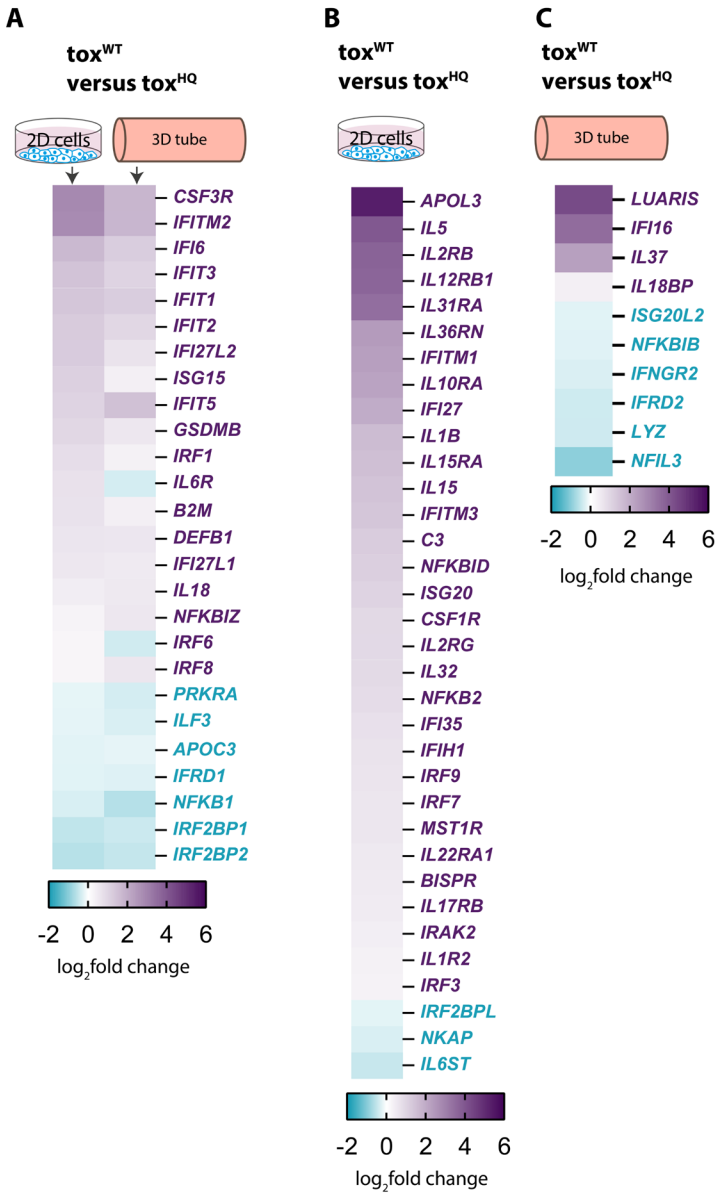

Figure 6.2 Differentially expressed innate immune genes in 2D Caco-2 cells and 3D Caco-2 tubes. (**A**) Heatmap of differentially expressed innate immune genes that are upregulated or downregulated in both toxin^{WT}-treated 2D Caco-2 cells (left) and 3D Caco-2 tubes (right) in comparison to toxin^{HQ}-treated 2D Caco-2 cells (left) and 3D Caco-2 tubes (right). (**B**) Heatmap of differentially expressed innate immune genes upregulated or downregulated in toxin^{WT}-treated 2D Caco-2 cells in comparison to toxin^{HQ}-treated 2D Caco-2 cells specifically (**C**) Heatmap of differentially expressed innate immune genes upregulated or downregulated in toxin^{WT}-treated 3D Caco-2 tubes in comparison to toxin^{HQ}-treated 3D Caco-2 tubes specifically. All heatmaps were

generated by manually filtering differentially expressed gene lists for *IFN*, *IRF*, *IFIT, IL* and *GSDM* genes, as well as potent anti-microbial genes such as *B2M*, defensins, *APOL3*, *C3* and *LYZ*.

6.2.2. Exploring anti-microbial activity in toxin^{WT}-treated in 2D and 3D Caco-2 models

Anti-microbial responses in the gut are known to play an important role in the elimination and prevention of systemic spread of bacteria during NTS infections (Gal-Mor, 2019). However, the role of anti-microbial responses in typhoidal infections are not very well understood. Given that a divergence in innate immune transcriptomes was observed in 2D and 3D Caco-2 models in response to toxin^{WT}, it was hypothesised that there could be differences in their anti-microbial responses as well. Previously, LYZ has been reported as an anti-microbial protein involved in host defences (Naveed *et al*., 2023). The downregulation of *LYZ* in intoxicated Caco-2 tubes led to the hypothesis that the toxin may be playing a role in immunosuppression, which has been previously observed in mouse infection models (Song *et al*., 2013, Lee *et al*., 2020, Del Bel Belluz, *et al.,* 2016). Thus, LYZ activity was further explored via immunofluorescence imaging in 2D and 3D Caco-2 models after intoxicating them with toxin^{WT} or toxin^{HQ} for 2 hours prior to a 48-hour chase. In the case of 2D Caco-2 cells, LYZ was expressed as low intensity puncta across the field of view in untreated and toxin^{HQ} controls, as well in distended toxin^{WT}-treated cells with increased γH2AX phosphorylation (**Fig 6.3 A**). However, in the case of 3D Caco-2 tubes, the amount of LYZ expression was higher in toxin^{WT}-treated tubes compared to untreated and toxin^{HQ} controls (**Fig 6.3 B**). This was surprising as transcriptomic data in **Fig 6.3 C** indicated the opposite was true. Moreover, cells closer to the ECM expressed more LYZ than those near the lumen of the tube in toxin^{WT}- and toxin^{HQ}-treated tubes, indicating towards a polarised expression pattern.

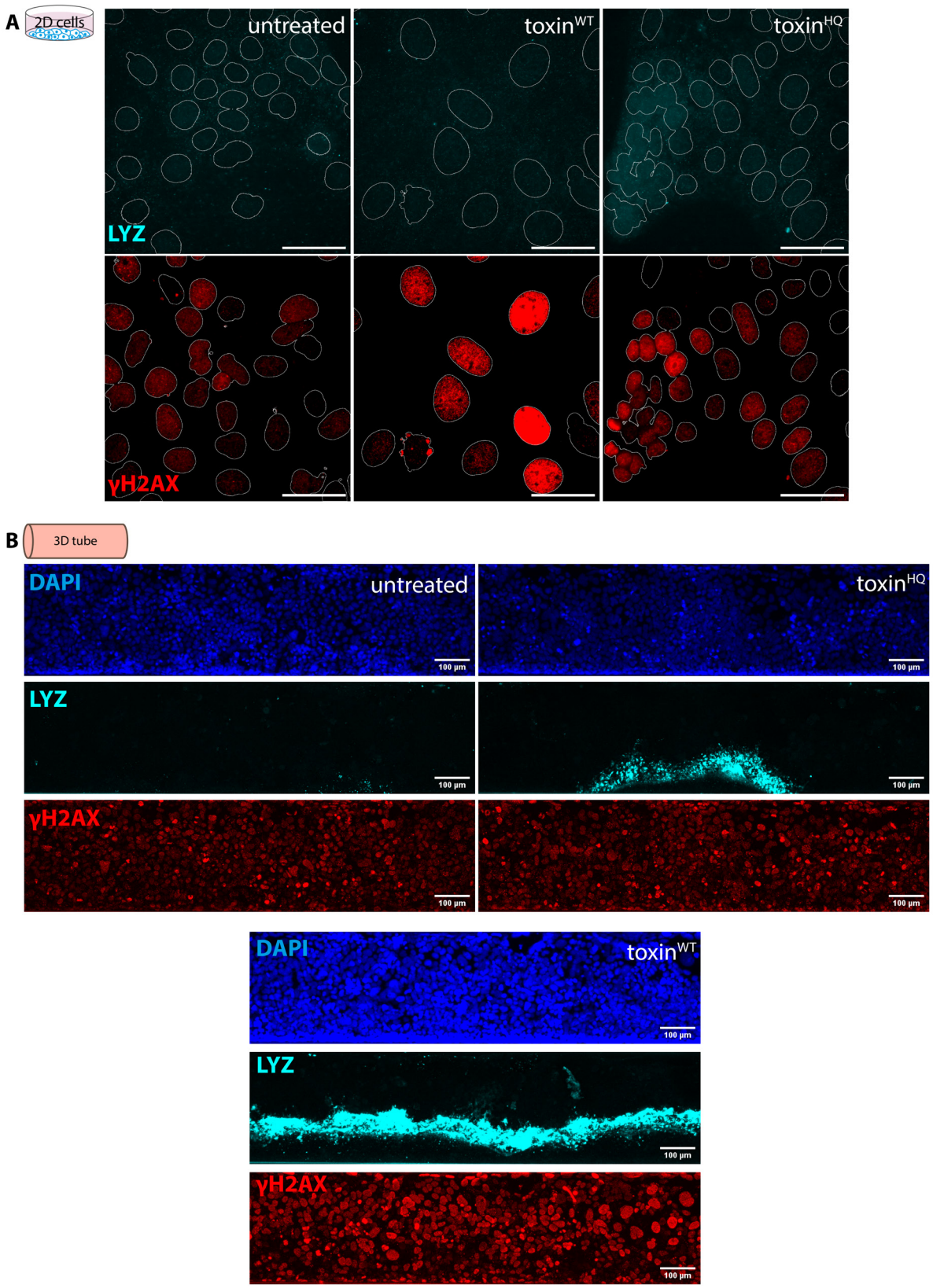

Figure 6.3 LYZ expression is enhanced during toxin^{WT}-induced DNA damage in 3D Caco-2 tubes, but not 2D Caco-2 cells. (**A**) Representative immunofluorescence images showing DAPI (blue), LYZ (cyan), and γH2AX (red) stained nuclei in untreated, toxin^{WT} (20 ng/ml) and toxin^{HQ} (20

ng/ml) treated 2D Caco-2 cells at 48h. Scale bars 50 µm. (**B**) Representative immunofluorescence images showing DAPI (blue), LYZ (cyan), and γH2AX (red) stained nuclei in in untreated, toxin^{WT} (20 ng/ml) and toxin^{HQ} (20 ng/ml) treated 3D Caco-2 tubes at 48h. Scale bars 100 µm. All images are representative of at least 3 biological replicates (n=3).

6.2.3. Exploring toxin effect on *Salmonella* survival in 2D and 3D Caco-2 models

To further explore potential anti-microbial activity elicited by the typhoid toxin in 2D Caco-2 cells and 3D Caco-2 tubes, understanding the influence of the toxin on *Salmonella* survival within host cells was crucial. However, the successful invasion of *Salmonella* pathogens into host cells was essential in order to study their survival post invasion.

Initially, Caco-2 tubes were tested for their susceptibility to *Salmonella* invasion (**Fig. 6.4 A**) using a toxin-deficient NTS *Salmonella* Javiana strain (*S*.J.$^{\Delta cdtB}$), additionally transformed with a GFP reporter plasmid pM975 that is only expressed upon internalization and SCV establishment in cells (Misselwitz *et al*., 2011, Hapfelmeier *et al*., 2005). Upon developing barrier function at day 3, tubes were infected with 20 or 100 multiplicity of infection (MOI) of *S*.J.$^{\Delta cdtB}$ for an hour, before washing and incubating with 10 µg/ml of Gentamicin antibiotic to eliminate extracellular bacteria from re-invading cells. At 4 hours and 24 hours post invasion, tubes were fixed for visualising GFP-positive *S*.J.$^{\Delta cdtB}$ via immunofluorescence imaging. However, no invasion was observed in any of the tubes (**Fig. 6.4 B**).

As Caco-2 tubes have a robust barrier between cells compared to Caco-2 cells scattered on a 2D culture surface, it was predicted that the internalisation of *S*.J.$^{\Delta cdtB}$ would be higher in 2D Caco-2 cultures. To test this, Caco-2 cells were seeded on 2D tissue culture plates pre-coated with rat-tail Collagen I and allowed to recover overnight. The next day, *S*.J.$^{\Delta cdtB}$ MOIs of 10, 100 and 1000 were centrifuged onto the cells at 172 RCF for 1 minute to promote invasion, then incubated with cells for a further 30 minutes. Cells were then washed and treated with an initial pulse of 50 µg/ml Gentamicin for 90 minutes, then washed and treated with 10 µg/ml of the antibiotic for the rest of the experiment (**Fig. 6.4 C**). At 4 hours, 24 hours and 48 hours post

invasion, cells were fixed for visualising GFP-positive *S*.J.$^{\Delta cdtB}$ via immunofluorescence imaging. However, no internalized bacteria were found in any of the samples (**Fig. 6.4 D**). To elucidate if the GFP reporter in *S*.J.$^{\Delta cdtB}$ was defective, HT1080 cells, a fibrosarcoma cell line routinely used by lab members for *Salmonella* infection studies, were infected with an *S*.J.$^{\Delta cdtB}$ MOI of 100 using the same pipeline as **figure 6.4 C**. This time, GFP emitting *S*.J.$^{\Delta cdtB}$ were detected close to the white outlines of cellular nuclei at 24 hours post invasion, indicating that invasion was successful and the GFP reporter was functional (**Fig. 6.4 E**).

Thus, to optimise *S*.J.$^{\Delta cdtB}$ internalization in Caco-2 cells, instead of increasing the MOI of *S*.J.$^{\Delta cdtB}$, the invasion time of *S*.J.$^{\Delta cdtB}$ was increased from 30 minutes to 2 hours or 4 hours (**Fig. 6.4 F**) to create a bigger time frame for bacteria to internalise and establish an SCV successfully. An *S*.J.$^{\Delta cdtB}$ MOI of 100 was centrifuged onto cells at 172 RCF for 1 minute to promote invasion, then incubated with cells for 2 hours or 4 hours. At the end of the 2-hour or 4-hour invasion period, cells were washed and either fixed immediately for visualisation, or continued in culture and treated with an initial pulse of 50 µg/ml Gentamicin for 90 minutes, then 10 µg/ml of the antibiotic until fixation (**Fig. 6.4 F**). In cells infected with *S*.J.$^{\Delta cdtB}$ for 2 hours, the presence of GFP *S*.J.$^{\Delta cdtB}$ was negligible (**Fig. 6.4 G**). However, after chasing the cells for 22 hours, there was an increase in GFP positive *S*.J.$^{\Delta cdtB}$ (**Fig. 6.4 G**). Cells that had been infected with *S*.J.$^{\Delta cdtB}$ for 4 hours, on the other hand, displayed GFP positive *S*.J.$^{\Delta cdtB}$ within cells at 4 hours, with an increase in intracellular bacteria after a 20-hour chase as well, indicating towards *S*.J.$^{\Delta cdtB}$ replication within the SCV (**Fig. 6.4 G**). Given that a centrifugation speed of 172 RCF was used to promote *S*.J.$^{\Delta cdtB}$ invasion, it was hypothesized that increasing this speed to 1000 RCF would further improve *S*.J.$^{\Delta cdtB}$ internalisation into cells during the 2-hour invasion period.

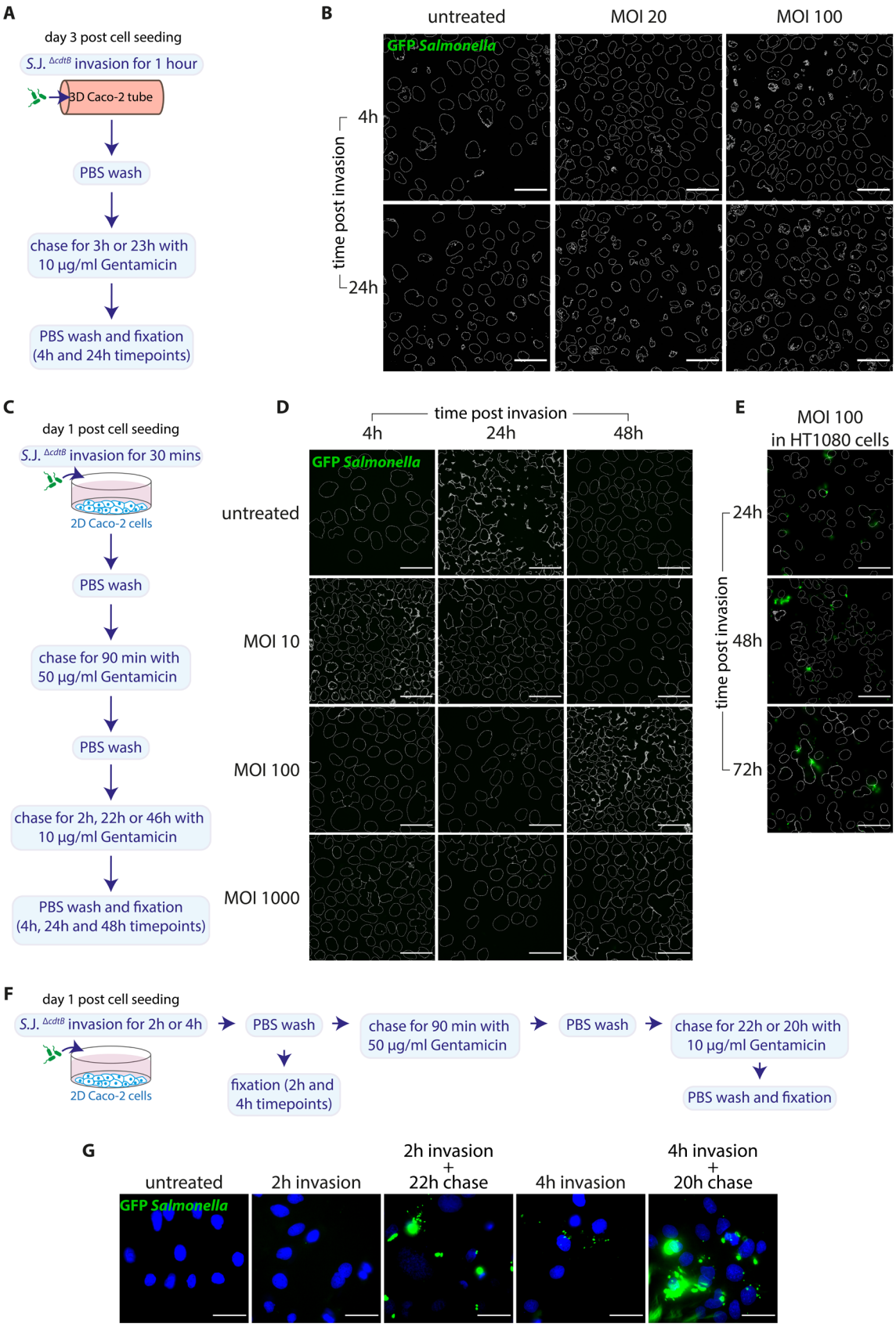

Figure 6.4 Optimising *Salmonella* infections in Caco-2 tubes. (**A**) Experimental plan for infecting 3D Caco-2 tubes (**B**) Fluorescence images showing absence of GFP expressing *S*.J.$^{\Delta cdtB}$

(MOI 20 and 100) in Caco-2 tubes at 4 hours and 24 hours post invasion. Nuclei depicted by DAPI outline (white). (**C**) Experimental plan for infecting 2D Caco-2 cells. (**D**) Fluorescence images showing absence of GFP expressing *S*.J.$^{\Delta cdtB}$ (MOI 10, 100 and 1000) in Caco-2 cells at 4 hours, 24 hours and 48 hours post invasion. Nuclei depicted by DAPI outline (white). (**E**) Fluorescence images of HT1080 cells infected with GFP expressing *S*.J.$^{\Delta cdtB}$ (MOI 100) at 24 hours, 48 hours and 72 hours post invasion. Nuclei depicted by DAPI outline (white). (**F**) Optimised experimental plan for infecting 2D Caco-2 cells (**G**) Fluorescence images of Caco-2 cells with DAPI stained nuclei (blue) and infected with GFP expressing *S*.J.$^{\Delta cdtB}$ (MOI 100) at the indicated timepoints. Scale bars are 50 μm in all images. All images are representative of 3 technical replicates.

To understand the influence of the typhoid toxin on *Salmonella* survival in 2D Caco-2 cells and 3D Caco-2 tubes, both models were treated with the typhoid toxin for 2 hours (pulse), followed by a 48-hour chase to activate the innate immune responses presented in **Fig 6.2**. The toxin^{WT}-treated models were then infected with 100 MOI of NTS *S*.J.$^{\Delta cdtB}$ for 2 hours. In the case of 2D Caco-2 cells, *S*.J.$^{\Delta cdtB}$ was centrifuged onto the cells for 1 minute at 1000 RCF before incubating with cells for 2 hours (**Fig 6.5 A**). After 2 hours or 24 hours post-invasion, the two models were lysed with detergent and the *Salmonellae* cultured on LB agar plates for CFU counts to assess *S*.J.$^{\Delta cdtB}$ internalisation (**Fig 6.5 A**). For this infection experiment, the toxin-deficit *S*.J.$^{\Delta cdtB}$ strain was chosen to avoid additional toxin activity and complications in interpretation.

At 2 hours post internalisation, CFU counts from each sample were normalized to CFUs from samples treated with *S*.J.$^{\Delta cdtB}$ only (control) for examining relative invasion between samples. The relative survival of *S*.J.$^{\Delta cdtB}$ in each sample at 24 hours was determined by normalizing CFU counts in that sample to their CFU counts at 2 hours, before normalizing to the control CFUs at 24 hours. In 2D Caco-2 cells, the invasion of *S*.J.$^{\Delta cdtB}$ at 2 hours varied slightly between samples pre-treated with toxin$^{WT/HQ}$ or ETP in comparison to control samples and there was no significant difference (**Fig 6.5 B**). Thus, toxin-induced immune responses did not affect *Salmonella* invasion. At 24 hours post invasion, *S*.J.$^{\Delta cdtB}$ survival decreased significantly in 2D Caco-2 cells pre-treated with toxin^{WT} or ETP relative to control samples, indicating towards anti-microbial activity in the intoxicated cells (**Fig 6.5 C**).

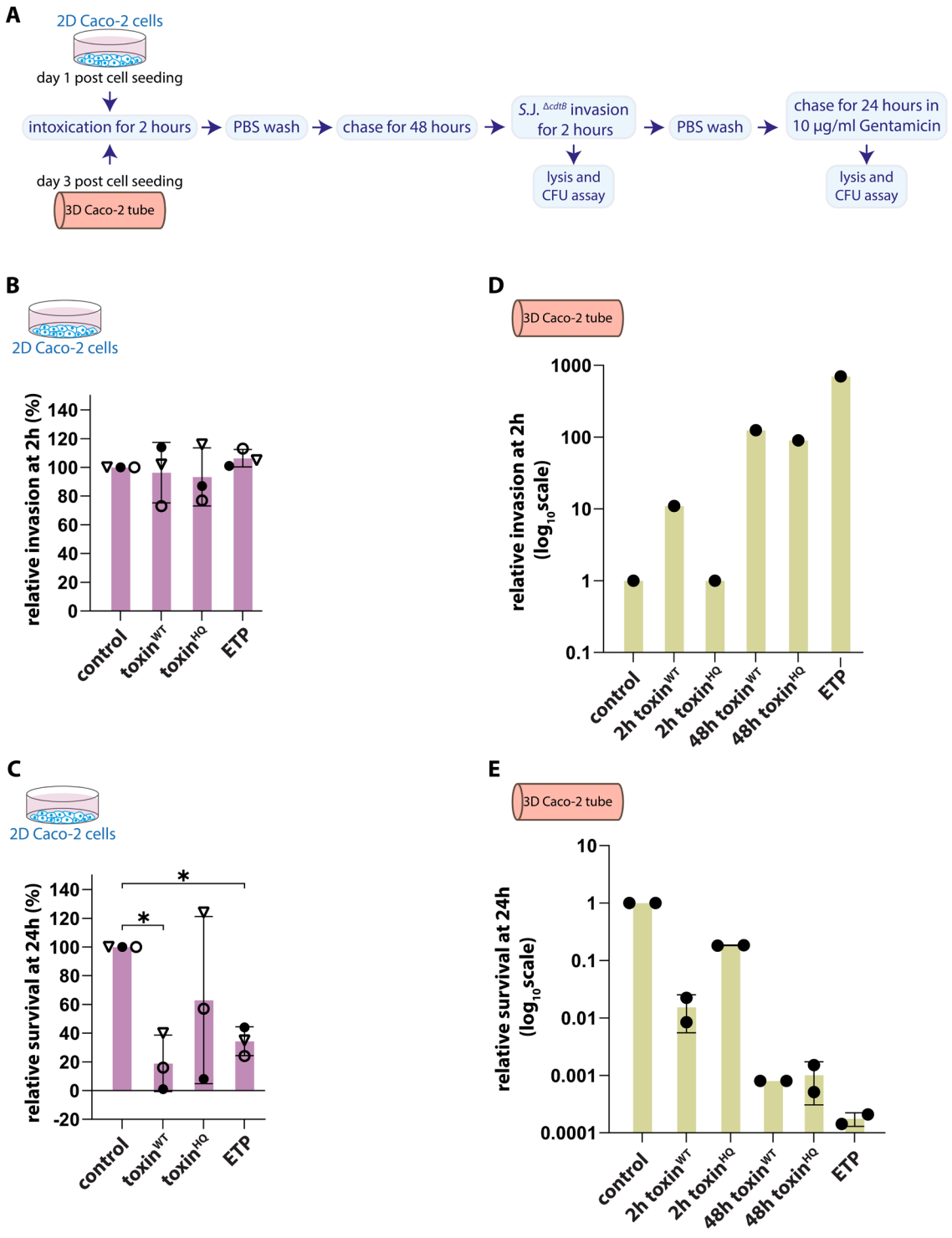

Figure 6.5 Exploring toxin effect on *Salmonella* survival in 2D and 3D Caco-2 models. (**A**) Schematic of the infection experiment in both 2D and 3D Caco-2 models. After 2 hours of *S*.J.$^{\Delta cdtB}$ invasion, culture medium was washed off and replaced with fresh medium containing 10 µg/ml of Gentamicin antibiotic to prevent extracellular *S*.J.$^{\Delta cdtB}$ replication or re-invasion into Caco-2 cells or tubes (**B**) Quantification of intracellular *S*.J.$^{\Delta cdtB}$ CFUs at 2 hours post invasion in toxin^{WT} (20 ng/ml), toxin^{HQ} (20 ng/ml) and ETP (10 µM) treated 2D Caco-2 cells relative to cells treated with

S.J.$^{\Delta cdtB}$ only (control). Individual points are biological replicates (n=3) represented by a triangle, hollow circle or black dot. Error bars depict SD. (**C**) Quantification of intracellular *S*.J.$^{\Delta cdtB}$ CFUs at 24 hours post invasion in toxin^{WT} (20 ng/ml), toxin^{HQ} (20 ng/ml) and ETP (10 μM) treated 2D Caco-2 cells relative to cells treated with *S*.J.$^{\Delta cdtB}$ only (control). CFUs are normalised to CFUs at 2 hours. Individual points are biological replicates (n=3) represented by a triangle, hollow circle or black dot. Statistical significance determined using RM one-way ANOVA with Tukey's multiple comparison test. Error bars depict SD. (**D**) Quantification of intracellular *S*.J.$^{\Delta cdtB}$ CFUs at 2 hours post invasion in toxin^{WT}-treated (20 ng/ml, 2-hour or 48-hour pulse), toxin^{HQ}-treated (20 ng/ml, 2-hour or 48-hour pulse) and ETP (10 μM) treated 3D Caco-2 tubes relative to tubes treated with *S*.J.$^{\Delta cdtB}$ only (control). Individual points are an average of two technical replicates (n=1) represented by black dots. (**E**) Quantification of intracellular *S*.J.$^{\Delta cdtB}$ CFUs at 24 hours post invasion in toxin^{WT}-treated (20 ng/ml, 2-hour or 48-hour pulse), toxin^{HQ}-treated (20 ng/ml, 2-hour or 48-hour pulse) and ETP (10 μM) treated 3D Caco-2 tubes relative to tubes treated with *S*.J.$^{\Delta cdtB}$ only (control). CFUs are normalised to CFUs at 2 hours. Individual points are technical replicates (n=1) represented by black dots. Error bars depict SD.

In the case of 3D Caco-2 tubes, *S*.J.$^{\Delta cdtB}$ internalisation at 2 hours differed greatly, with at least a 10-fold difference between samples pre-treated with toxin^{WT} or ETP in comparison to control or toxin^{HQ}-treated samples (**Fig 6.5 D**). Interestingly, upon prolonging toxin$^{WT/HQ}$ pulse from 2 hours to 48 hours before infection, *S*.J.$^{\Delta cdtB}$ invasion increased by 10-fold in both samples (**Fig 6.5 D**). At 24 hours post invasion, *S*.J.$^{\Delta cdtB}$ survival was reduced in tubes pre-treated with toxin^{WT} or ETP in comparison to control or toxin^{HQ}-treated tubes (**Fig 6.5 E**). However, upon increasing toxin$^{WT/HQ}$ pulse from 2 hours to 48 hours before infection, *S*.J.$^{\Delta cdtB}$ burden was reduced even further, with minimal difference in *S*.J.$^{\Delta cdtB}$ burden between tubes pre-treated with toxin^{WT} and null toxin^{HQ} for 48 hours (**Fig 6.5 E**), indicating that prolongation of toxin$^{WT/HQ}$ pulse from 2 hours to 48 hours decreased *S*.J.$^{\Delta cdtB}$ burden regardless of toxin^{WT} nuclease activity. However, more biological replicates would be needed to validate these findings.

6.3. Discussion

The typhoid toxin has previously been shown to upregulate interferon regulated genes in mice colon and liver tissues (Del Bel Belluz *et al*., 2016). This chapter presents the effect of the typhoid toxin on innate immune responses and *Salmonella* survival in 2D Caco-2 cells and 3D Caco-2 tubes. Besides divergent DDR responses,

RNAseq data also revealed divergence in immune responses between 2D Caco-2 cells and 3D Caco-2 tubes in response to the toxin^{WT} (**Fig 6.3**). Notably, the number of interleukin, interferon and ISG-related genes upregulated in 2D Caco-2 cells was higher than those upregulated in 3D Caco-2 tubes in response to the toxin^{WT} (**Fig 6.3 B** and **C**). The anti-microbial *APOL3* was the most upregulated in 2D Caco-2 cells in response to the toxin^{WT}, while *LYZ*, the only anti-microbial gene differentially expressed in 3D Caco-2 tubes, was downregulated in response to the toxin^{WT}. Given the immunomodulatory role of the typhoid toxin to promote *Salmonella* dissemination and persistence, such as decreasing neutrophil count in mice upon intravenous injection or oral challenge, reducing recruitment of macrophages in mouse intestinal mucosa and reducing typhoid fever symptoms in human challenge models (Song *et al*., 2013, Lee *et al*., 2020, Del Bel Belluz, *et al.,* 2016), it was interesting to find an increase in LYZ expression in a toxin-dependent manner specifically in 3D Caco-2 tubes (**Fig 6.4 B**). However, the amount of LYZ expressed and secreted in each model in response to the toxin^{WT} will need further investigation and quantification, for example through ELISA assays.

The typhoid toxin was also observed to reduce intracellular NTS *S*.J.$^{\Delta cdtB}$ burden in both 2D Caco-2 and 3D Caco-2 models, indicating towards similarity in anti-microbial responses in the two models (**Fig 6.5**). This contradicts previous studies where the typhoid toxin has been reported to enhance cellular susceptibility to *S.* Javiana invasion (ElGhazaly *et al*., 2023, Ibler *et al.,* 2019). However, additional biological replicates need to be obtained to strengthen findings in terms of statistical significance. Moreover, experiments with typhoidal strains of *Salmonella* may prove more insightful in understanding how TS invasion during enteric fever may be influenced by toxin^{WT} activity in 2D and 3D Caco-2 models, as TS strains are known to be more invasive than NTS strains (Dougan and Baker, 2014, Gal-Mor, 2019).

Part III: Discussion

7.1. General conclusions

This study aimed to establish a 3D human gut-on-chip model to study host responses to the typhoid toxin and their role in *Salmonella* survival. The gut-on-chip model was developed using human adenocarcinoma cell lines such as Caco-2 and DLD-1 cells, and human primary intestinal cells from biopsy-derived colon organoids. Caco-2 gut-on-chips were found to be the most sensitive to the typhoid toxin, while other 3D gut-on-chips required more optimization to model toxin-driven DDR responses. Caco-2 tubes were investigated further for their DDR and innate immune responses to the toxin at the transcriptional level. Distinct transcriptomes were found to be elicited by the toxin in 3D Caco-2 tubes in comparison to 2D Caco-2 cells cultured on a flat plane. Regardless, the toxin reduced intracellular NTS *Salmonella* burden in both 3D and 2D Caco-2 models.

7.2. Development of various gut-on-chip models for typhoid toxin studies

Host-restricted pathogens such as typhoidal *Salmonella* are difficult to study in animal models such as mice due to their low survival rates (Hedlund *et al*., 2007, Deng *et al*., 2014). Humanised mice engrafted with human hematopoietic stem cells are emerging models for studying chronic *S*. Typhi infections, although interactions between human immune cells and *S*. Typhi dissemination are difficult to interpret due to a limited influence of human cytokines on mouse tissues (Song *et al*., 2010). Human challenge models are subject to stringent regulations, which limit infection times,

infection doses and subsequent interpretations (Gibani *et al*., 2019). Organoid studies such as early *S*. Paratyphi infection studies in human gallbladder organoids, and *S*. Typhimurium infection studies in human primary gut organoids have increased our understanding of host-pathogen interactions (Lees *et al*., 2019, Sepe *et al*., 2020, Geiser *et al*., 2021). However, owing to the spherical structure of these gut organoids, the enclosed lumen cannot be accessed very easily and requires sophisticated equipment for microinjecting pathogens into the lumen (Geiser *et al*., 2021). On the other hand, polarized cells in 2D monolayers or mucosoids using human gall bladder organoids can be easily infected for *S*. Paratyphi A studies but do not mimic the spatial cellular organisation observed *in vivo* (Sepe *et al*., 2020).

Organ-on-chip technologies are an emerging arena for modelling human-specific diseases and can be modified in extensive ways, for example to develop co-cultures of different cell types or tissues for long-term studies. Additionally, they require low volumes of culture media due to their microfluidic design and can mimic the spatial organisation of tissues *in vivo* (Trietsch *et al*., 2017). The typhoid toxin has not been previously studied in a 3D gut-on-chip model, which makes our findings novel and distinct, and provides groundwork for future studies in typhoidal *Salmonella* infections using gut-on-chip cultures.

3D gut-on-chips derived from intestinal cell lines such as Caco-2 cells develop barrier function in 3 days and sooner than conventional transwell Caco-2 cultures due to fluid flow or perfusion (Trietsch *et al*., 2017). However, while this study employed the use of 150kDa of FITC-dextran dye for 3D gut-on-chip development, using a smaller size of the dye such as 4 kDa would help assess the barrier integrity of these models more stringently, in addition to routine barrier integrity assays such as TEER (Nicolas *et al*., 2020).

While Caco-2 tubes are more sensitive to the typhoid toxin than DLD-1 tubes, DLD-1 tubes are useful for studying the effects of typhoid toxin on potential p53 responses during DNA damage (**Fig 4.6**), as DLD-1 cells express a mutant form of the p53 tumour suppressor protein unlike Caco-2 cells (Lane *et al.,* 1990, Ookawa *et al.,* 2002, Thant *et al*., 2008).

However, since both Caco-2 and DLD-1 cell lines lack diversity in epithelial cell types found in the human intestine such as goblet cells, Paneth cells, intestinal stem cells and enteroendocrine cells, primary gut-on-chips derived from intestinal organoids are an emerging tool for modelling gastrointestinal disease such as IBD by co-culturing them with monocyte-derived macrophages in a single chip in the 3-lane OrganoPlate® (Beaurivage *et al*., 2020).

Before modelling toxin-mediated responses in the primary gut-on-chip, it was important to first determine the toxin dose required for eliciting DDRs in primary colon cells. Results from **chapter 4** showed primary colon cells cultured on a 2D plane to be resistant to the toxin^{WT} at 20 ng/ml and 100 ng/ml when incubated for 2 hours. Given that 20 ng/ml of toxin^{WT} generated DDRs in DLD-1 tubes when incubated for 48 hours instead of 2 hours, increasing the time period of intoxication in primary colon cells may allow more time for the toxin to trigger DDRs in them.

Previous studies have shown the expression of stem cell marker LGR5 in gut organoid cultures when grown in basement membrane extracts such as Matrigel or Cultrex gel (Sato *et al*., 2009). On the other hand, the primary-gut-on-chip using the OrganoPlate® showed an upregulation in differentiation genes and downregulation in the stem cell marker *LGR5* at 8 days post cell seeding (Beaurivage *et al*., 2020). While the effect of *LGR5* downregulation on self-renewal or long-term maintenance of the primary gut-on-chip has not yet been investigated, the downregulation of *LGR5* in the primary gut-on-chip as reported by Beaurivage *et al* in 2020 may be due to the lack of Cultrex gel used to support the attachment, growth, and polarization of cells in the gut-on-chip. This thesis used a modified gut-on-chip culture protocol by pre-coating the cell seeding channel of the OrganoPlate® with Cultrex gel prior to seeding cells, while using ECM in the ECM channel to support the growth of the primary gut-on-chip (**Fig 4.9 B** and **C**). Further investigation is needed to assess if barrier function can be maintained longer than 8 days post cell seeding, however, the primary gut-on-chip is a promising arena for modelling typhoid toxin and/or long-term typhoidal *Salmonella* infections in the future.

7.3. Distinct transcriptomic responses to the typhoid toxin in 3D Caco-2 tubes and 2D Caco-2 cells

The typhoid toxin caused DNA damage in both 3D Caco-2 tubes and 2D Caco-2 cells cultured on a 2D surface (**Chapter 4**, **Fig. 4.3**). Upon deeper investigation, the toxin was shown to cause a divergence in transcriptional responses in the two models. As described in **chapter 5**, functional analysis of genes differentially regulated by the toxin^{WT} in 2D Caco-2 cells showed cell cycle checkpoint and response to type I interferon as the two most significant biological processes associated with these genes. On the other hand, the two most significant processes associated with differentially expressed genes in toxin^{WT}-treated tubes relative to mutant toxin^{HQ}-treated tubes were sterol biosynthetic process and cholesterol biosynthetic process.

Sterols are lipid molecules, the most important of them being cholesterol, and their biosynthesis is often hijacked during cancer progression (Feltrin *et al.*, 2020). Cholesterol biosynthesis in particular is part of the lipid anabolism pathway, and its induction has been reported to promote DNA damage and cellular senescence in mammalian cells (Ziegler *et al.*, 2024). Additionally, cholesterol accumulation in the mitochondria due to dysregulated synthesis has been reported to induce inflammasome activation in mouse macrophages (Dang *et al.*, 2017). In the context of typhoidal *Salmonella* pathogenesis, it could be that activation of the cholesterol biosynthesis pathway by the typhoid toxin may benefit the host in eliminating invading pathogens, or it may act as a hijack target for the toxin to promote DNA damage, senescence and *S*. Typhi invasion into macrophages in the intestinal mucosa to enable dissemination via infected macrophages in the bloodstream. This could be tested in a 3-lane organ-on-chip system by co-culturing primary gut-on-chips in the first channel with macrophages embedded in the ECM or the middle channel, and endothelial cells in the third channel. Typhoidal strains such as *S*. Paratyphi A could be infected in the primary gut-on-chip to test if the pathogens cross the gut barrier into the ECM and infect macrophages, and if the infected macrophages migrate towards the endothelial barrier in the third channel.

Differentially expressed genes particularly involved in cell cycle regulation and innate immunity were also examined for their differences in regulation between 2D and 3D Caco-2 models in response to the toxin. The CDK inhibitor *CDKN1A* ($p21^{Cip1/Waf1}$) was uniquely upregulated in intoxicated 2D Caco-2 cells, while *INCA1* was uniquely upregulated in Caco-2 tubes in response to the toxin (**Fig 5.9 D** and **E**). However, certain genes were differentially expressed in both intoxicated models, such as *CDKN1C* ($p57^{Kip2}$) (**Fig 5.9 C**). Despite minimal expression in response to the toxin, $p21^{Cip1/Waf1}$ was observed to play a role in mediating DDR-driven cell cycle arrest in 2D Caco-2 cells. Indeed, the toxin has been previously reported to induce cell cycle arrest and $p21^{Cip1/Waf1}$ expression in human intestinal cells cultured on a 2D plane (ElGhazaly *et al*., 2023). 3D Caco-2 tubes, on the other hand, displayed a decrease in cell cycle progression in a DDR-dependent manner without much change in $p21^{Cip1/Waf1}$ expression, hence the cellular mechanisms behind this are yet to be explored deeply. While genes involved in the sterol or cholesterol biosynthesis pathways could not be examined due to limited time, investigating their influence at the transcriptional or proteomic level using siRNA knockdown, qPCR, immunoblot and immunofluorescence experiments may provide novel insights into pathways elicited in 3D Caco-2 tubes in response to toxin-induced DDRs. Additionally, Caco-2 tubes treated with the typhoid toxin and depleted for INCA1 via siRNA transfection could also be tested for barrier integrity to observe the effects of toxigenic cell cycle arrest on the growth and integrity of 3D Caco-2 tubes.

The toxin also elicited distinct transcriptional profiles in intoxicated 2D and 3D Caco-2 models in terms of innate immune genes such as *IFNs*, *IRFs*, *IFITs* and *ILs* (**Chapter 6**). 2D Caco-2 cells in particular had a higher number of differentially expressed immune-related genes than in intoxicated 3D Caco-2 tubes. While *IL1B* was found to be downregulated in mouse colons infected with typhoid toxin expressing *S*. Typhimurium (Del Bel Belluz, *et al.,* 2016), we found this gene to be significantly upregulated in $toxin^{WT}$-treated 2D Caco-2 cells, with no differential expression in $toxin^{WT}$-treated 3D Caco-2 tubes. While the influence of these innate immune genes at the proteomic level could not be explored due to time constraints, further investigation can provide insights into how the toxin modulates innate immune responses in the two models, and their role in host-pathogen interactions during typhoidal *Salmonella* infections.

7.4. Anti-microbial activity of intoxicated 3D Caco-2 tubes and 2D Caco-2 cells

As described in **chapter 6**, certain anti-microbial genes such as *B2M* and the only detectable defensin *DEFB1* were found to be upregulated in both 3D and 2D Caco-2 transcriptomes in response to the toxin. Other antimicrobials such as *APOL3* and *C3* were upregulated in intoxicated 2D Caco-2 cells, while the antimicrobial *LYZ* was downregulated in 3D Caco-2 tubes in response to the toxin.

B2M and LYZ have been reported as anti-microbial agents (Chiou *et al*., 2021, Naveed *et al*., 2023) and were upregulated in the plasma secretome of human challenge volunteers in a toxin-dependent manner (Srour *et al*., unpublished). Furthermore, the complement C3 was upregulated by the typhoid toxin in mammalian cells (ElGhazaly *et al*., 2023). Despite downregulation of *LYZ* in toxin^{WT}-treated Caco-2 tubes, immunofluorescence data indicated towards an increase in LYZ expression in toxin^{WT}-treated Caco-2 tubes in comparison to untreated or toxin^{HQ}-treated controls. Additionally, LYZ was also expressed in 2D Caco-2 cells in a DDR-independent manner with minimal differences between treatments. While *LYZ* was the only anti-microbial gene we could examine from the RNAseq data via immunofluorescence, further exploration of anti-microbials through ELISAs and immunoblotting will offer a clearer picture regarding their role in toxin-induced responses in the gut.

Overall, the typhoid toxin was observed to reduce intracellular NTS *Salmonella* burden in both 2D Caco-2 cells and 3D Caco-2 tubes at 24 hours post infection. For statistical relevance, additional biological replicates will have to be obtained to strengthen findings. Future experiments with typhoidal *Salmonellae* may prove more insightful in understanding how the toxin influences their invasion in 2D and 3D human intestinal models, as TS strains are known to be more invasive than NTS strains (Dougan and Baker, 2014, Gal-Mor, 2019).

Part IV: Materials and methods

8. Cell biology

8.1. Calculating cell density for seeding

Cell densities were calculated using the TC20 automated counter (Biorad, 1450102) or a haemocytometer (Hawksley, AC1000). The cell suspension was first diluted 1:2 with Trypan Blue (Sigma-Aldrich, T8154). For automated counting, a counting slide with 10 µl of the diluted sample was inserted into the machine for readout. For manual counting, 10 µl of the sample was placed on the haemocytometer grid (**Fig. 8.0**) and fixed with a glass coverslip before placing it under a light microscope.

Cells that weren't stained blue were counted in each corner of the grid (**Fig. 8.0**). The numbers were then summed up together and divided by 2 to obtain the live cell count per ml:

$$\frac{\text{number of live cells in corner } 1 + 2 + 3 + 4}{2} \times 4 \text{ cells/ml}$$

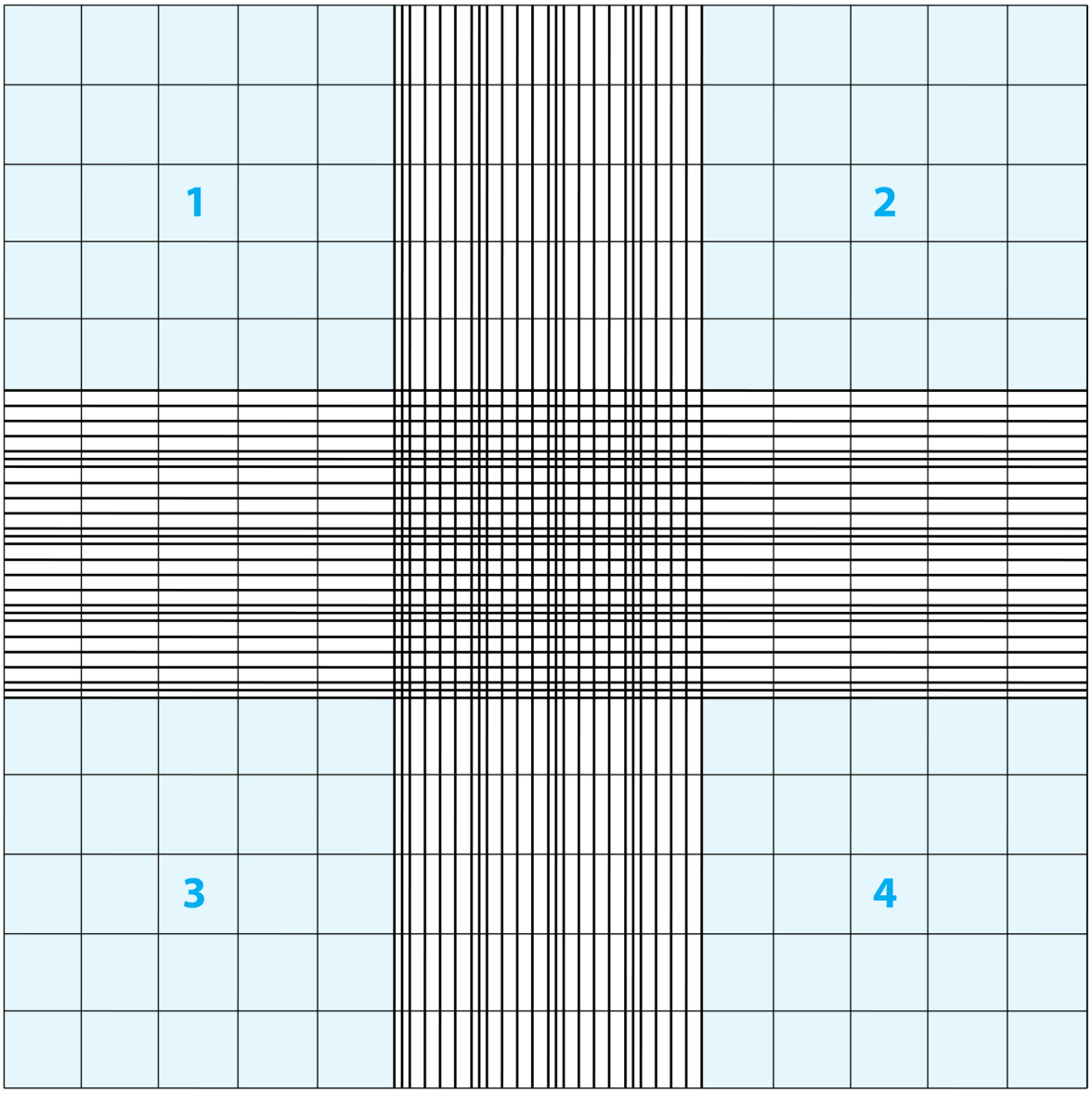

Figure 8.0 Haemocytometer grid. Live cells in corners 1, 2, 3 and 4 of the grid were counted manually for calculating cell density.

8.2. Mammalian cell culture

8.2.1. Cryopreservation and revival

Caco-2 (Sigma-Aldrich, 86010202) and DLD-1 cells (ECACC, 90102540) were cryopreserved at -80°C using sterile technique. For Caco-2 and DLD-1 cultures, at least 2 million cells were pelleted at 125 RCF for 10 minutes and resuspended in 900 µl of FBS in 1.5 ml microcentrifuge tubes (Agilent, 5188-5251) before transferring the

entire volume to a cryovial (Nalgene, 5000-1020) containing 100 µl of DMSO (Sigma-Aldrich, D2438). The cryovials were then immediately placed in Mr Frosty (Thermo Scientific, 5100-0001) and transferred to a -80°C freezer.

DLD-1 and Caco-2 cryovials stored at -80°C were thawed for culture within 3 months using sterile technique. To begin with, T25 flasks (Greiner, 690175) were filled with 4 ml of supplemented culture medium pre-warmed to 37°C and specific to the cell line being revived (**Table 8.0**). The required cryovial was then removed from the -80 freezer and placed in a bead bath set at 40-42°C for not more than 2 minutes, or a water bath at 37°C for not more than 90 seconds before transferring the contents of the vial to the T25 flask. Cells were then allowed to recover and attach overnight in a humidified incubator (Panasonic) at 37°C and 5% CO_2. The next day, culture medium in the T25 was replaced with 5 ml of fresh pre-warmed supplemented medium. Upon reaching 70-80% confluency in about 2-3 days, medium was aspirated from the T25 and cells washed once with 5ml of PBS (Sigma-Aldrich, D8537). Next, cells were treated with 1 to 2 ml pre-warmed trypsin (Sigma-Aldrich, T4049) for 8-10 minutes at 37°C to promote detachment. Trypsin was then neutralized with equal volume of pre-warmed culture medium (**Table 8.0**) and the cell suspension then transferred to a T75 flask (Greiner, 658175) to a final volume of 10 ml of pre-warmed culture medium (**Table 8.0**).

8.2.2. Maintenance

Caco-2 and DLD-1 cells were maintained in T75 flasks and passaged after reaching 70-80% confluency.

Cell line	Culture medium
Caco-2	MEM-α with Glutamax (Gibco, 32561037) supplemented with 10% FBS, 10 U/ml Penicillin/Streptomycin (Gibco, 11548876) and 50 µg/ml Kanamycin sulphate (BioBasic, KB0286)
DLD-1	RPMI with L-glutamine (R8758) supplemented with 10% FBS, 10 U/ml Penicillin/Streptomycin and 50 µg/ml Kanamycin sulphate

Table 8.0 Cell lines and their respective growth media.

Essentially, medium was first aspirated from the T75 flask and cells washed once with 10ml of PBS. Next, cells were treated with 2.5 to 3 ml pre-warmed trypsin for 8-10 minutes at 37°C to promote detachment. Trypsin was then neutralized with equal volume of pre-warmed culture medium (**Table 8.0**) and the cell suspension then moved to a 15 ml falcon (Corning, 352096) for centrifugation at 250 RCF for 5 minutes. The supernatant was then discarded and cells resuspended in 5 ml of fresh pre-warmed medium, after which they were seeded into fresh T75 flasks at a 1:5 or 1:10 dilution to a final volume of 10 ml of pre-warmed culture medium. If low-density flasks did not reach 70% confluency by three days, medium was changed to fresh pre-warmed medium anyway.

DLD-1 and Caco-2 cells were maintained in culture until passage 40.

For suspension THP-1 cells, cells were passaged once they reached a density of 0.8 million per ml, typically every 2-3 days. To do this, cells were pelleted at 1000 RPM for 5 minutes and resuspended in a fresh T75 at a density of 0.2 million cells per ml. The culture medium used to resuspend cells comprised 25% of the old supernatant and 75% of fresh medium (**Table 8.0**) supplemented with 50 µM BME (Sigma-Aldrich, M6250).

All supplemented culture media were stored at 4°C and used within 2 months.

8.2.3. Coating plates for 2D culture

Plate format	Coating volume per well
6 well	800 to 1000 µl
24 well	250 µl
96 well	50 µl

Table 8.1 Pipetting volumes for Collagen I coating according to plate format.

For seeding Caco-2 or DLD-1 cells in a 6 well (Greiner, 657160), 24 well (Greiner, 662160) or 96 well tissue culture plate (Greiner, 655098), plates were first coated with rat tail collagen I solution (Bio-Techne, 3447-020-01) diluted to 0.6 mg/ml using 30% sterile ethanol. After pipetting the coating solution into wells (**Table 8.1**), the plates were incubated at 37°C for at least 2 hours to allow sufficient polymerization. Coated wells were then washed once with PBS according to volume scheme in **table 8.2** before seeding cells.

Plate format	Wash volume or medium volume per well
6 well	1500 µl
24 well	500 µl
96 well	100 µl

Table 8.2 Pipetting volumes for wash and culture medium according to plate format.

If not seeding cells immediately, coated plates were stored at 4°C or 37°C for up to three weeks.

8.2.4. 3D culture of Caco-2/DLD-1 gut-on-chip model

Before seeding Caco-2 or DLD-1 cells in a 3-lane OrganoPlate® (Mimetas, 4004-400-B) to generate tubular models, the middle channel of each chip was first seeded with the ECM mixture and allowed to polymerize for at least 24 hours.

8.2.4.1. Seeding the ECM

Before starting with ECM preparation, columns including the observation window (**Fig. 8.1**) were filled with 50 µl of PBS using a multichannel pipette. For example, if chip B02 was planned to be used, then A02, B02 and C02 were filled with PBS.

The components used to prepare the ECM were Collagen I (Bio-Techne, 3447-020-01), 1M HEPES solution and 37g/L $NaHCO_3$ solution. HEPES was either purchased from a manufacturer (Gibco, 15630080) or prepared manually by dissolving stock powder (Sigma-Aldrich, H3375-25G) in sterile MilliQ water and adjusting pH to 7.2-7.5 using HCl/NaOH. To prepare 37g/L $NaHCO_3$ solution, stock powder (Sigma-Aldrich, S5761-500G) was dissolved in sterile MilliQ water and pH adjusted to 9.5 using NaOH.

After preparation, both 1M HEPES and 37g/L $NaHCO_3$ solution were stored at -20°C as 30 µl single-use aliquots and used within 2-3 months.

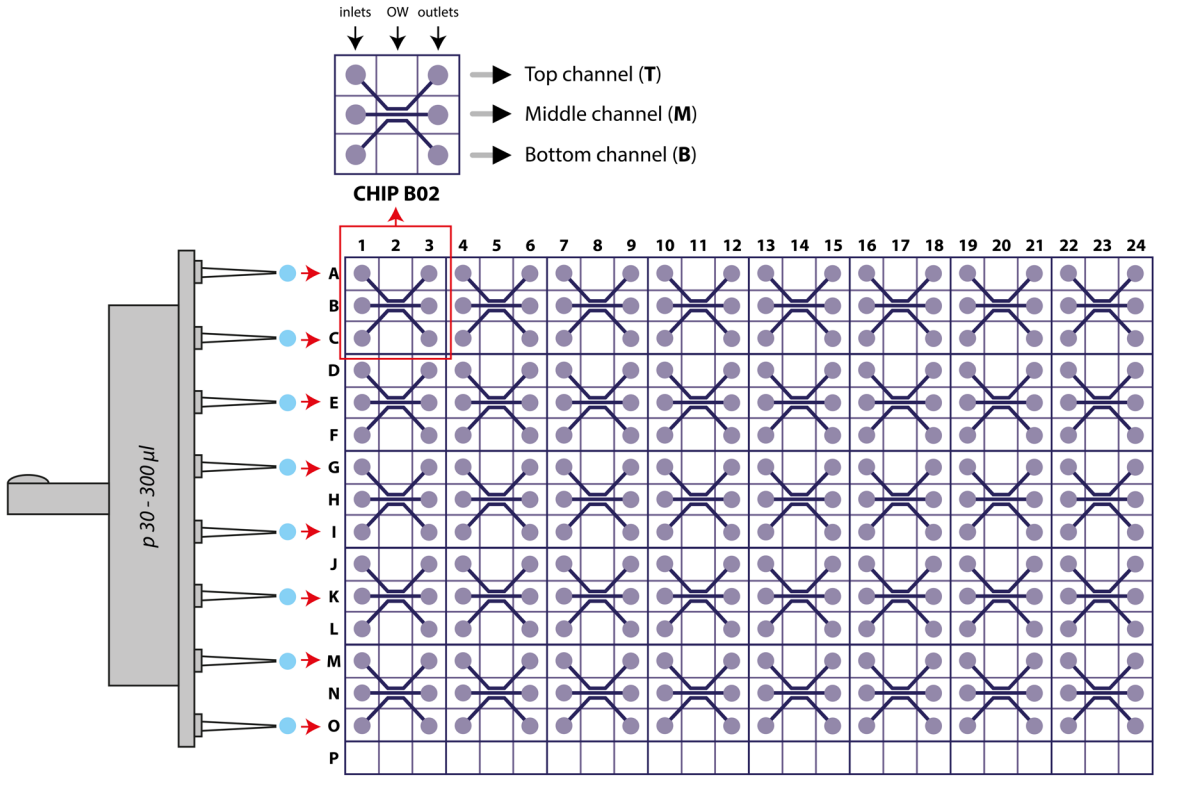

Figure 8.1 Schematic of the OrganoPlate® 3-lane 40. Blue dots indicate how an eight-channel multipipette orients horizontally with column 1, 2 and so on. OW= Observation window which is

denoted by B02, E02, etc where the 3D intestinal tube is visualised and imaged under a microscope.

ECM components were thawed on ice a few minutes before ECM seeding. A 1.5ml Eppendorf tube was also placed on ice to cool it and avoid ECM solidification/polymerisation while mixing the components. All components were mixed on ice in a 1:1:8 ratio in the pre-cooled Eppendorf, starting with 10 µl of 1 M HEPES first, followed by 10 µl of 37g/L $NaHCO_3$ and then 80 µl of 5 mg/ml Collagen I. As the final component, i.e. Collagen I was added and mixed with other components, care was taken to not create any air bubbles. The ECM was mixed at least 50 times on ice to ensure complete homogeneity and used within 10 minutes.

If too many air bubbles were present, the mixture was centrifuged at a high speed for about 5 seconds to get rid of them and quickly placed back on ice.

The volume seeded was 2.4 µl in each chip at the **inlet** of the middle channel (**Fig. 8.1**) using 20 µl filter tips (S1123-1710). Before dispensing, the tip of the pipette tip was aligned within the hole in the inlet at a 90° angle until they were gently in contact. To see the hole in the inlet first, the plate was tilted slightly towards the face, and then the ECM was dispensed into it. This made dispensing easier.

If for some reason the capillary action was faulty and the ECM did not get sucked into the middle channel through the inlet, the 2.4 µl volume was aspirated from the inlet and immediately dispensed into the outlet of the same channel to re-attempt ECM seeding. This method almost always worked successfully.

The OrganoPlate® was seeded with ice-cold ECM in the required chips within 5 minutes and placed quickly in the 37°C incubator to start solidification/polymerization and avoid the ECM mixture leaking into neighbouring channels. After 15 minutes, 30 µl of PBS was added to the inlets of all the ECM channels to prevent ECM dehydration and the plate was put back in the incubator for a day. If seeding cells after the weekend, 50 µl of PBS was added to the ECM inlets instead.

If ECM seeding took longer than 5 minutes, the chips were seeded in small batches, e.g one row at a time or one column at a time, and fresh ECM was prepared and seeded once the first batch was polymerized after 15 minutes.

8.2.4.2. Seeding cells

DLD-1 and Caco-2 cells were seeded the next day or after the weekend at a density of 20,000 cells per chip. To do this, cells were trypsinized as described in Section 1.2.2 and resuspended in 100 µl of appropriate medium (**Table 8.0**) at a density of 10,000 cells/µl and stored on ice if not used immediately. Although enough to seed one whole plate, this volume was prepared even for a small number of chips to create an adequate supply in case cell seeding went wrong in some of the chips.

Next, PBS was gently aspirated from all ECM inlets in the OrganoPlate®. The cell suspension was pipetted vigorously to ensure homogeneity, and then 2 µl of the suspension dispensed into the top channel **inlet** (**Fig. 8.1**) using 20 µl filter tips. Cells were resuspended regularly before seeding every 3 or 5 chips to ensure homogenous cell density between chips and reduce differences in tube development.

Next, 50 µl of medium was dispensed gently into the top channel **outlet** to create a passive pump and ensure all cells entered the top channel. If cells did not enter, the plate was gently tapped on the bench, against an object or tapped again sideways to dislodge cells attached at the inlet and promote entry. If there was still no success, the inlet was gently aspirated first, and then the outlet using an automated aspirator. Care was taken to not let the aspirator sit in the inlets/outlets too long to avoid ECM getting sucked out as well.

After aspiration, cells were reseeded the same way as described above. Cells almost always entered the top channel successfully the second time. If not, cells were aspirated again as described above, and the cells were seeded through the outlet instead of the inlet the third time.

After this, the plate was placed in the CO_2 incubator at a 75° incline for between 2-6 hours using the Mimetas plate stand (supplied with the OrganoPlates®) to allow cell attachment onto the ECM.

After attachment, 50 µl medium was dispensed gently into the remaining empty outlets/inlets in the top channel and bottom channel (**Fig. 8.2**), after which the plate was placed on a rocker (Mimetas, MI-OFPR-L) set at a 7° angle and 8-minute interval to start perfusion.

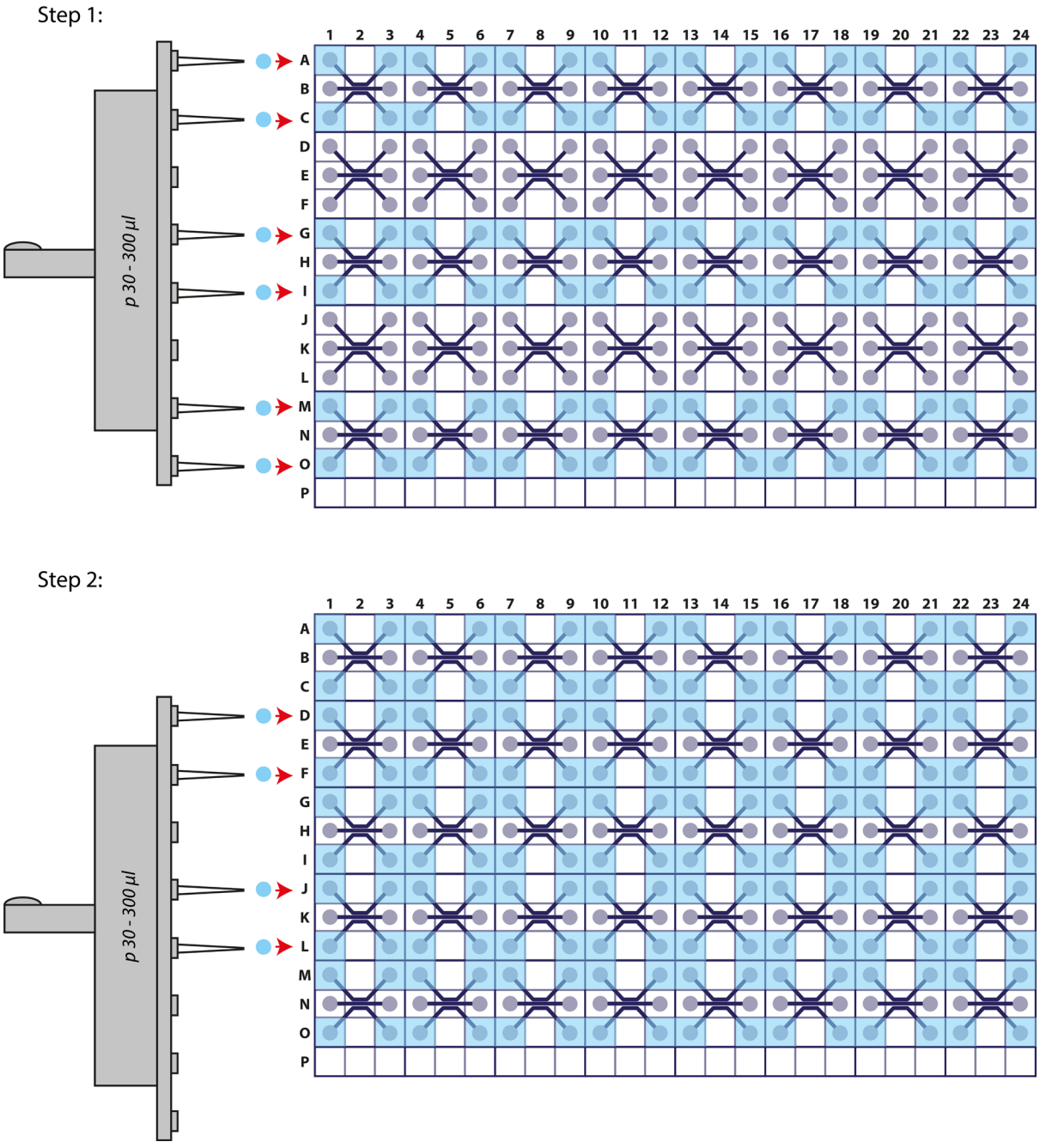

Figure 8.2 Dispensing medium into the OrganoPlate® 3-lane 40. Blue dots indicate how an eight-channel multipipette orients horizontally with each row/column of chips. After step 1, the two pipette tips at the bottom are discarded before dispensing medium into the remaining two rows of chips.

Medium was replaced gently with fresh medium every 2-3 days. Barrier integrity was tested at day 3 post cell seeding.

8.3. Colon organoid culture

Organoids were generated in the Boccellato Lab from human tissue material obtained at the Translational Gastroenterology Unit at John Radcliffe Hospital, University of Oxford, under the Research Ethics Committee number 21/YH/0206.

8.3.1. Maintenance

Organoids were maintained in a 50 µl drop of Cultrex extracellular matrix hydrogel (bio-techne, 3536-005-02) per well in a 24 well plate or four 50 µl drops per well in a 6 well format submerged in culture medium. These were cultured until passage 20 or cryopreserved where required using sterile technique.

For routine maintenance, organoids were passaged using the gentle dissociation method every 7 days. For seeding experiments, organoids were passaged using the shearing method.

Culture medium was freshly prepared in limited amounts using components in **table 8.3**, sterilised using 0.2 µm filters (Sarstedt, 83.1826.001), stored at 4°C and used within two weeks.

Ingredient	µl/ 20ml	Stock storage (°C)	Stock concentration	Final concentration	Dissolved in	Product code
Wnt surrogate-fc	20	-80	100 µg/ml	100 ng/ml	Tris-NaCl	IPA, N001 - 100 µg
Rspo1	5000	-80	100% (conditioned medium)	25%	-	Prepared in house by Boc Lab
DMEM/F12	13260	4	-	-	-	Gibco, 12634010

B27	400	-20	50X	1X	-	Gibco, 17504044
N2	200	-20	100X	1X	-	Gibco, 17502048
EGF	10	-20	100 µg/ml	50 ng/ml	0.1% PBS-BSA	Gibco, PHG0311
Noggin	20	-20	100 µg/ml	100 ng/ml	0.1% PBS-BSA	Peprotech, 120-10C
FGF-10	2	-20	100 µg/ml	10 ng/ml	0.1% PBS-BSA	Peprotech, 100-26
Nicotinamide	200	4	1 M	10 mM		Sigma-Aldrich, 72340-100g
NAC	50	-20	500 mM	1.25 mM		Sigma merck, A9165-5G
HEPES	200	4	1 M	10 mM	-	Gibco, 15630056
SB 202190 (p38i)	20	-20	10 mM	10 µM		Merck, S7067
ROCKi	66	-20	3 mM	10 µM		Selleckchem, S1049
PGE2	2	-20	10 mM	1 µM		Bio-Techne, 2296
Primocin	40	-20	50 mg/ml	100 µg/ml	-	Invivogen, ant-pm-05
BSA	250	-20	10%	0.125%	PBS	Sigma-Aldrich, A7030

SB431542	20	-20	10 mM	10 µM	DMSO	Bio-Techne, 1614/1
FGF basic	2	-20	100 µg/ml	10 ng/ml	0.1% PBS-BSA	Peprotech, 100-18B
IGF-1	2	-20	1 mg/ml	100 ng/ml	0.1% PBS-BSA	Peprotech, 100-11
GlutaMAX	200	4	100X	1X	-	Gibco, 35050038

Table 8.3 Colon medium components.

8.3.1.1. Gentle dissociation method

Before starting the gentle dissociation protocol, Cultrex gel from -80°C was thawed for at least two hours (or overnight) on ice in the fridge, medium warmed to 37°C and the centrifuge set to 4°C. Subsequently, medium was aspirated and the drops washed once with ice-cold PBS without damaging them according to the volume scheme in **table 8.4**.

Plate format	Volume per well
6 well (4 drops per well)	2000 µl
24 well (1 drop per well)	500 µl

Table 8.4 Volumes for organoid drops according to plate format.

8.3.1.1.1. Retrieving organoids from Cultrex drops

Next, Gentle Dissociation Solution (Stemcell technologies, 100-0485) was added to all wells without touching the drops using volume scheme in **table 8.4**. After this, a p1000 tip (Starlab, S1122-1830) was pre-wetted with sterile 1% PBS-BSA or DMEM+10%FCS to prevent organoids from sticking to the plastic, and then used to break the gel drops in each well by aspirating and flushing dissociation solution directly over the drops a couple of times.

The crumbled drops were then incubated with the dissociation solution for 10 minutes at room temperature.

After 10 minutes, an autoclaved unfiltered p10 tip (Starlab, S1111-3700) was inserted into a filtered p1000 tip, and the double tip pre-wetted with sterile 1% PBS-BSA (or DMEM+10%FCS). The double tip was then used to gently aspirate and dispense the crumbled drops about 10 times to dissociate them further.

After this, no more than three drops (200 µl of Cultrex) were pooled at a time into a 2 ml Eppendorf (Fisher Scientific, 10038760) on ice, or 12 drops (600 µl of Cultrex) in a 15 ml falcon tube on ice. The drops were then centrifuged at 1200g for 3 minutes at 4°C. The Eppendorf/falcon was then placed back on ice and supernatant discarded as much as possible without disturbing the cell pellet.

8.3.1.1.2. Seeding new drops

If the organoid pellet was from one 50 µl drop, the pellet was now dissolved in 110 µl of Cultrex (extra 10 µl to account for dead volume) carefully without creating air bubbles. After mixing evenly, one 50 µl drop was seeded per well in a fresh 24-well plate, or 4 drops per well in a fresh 6-well plate.

The plates were then incubated at 37°C for 20 minutes to allow the drops to solidify. After this, colon medium (**Table 8.3**) was added to each well containing the drops, and sterile water to the outer wells of the plate (to prevent cultures from drying out) according to volume scheme in **table 8.4**. The plates were then placed back in the CO_2 incubator to continue culture. The drops were replaced with fresh warm medium after 3-4 days using the same volume scheme (**Table 8.4**), and the organoids passaged again at day 7 post seeding.

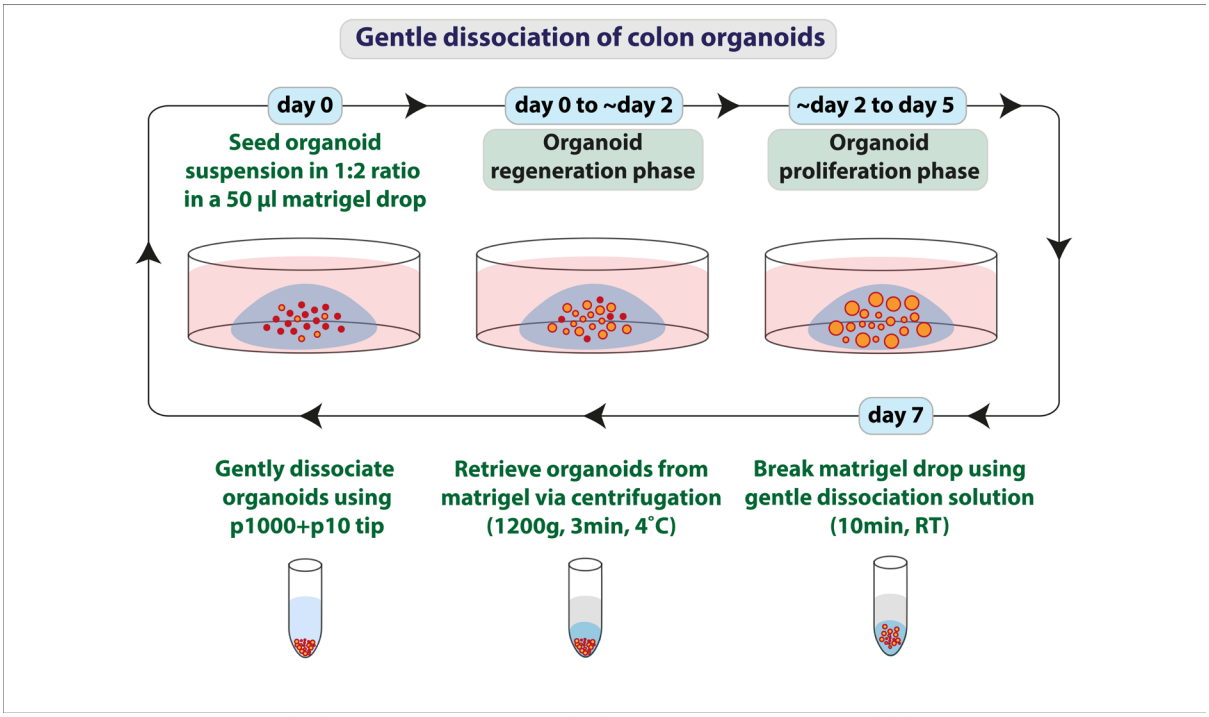

Figure 8.3. Schematic of organoid culture via gentle dissociation. Cultrex or Matrigel drops (Corning, 356231) freshly passaged via this method consist of a heterogenous mixture of small organoids and single cells from sheared organoids that survived the stress associated with dissociation. During the regeneration phase, single cells start growing and aligning to form new small organoids, and during proliferation, these organoids grow larger until they are ready to be passaged again. If not passaged on time, the overgrown organoids collapse on themselves and disintegrate to death.

For seeding primary cells from organoids for 2D or 3D culture, Cultrex drops were passaged at day 7 using the shearing method instead of gentle dissociation.

8.3.1.2. Shearing method

Before starting with the shearing process, Cultrex gel from -80°C was thawed for at least two hours (or overnight) on ice in the fridge, cell recovery solution (Corning, 354253) placed on ice after removing from fridge, colon medium warmed to 37°C (**table 8.3**) and centrifuge set to 4°C.

8.3.1.2.1. Retrieving organoids from Cultrex drops

Ice-cold recovery solution was added according to volume scheme in **table 8.5** and incubated with the drops for 30 minutes at 4°C.

Plate format	Volume per well
6 well (4 drops per well)	800 µl
24 well (1 drop per well)	200 µl

Table 8.5 Volumes for organoid drops according to plate format.

While drops were being incubated with the recovery solution, the following solutions were prepared, filter-sterilized and warmed to 37°C–

i. DMEM with 10% FCS containing 200 U/ml **DNase I solution** and 10 µM **ROCKi** – 125 µl per drop
ii. TrypLE (Life Technologies, 12604013) containing 10 µM **ROCKi** – 125 µl per drop

After 30 minutes, a p1000 tip was pre-wetted with sterile 1% PBS-BSA (or DMEM+10%FCS) to prevent organoids sticking to plastic, then used to break the Cultrex drops by aspirating recovery solution and flushing it on the drop, several times.

Next, no more than 4 drops (200 µl of Cultrex) at a time were pooled in a 1.5 ml Eppendorf on ice, or 12 drops (600 µl of Cultrex) in a 15ml falcon tube on ice. The drops were then centrifuged at 2000g for 3 minutes at 4°C. Supernatant and Cultrex were discarded as much as possible without disturbing the organoid pellet and while keeping the Eppendorf/falcon on ice.

To prevent problems related to cell clumping and obtain a good quality single cell suspension, any residual Cultrex was removed by resuspended the drops again in cold DMEM+10%FCS using pre-wetted p1000 tip (medium wash), centrifuging as described in the previous step and discarding supernatant while keeping the Eppendorf/falcon on ice. This medium wash was performed once or twice, as needed.

8.3.1.2.2. Dissociating organoids to primary cells

The organoid pellet was then resuspended in TrypLE containing ROCKi in a 15 ml falcon and incubated for no more than 5-6 minutes at 37°C in a water bath, while gently flicking the tube with a finger or gently vortexing for 15 seconds after every minute to resuspend the organoids.

After 5 minutes, the falcon was placed under the microscope to observe if the organoids had dissociated. If not, they were incubated for another minute.

To prevent cells from clumping, TrypLE was inactivated after 6 minutes with an equal volume of DMEM+10%FCS containing DNase I + ROCKi prepared earlier. The cells were then pipetted about 10 times through a pre-wetted double tip (p10+p1000) to dissociate them further (mechanical dissociation).

8.3.1.2.3. Seeding new drops

To seed new drops, 50,000 – 100,000 cells were centrifuged at 700g for 3 minutes and resuspended in 55 µl of Cultrex (extra 5 µl to account for dead volume) carefully without creating air bubbles.

One 50 µl drop was seeded per well in a fresh 24-well plate, or 4 drops per well in a fresh 6-well plate.

The plates were then incubated at 37°C for 20 minutes to allow the drops to solidify. After this, colon medium (**table 8.3**) was added to each well containing the drops, and sterile water to the outer wells of the plate (to prevent cultures from drying out) according to volume scheme in **table 8.3**. The plates were then placed back in the CO_2 incubator to continue culture. The drops were replaced with fresh warm medium after 3-4 days using the same volume scheme (**table 8.3**), and the organoids passaged again at day 10 post seeding.

8.3.2. Coating plates for primary 2D culture

Chamber slides (Ibidi, 81201) or 24-well plates were used to seed primary cells sheared from organoids.

Before shearing, plates were coated with either collagen I as described in **section 8.2.3**, or Atelocollagen (KOKEN®, KKN-IPC-50). Atelocollagen was prepared by diluting the 5mg/ml stock to 1 mg/ml using 0.02 M sterile acetic acid. Coating volumes are described in **table 8.6**.

The plate was then incubated for 30 minutes at 37°C before washing once with PBS.

Plate format	Volume per well
Ibidi chamber slide	300 µl
24 well	500 µl

Table 8.6 Dispensing volumes according to plate format.

Primary cells obtained through the shearing method in **section 8.3.1.2** were seeded according to the assay being performed. If not seeding cells immediately, plates were filled PBS and stored at 37°C overnight.

8.3.3. 3D culture of primary gut-on-chip model

8.3.3.1. Seeding ECM

The ECM channel of the 3-lane OrganoPlate® was seeded with the ECM as described in section 1.2.4.1. This was performed at least 24 hours before seeding primary cells.

8.3.3.2. Coating top channel

The top channel of the 3-lane OrganoPlate® was coated with Cultrex immediately after ECM polymerization and 24 hours before seeding primary cells. The coating ensured a friendly surface for primary colon cells to adhere to and grow on.

To coat the channel, 40 µl of Cultrex diluted 1:100 in cold PBS was added to the inlet of the top channel (**Fig. 8.1**), after which the plate was incubated at 37°C for 20 minutes to allow the gel to solidify.

8.3.3.3. Seeding cells

Any residual liquid in the top channel and ECM channel was aspirated very gently from outlets and inlets (**Fig. 8.1**) using an automated aspirator.

Primary cells were sheared from organoids as described in **section 8.3.1.2**. A cell suspension of 50,000 cells per µl was prepared, and the cell suspension pipetted vigorously to ensure homogeneity. Using 20 µl filter tips, 2 µl was seeded into the top channel **inlet** of each chip. Cells were resuspended regularly before seeding every 3 or 5 chips to ensure homogenous cell density between chips and reduce differences in tube development.

Next, 50 µl of attachment medium (colon medium **without SB431542**) was dispensed gently into the top channel **outlet** of each chip to create a passive pump and ensure all cells entered the top channel. If cells did not enter, the plate was gently tapped on the bench, against an object or tapped again sideways to dislodge cells attached at the inlet and promote entry. If there was still no success, the inlet was gently aspirated first, and then the outlet using an automated aspirator. Care was taken to not let the aspirator sit in the inlets/outlets too long to avoid ECM getting sucked out as well.

After aspiration, cells were reseeded the same way as described above. Cells almost always entered the top channel successfully the second time. If not, cells were aspirated again as described above, and the cells were seeded through the outlet instead of the inlet the third time.

After this, the plate was placed in the CO_2 incubator at a 75° incline using the Mimetas plate stand (supplied with the OrganoPlates®) to allow cell attachment onto the ECM.

After 3-4 hours, 50 µl attachment medium was dispensed gently into the remaining empty outlets/inlets in the top channel and bottom channel (**Fig. 8.2**), after which the plate was placed back in the incubator for another 24 hours **without rocking**.

After 24 hours of static culture, the plate was placed on the OrganoPlate® rocker set at a 7° angle and 8-minute interval to start perfusion.

At day 2, 48 hours post cell seeding, attachment medium was replaced with colon medium to prevent epithelial to mesenchymal transition (Beaurivage *et al.*, 2020).

After day 2, medium refreshment was carried out every 24-48 hours.

Care was taken to ensure the pipetting force was not too high in each step to prevent cell detachment.

8.4. Barrier integrity assay

For Caco-2/DLD-1 gut-on-chip models, barrier function was tested at day 3. For primary gut-on-chip, barrier integrity was tested at day 8.

To do this, medium was aspirated from all inlets and outlets (**Fig. 8.1**) and replaced with 50 µl of medium containing 0.5mg/ml FITC-dextran 150 kDa (Sigma-Aldrich, 46946) in each inlet/outlet. Alternatively, 2 µl of 25mg/ml stock FITC-dextran was added to each top channel inlet directly so that the final concentration of the dye would be 0.5mg/ml.

The plate was then placed back on the rocker for 30 minutes before imaging the localisation of the dye under a light microscope.

8.5. Intoxication assay

8.5.1. 2D culture model

All intoxication experiments in static cell cultures were performed a day after seeding cells using recombinant typhoid toxin stocks purified by the Humphreys lab. Stocks were diluted to 20 ng/ml using culture medium appropriate for the cell line and then dispensed onto cells in each well according to volume scheme in **table 8.2**. After two hours, wells were washed with PBS according to the same volume scheme and replaced with fresh culture medium. Cells were then chased for 48 hours unless mentioned otherwise in text.

8.5.2. 3D gut-on-chip model

Unless stated otherwise, 3D gut-on-chip models were intoxicated as soon as they attained barrier function with 20 ng/ml of typhoid toxin diluted in culture medium. After 2 hours, chips were replaced with fresh medium without PBS wash. The models were then chased for 48 hours.

8.5.3. 3D colon organoid model

Gently dissociated organoids were treated with the typhoid toxin at day 6 post seeding, while sheared organoids were intoxicated the same day they were seeded. The toxin was diluted in colon medium to the required concentration and dispensed onto organoid drops in each well according to volume scheme in **table 8.4**. Organoids were then incubated with the toxin until the end of the stated timepoint.

8.6. Drug and inhibitor treatment

Drugs were diluted in culture medium to the concentrations mentioned in **table 8.7** and incubated for 48 hours in all models unless stated otherwise.

Inhibitors were diluted in culture medium to the concentrations mentioned in **table 8.7** (unless stated otherwise), added to intoxicated 2D Caco-2 cells after the 2-hour toxin pulse, and incubated for 48 hours.

Drug	Final concentration	Product code
APH	20 µM	Sigma-Aldrich, A0781
ETP	10 µM	Cayman Chemicals, 12092
Inhibitor	**Final concentration**	**Product code**
iATM (KU55933)	1 µM	AOBIOUS, INC, AOB2108
iATR (AZD6738)	1 µM	Merck, ATE959438183-50MG
siRNA	**Final concentration**	**Product code**
siNT	20 nM	Horizon Discovery, D-001810-01-20
siP21	20 nM	Horizon Discovery, L-003471-00-0005

Table 8.7 Inhibitors, drugs and siRNA used in the project. siRNAs are ON-TARGETplus SMARTpool.

8.7. siRNA transfection

Transfections in intoxicated 2D Caco-2s were performed using Lipofectamine RNAiMax (Invitrogen, 13778-150). Briefly, cells were intoxicated as described in **section 8.5.1** for two hours. Towards the end of this two-hour pulse, siRNA (**Table 8.7**) and Lipofectamine solutions were prepared separately by diluting reagents in OptiMEM Reduced Serum medium as described in **table 8.8**.

Reagent	Stock volume (µl)	Diluent volume (µl)
siRNA (20 µM stock)	1.5	75
Lipofectamine RNAiMAX	1.5	75

Table 8.8 siRNA and Lipofectamine preparation for a single well in a 6 well plate.

Next, the diluted Lipofectamine was allowed to incubate at room temperature for 10 minutes, and then mixed with the diluted siRNA solution in **table 8.8** to obtain a final transfection volume of 150 µl for each well in a 6 well plate. Once intoxicated wells were washed with PBS and replaced with fresh medium according to volume

scheme in **table 8.2**, the 150 µl transfection solution was dispensed into the required well and gently mixed with the medium using a pipette. Cells were then incubated with the transfection solution for 48 hours.

9. Microbiology

9.1. Preparation of LB agar plates

To prepare culture plates for growing bacteria, 35 g/L LB agar (Sigma-Aldich, L2897) was prepared in distilled water, boiled until completely dissolved and autoclaved. The liquid LB agar was then poured into sterile petri dishes (Thermo Scientific,11309283) using sterile technique and allowed to solidify at room temperature. If culturing antibiotic-resistant bacteria, the liquid LB agar was first supplemented with appropriate antibiotics as described in **table 9.0**.

Bacterial strain	Antibiotic resistance	Concentration of antibiotic needed in LB agar
***S*. Javiana WT pM975**	Ampicillin	100 µg/ml
***S*. Javiana ΔCdtB pM975**		

Table 9.0 Bacterial strains used in the project and their antibiotic resistance.

9.2. Cryopreservation and revival

For long-term storage, 750 µl of log-phase bacteria in LB broth (Millipore, 28713) containing appropriate antibiotics (**Table 9.0**) was mixed with 250 µl of autoclaved 100% glycerol in a cryovial, and the vial vortexed to ensure an even mix with the glycerol. After this, the cryovials were flash-frozen in liquid nitrogen and stored at -80°C.

For reviving bacteria on LB agar plates, glycerol stocks were recovered from -80°C and placed on dry ice. Using sterile technique, a p10 or p200 pipette tip was used to scrape some of the frozen bacteria, or alternatively, a flamed 10 µl inoculation loop was used for the same (Avantor, 612-9354). The tip or inoculation loop was then used to streak across the four quadrants of a sterile LB agar plate in a zig-zag manner. The streaked plates were then placed upside down in a non-CO_2 incubator and left to grow overnight at 37°C. The next day, the plates were recovered from the incubator and stored at 4°C for no more than 3 weeks.

9.3. Preparing overnight liquid culture

A day before performing *Salmonella* invasion, liquid bacterial cultures were prepared in sterile LB broth containing appropriate antibiotics (**Table 9.0**) by selecting a colony from the streaked LB agar plate using a pipette tip and placing the tip in a falcon tube containing 5 ml of LB broth. The falcon was then placed in a shaking incubator set to 37°C and 250 RPM to grow overnight.

9.4. Preparing day culture

The next day, the overnight culture was diluted 1:100 in a falcon tube containing 5ml of fresh LB broth with appropriate antibiotics. This new falcon or day culture was grown in the shaking incubator for two hours until bacteria entered their logarithmic growth phase, i.e between OD_{600} of 1 and 1.4. The remaining overnight culture was stored at 4°C for not more than a week for future use.

Once the day culture reached the required OD_{600} range, bacteria were normalized to OD_{600} 1 using the formula below –

$$\text{Volume of day culture needed to normalize to } OD_{600} \text{ 1 (ml)} = \frac{1}{OD_{600} \text{ of the day culture}}$$

This volume was centrifuged at 13,000 RPM for 5 minutes and the bacterial pellet carefully resuspended in 1 ml of sterile PBS.

9.5. Calculating invasion volume

As the estimated number of bacteria present in a bacterial suspension of OD_{600} 1 is 8×10^8 per ml (Agilent), the volume of bacteria needed from this suspension to invade each well in a tissue-culture plate or each tube in an OrganoPlate® was calculated as follows –

$$\text{Volume of bacteria needed per well or chip (ml)} = \frac{\text{number of bacteria needed per well}}{8 \times 10^8}$$

where number of bacteria needed per well = MOI × mammalian cell number per well

The MOI used was 100 unless specified otherwise in the text.

9.6. *Salmonella* invasion

Cell line	Culture medium
Caco-2	MEM-α with Glutamax supplemented with 10% FBS
DLD-1	RPMI with L-glutamine supplemented with 10% FBS

Table 9.1 Growth media used for 2D and 3D models during invasion.

9.6.1. 2D culture model

Mammalian cells were seeded a day before performing invasion and cultured in appropriate medium (**Table 9.1**) without antibiotics. If using antibiotics, cells were washed with PBS just before starting invasion.

The invasion volume calculated in **section 9.5.** was topped up with fresh culture medium (**Table 9.1**) to the final volume described in **table 8.2** and dispensed into each well.

The plate was then centrifuged at 1000 RCF for a minute to sediment the bacteria onto the cells and promote invasion.

After 2 hours of invasion (or as specified in the text), the invasion medium was aspirated and cells washed twice with PBS. Cells were then either lysed for CFU assay, fixed for immunostaining or maintained in culture for a particular timepoint using fresh culture medium (**Table 9.1**) supplemented with 10 µg/ml Gentamicin (Santa Cruz, SC-203334).

9.6.2. 3D gut-on-chip model

Invasion was performed on the Caco-2 gut-on-chip model as soon as the model attained barrier function. To calculate the invasion volume in **section 9.5**., the number of cells present in the Caco-2 tube was estimated using the following formula –

$$\text{number of cells} = 2^{n} \times 20{,}000$$

$$\text{where n = number of doublings} = \frac{\text{number of hours that have passed since cell seeding}}{\text{doubling time}}$$

The doubling time was estimated to be roughly 32 hours for the culture conditions employed.

The invasion volume was then calculated as described in **section 9.5**. If the volume was not in the range of 30 to 50 µl per chip, this was adjusted either by diluting the invasion volume with more medium (**Table 9.1**) or concentrating via centrifugation at 13000 RPM for a minute to achieve the desired range for successful seeding.

Prior to invasion, culture medium (**table 9.0**) was aspirated from all inlets and outlets (**Fig. 8.1**). The invasion volume was then dispensed into each top channel inlet. After this, the OrganoPlate® was incubated with the bacteria for 2 hours without perfusion, unless specified otherwise in the text.

Subsequently, the invasion medium was aspirated and tubes either lysed for CFU assay, fixed for immunostaining or maintained in culture for a particular timepoint using fresh culture medium (**Table 9.1**) supplemented with 10 µg/ml Gentamicin. PBS washes before gentamicin treatment were kept to a minimum or avoided altogether, owing to the delicate nature of the tubes.

9.7. CFU assay

9.7.1. 2D culture model

Mammalian cells were seeded at a density of 1×10^4 cells per well in a 24 well plate and intoxicated as described in **section 8.5.1.** Toxin chase was performed for 48 hours before starting invasion as described in **section 9.6.1**.

At 2 hours and 24 hours post invasion, cells were washed with PBS, then lysed with 1 ml of 1% sterile Triton X-100 in PBS (Sigma-Aldrich, X100-500ML) for 5 minutes at room temperature. The lysates were then transferred to a 96-well plate and serially diluted ten-fold for up to 7 dilutions using a multi-channel pipette. 5-10 µl of each dilution was plated on LB agar plates with ampicillin (**Table 9.0**) and allowed to incubate overnight at 37°C. Colonies were counted the next day and the dilution factors with countable colonies were chosen to calculate CFUs with the help of the following formula –

$$\text{CFUs per well} = \frac{\text{number of colonies counted in the chosen dilution factor} \times 1\ \text{ml}}{\text{volume plated (ml)} \times \text{dilution factor}}$$

where 1 ml is the volume of Triton X-100 used to lyse each well.

9.7.2. 3D gut-on-chip model

Mammalian cells were seeded at a density of 2×10^4 cells per chip in the 3-lane Organoplate® and intoxicated as described in **section 8.5.2.** Toxin chase was performed for 48 hours before starting invasion as described in **section 9.6.2**.

At 2 hours and 24 hours post invasion, medium was aspirated from all inlets and outlets. Next, 100 µl of 1% sterile Triton X-100 in PBS was dispensed in the top channel inlet (**Fig. 8.1**) and incubated for 10 minutes at room temperature or until the tubes were completely lysed. The lysates were then transferred to a 96-well plate and serially diluted ten-fold for up to 11 dilutions using a multi-channel pipette. 5 µl of each dilution was plated on LB agar plates with ampicillin (**Table 9.0**) and allowed to incubate overnight at 37°C. Colonies were counted the next day and the dilution

factors with countable colonies were chosen to calculate CFUs with the help of the following formula –

$$\text{CFUs per tube} = \frac{\text{number of colonies counted in the chosen dilution factor} \times 0.1 \text{ ml}}{\text{volume plated (ml)} \times \text{dilution factor}}$$

where 0.1 ml is the volume of Triton X-100 used to lyse each tube.

10. Biochemistry

10.1. EdU labelling

Cells were seeded at the densities stated in **table 9.2** and treated as required. Unless stated otherwise in the text, EdU incorporation was performed 24 hours before the end of the timepoint using the Click-iT™ EdU Cell Proliferation Kit for Imaging (Thermo Scientific, C10340). The 10mM EdU stock was first diluted 1:50 in fresh culture medium relevant to the model to prepare a working solution. This working solution was then diluted in the medium present in each well/chip to achieve a final concentration of 10 µM EdU. In the case of 6-well and 24-well plates, these were gently swished around on a flat surface, or the medium gently pipetted several times in each well to mix EdU evenly with the medium before placing them back in the incubator. In the case of the Organoplate®, the plate was simply placed back on the rocker in the incubator.

Medium replacement in wells/chips was avoided to prevent potential effects on cell cycle kinetics.

Format	Culture model	Seeding density
6-well plate	2D Caco-2/DLD-1 cells	1×10^5 cells per well on coverslips
24-well plate	2D Caco-2/DLD-1 cells	1×10^4 cells per well on coverslips
	2D Primary colon cells	2×10^4 cells per well on coverslips
Ibidi chamber slide	2D Primary colon cells	1.5×10^4 cells per well

Table 9.2 Cell seeding densities for fluorescence microscopy.

10.2. Fixation

10.2.1. 2D culture model

At the end of the timepoint, medium was aspirated from all wells and coverslips (Avantor, 631-1578) fixed using 4% PFA (Thermo Scientific, J61899) for 10-15 minutes at room temperature according to volume scheme in **table 8.2**. Wells were then washed twice with PBS, refilled with sufficient PBS and plates stored at 4°C for up to a month if not assayed immediately.

10.2.2. 3D gut-on-chip model

Medium was aspirated from all inlets and outlets at the end of the timepoint and 4% PFA added according to volume scheme in **table 9.3**. After 10 to 15 minutes of incubation at room temperature, chips were washed twice with PBS (5 minutes each) using the same volume scheme and stored at 4°C in PBS for up to four weeks if not staining immediately.

Top channel inlet	Top channel outlet
100 µl	50 µl

Table 9.3 Volume scheme for the Organoplate®.

10.2.3. 3D colon organoid model

Organoids were retrieved from Cultrex drops at the end of the timepoint as described in **section 8.3.1.2.1**. When required, the organoids collected in the Eppendorf were washed an additional two times with 200 µl cold PBS to remove any residual Cultrex, after which they were fixed with 200 µl of 4% PFA for 20 minutes at room temperature. Organoids were then washed with PBS twice, immersed in 200 µl PBS again and stored at 4°C for up to a month if not assayed immediately.

For every wash, organoids were never centrifuged, but instead allowed to sediment to the bottom of the Eppendorf tube before gently aspirating the supernatant. This allowed the organoids to retain their spherical shape.

10.3. EdU staining

Fixed cells, gut-on-chip models or organoids were permeabilized and probed for EdU using the Click-iT™ EdU kit according to manufacturer's instructions but with slight changes.

In the case of 2D cultures, the volume scheme described in **table 8.2** was used for permeabilization and washes, and the final volume of the reaction cocktail was reduced to 50 µl per coverslip and incubated with coverslips on parafilm.

In the case of organoids, the final volume of the reaction cocktail was adjusted to 100 µl per Eppendorf tube while wash and permeabilization volumes were adjusted to 200 µl.

In the case of gut-on-chip models, the volume scheme in **table 9.3** was used for permeabilization and washes. For incubation with the reaction cocktail, 25 µl of the cocktail was added to each top channel inlet and outlet and the plate manually rocked by placing it on a low angle, e.g., 5° and switching sides every 5 minutes.

10.4. Immunofluorescence staining

After staining for EdU, samples were either blocked overnight to begin the immunostaining protocol or stored in PBS at 4°C in aluminium foil for later.

10.4.1. 2D culture model

PBS was aspirated from all wells and coverslips incubated for an hour at room temperature or overnight at 4°C with blocking buffer comprising 3% BSA in 0.2% PBS-Triton X-100 according to volume scheme in **table 8.2**. If the coverslips were already stained for EdU, the plates were covered with aluminium foil while blocking to protect from light.

After blocking, coverslips were removed from the plate wells and incubated with primary antibodies as described in **table 9.4** on parafilm (50 µl per coverslip) for an hour at room temperature away from light.

Primary antibody	Species	Dilution in blocking buffer	Product code
ZO-1	rabbit polyclonal	1:50	Thermo, 61-7300
acetylated α-tubulin	mouse monoclonal	1:1000	Sigma, T6199-100UL
$p21^{Waf1/Cip1}$	rabbit monoclonal	1:500	CST, 2947T
p53	mouse monoclonal	1:1000	CST, 2524T
LYZ	mouse monoclonal	1:100	Invitrogen, MA182873
γH2AX	mouse monoclonal	1:1000	Merck, 05-636
γH2AX	rabbit monoclonal	1:1000	CST, 9718T
Secondary antibody	**Species**	**Dilution in blocking buffer**	**Product code**
anti-mouse 488 IgG, Alexa Fluor	Donkey	1:500	Invitrogen A21202
anti-rabbit 568 IgG, Alexa Fluor	Donkey	1:500	Invitrogen A11036
anti-mouse 647 IgG, Alexa Fluor	Goat	1:500	Invitrogen A-21240

Table 9.4 Primary and secondary antibodies used for immunostaining.

After incubation with primaries, coverslips were dipped in PBS twice, placed on a paper towel to soak up excess liquid, then placed on fresh parafilm containing 50 µl of secondary antibodies (**Table 9.4**) and 5 µg/ml DAPI (Sigma-Aldrich, D9542-10MG) for 30 minutes at room temperature away from light.

After incubation with secondaries, coverslips were dipped in PBS twice, placed on a paper towel to soak up excess liquid, then mounted on glass slides with 5 µl of Vactashield per coverslip (Vector Lab, H1200) and sealed with nail varnish. Glass slides were stored at 4°C protected from light for up to two months.

10.4.2. 3D gut-on-chip model

PBS was aspirated from all wells and tubes incubated with blocking buffer comprising 2% FBS, 2% BSA and 0.2% Triton X-100 in PBS for 45 minutes at room temperature or overnight at 4°C for optimal results, according to volume scheme in **table 9.3**. If the tubes were already stained for EdU, plates were covered with aluminium foil while blocking to protect from light.

The blocking solution was then aspirated and replaced with primary antibodies (**Table 9.4**) by dispensing 25 µl into each inlet and outlet. The antibodies were incubated with the tubes overnight at 4°C away from light, or at least two hours at room temperature away from light and while rocking the plate manually by placing it on a low angle, e.g., 5° and switching sides every 5 minutes.

After incubation with primaries, chips were washed with PBS for five minutes using volume scheme in **table 9.3**, then incubated with secondary antibodies (**Table 9.4**) and 5 µg/ml DAPI for 30 minutes at room temperature away from light while rocking the plate manually.

After incubation with secondaries, chips were washed with PBS for five minutes using volume scheme in **table 9.3**, refilled with 50 µl PBS in all inlets and outlets and stored at 4°C away from light for up to two months.

10.4.3. 3D colon organoid model

PBS was aspirated from all Eppendorfs and organoids incubated with 200 µl blocking buffer comprising 3% BSA and 0.2% Triton X-100 in PBS for an hour at room temperature or overnight at 4°C for optimal results. If the organoids were already stained for EdU, Eppendorfs were covered with aluminium foil while blocking to protect from light.

The blocking solution was then gently aspirated after the organoids sedimented at the bottom and replaced with 200 µl of primary antibodies (**Table 9.4**) overnight at 4°C away from light.

The next day, organoids were washed with 200 µl PBS twice by allowing them to sediment to the bottom of the Eppendorf tube before gently aspirating the supernatant, then incubated with 200 µl of secondary antibodies (**Table 9.4**) and 5 µg/ml DAPI for 2 hours at room temperature away from light. During this time, Mowiol embedding medium was recovered from -20°C and warmed to 37°C.

After incubation with secondaries, organoids were washed with PBS twice then mounted on glass slides with Mowiol embedding medium comprising 24% (w/v) Glycerol (Sigma-Aldrich, G5516), 9.6% (w/v) Mowiol 4-88 (Sigma-Aldrich, 81381), 0.1 M Tris-Cl (Roche, 10812846001) and 2.5% (w/v) DABCO (Sigma-Aldrich, D27802) in distilled water. Slides were incubated at 37°C for at least an hour or overnight at 4°C to allow the Mowiol to solidify completely.

10.5. RNA extraction and sequencing

Caco-2 cells were seeded at a density of 1×10^5 cells per well in a 6-well plate and intoxicated as described in **section 8.5.1**. After 48 hours, cells were washed with PBS, scraped in 1 ml of PBS and centrifuged at 250 RCF for five minutes. Cell pellets were then stored at -80°C for RNA extraction later.

3D Caco-2 tubes were grown as described in **section 8.2.4.** and intoxicated as described in **section 8.5.1.** After 48 hours, tubes were lysed using the RNASpin Mini kit lysis buffer supplemented with 1% BME. To do this, 35 µl of the buffer was added to the top channel inlet, and 15 µl to the top channel outlet. After 30 to 60 seconds, the lysate was pooled from four chips for each sample and topped up with more lysis buffer to reach a final volume of 350 µl per sample. All samples were immediately stored at -80°C for RNA extraction later.

RNA isolation was performed using the RNASpin Mini kit (Cytiva, 25-0500-71) and eluted in 30 µl of nuclease-free water. 5 µl from this was used for quantification or quality control purposes and the rest of the volume immediately stored at -80°C.

RNA was quantified using the Nanodrop Lite spectrophotometer (ND-LITE-PR, Thermo Fisher Scientific).

Library preparation (polyA enrichment), mRNA sequencing and quantification analyses were performed by Novogene Europe using the Illumina sequencing platform for paired end library fragments with read lengths of 150 base pairs (Q30≥85%).

10.6. Immunoblotting

10.6.1. Preparing lysates

Caco-2 cells were seeded at a density of 2×10^5 cells per well in a 6-well plate and treated as described in **sections 8.5.1**, **8.6** and **8.7**. After 48 hours, cells were washed with PBS, scraped in 1 ml of PBS and measured on a spectrophotometer, after which the samples were centrifuged at 2000 RPM for five minutes and the supernatant discarded. The $O.D_{600}$ reading for each sample was multiplied by 250 to determine the volume (µl) of sample buffer required for resuspending the cell pellets.

Sample buffer was prepared using 50 mM Tris (pH 6.8), 8 M Urea, 2% SDS, 0.3% Bromophenol blue and 1% BME. Cell pellets resuspended in sample buffer were stored at -20°C for not more than a year.

10.6.2. Preparing protein gels

Protein gels were cast using BioRad Mini PROTEAN Tetra Cell Casting Stand Clamps (1658050) for SDS-PAGE. Essentially, glass plates were first chosen as required (**Table 9.5**), cleaned with 70% IMS, then dried and assembled on the casting apparatus. The resolving gel was cast first by mixing 0.1% (w/v) of APS (Melford, A1512) with 5 ml of 9% Bis-Tris acrylamide SDS buffer pre-prepared using the recipe in **table 9.6**. Next, 0.1% (v/v) of TEMED (Sigma-Aldrich, T9281) was added in and the mixture was then carefully dispensed into the cast without creating air bubbles to polymerize for 15 minutes at room temperature. Isopropanol was used in case any air bubbles were present and discarded after the gel solidified.

Required thickness (mm)	Number of wells	Well capacity (µl)
1 (BioRad, 1653311)	15	20
	10	30
1.5 (BioRad, 1653312)	10	50

Table 9.5 Plate types for casting protein gels.

Stacking gel was prepared in the same manner to a final volume of 2.5 ml using 5% Bis-Tris acrylamide SDS buffer this time (**Table 9.6**), and dispensed over the solidified resolving gel. A gel comb was inserted immediately between the plates and the stacking gel allowed to polymerize for 15 minutes at room temperature.

Once the stacking gel had set, the sandwiched plates were removed from the casting apparatus while keeping the gel comb intact, and stored at 4°C in damp paper towels to prevent drying.

9% Bis-Tris acrylamide SDS buffer recipe for resolving gel (storage at 4°C)		
Reagent	**Volume (ml)**	**Final concentration**
37.5:1 (40%) acrylamide/Bis solution (1610148)	22.5	9%
2.5 M Bis-Tris pH 6.5	14.25	356 mM
20% SDS	0.5	0.1%
MQ water	62.75	62.75%
5% Bis-Tris acrylamide SDS buffer recipe for stacking gel (storage at 4°C)		
Reagent	**Volume (ml)**	**Final concentration**
29:1 (30%) acrylamide/Bis solution (1610156)	16.6	5%
2.5 M Bis-Tris pH 6.5	14.25	356 mM
20% SDS	0.5	0.1%
MQ water	68.65	68.65%

Table 9.6 Recipes for a 100 ml solution of stacking or resolving gel buffer.

10.6.3. SDS-PAGE

Cell lysates were recovered from -20°C and heated to 95°C for 10 minutes, after which they were centrifuged at 13,000 RPM for 10 seconds. Protein gels were set up in the Mini-PROTEAN Tetra System (Bio-RAD) containing MES buffer (Life Technologies, NP0001) and the gel comb was removed to access the wells. Once lysates and a protein ladder (PageRuler Plus Prestained Protein Ladder, Thermo Scientific, #26619) were loaded, the apparatus was run at 40 mA per gel.

10.6.4. Protein transfer

Once lysates reached the bottom of the protein gel, the gel was recovered from the plates and placed in transfer buffer containing 20mM Tris, 150 mM Glycine and 20% v/v methanol (Sigma, 900658). PVDF membranes were cut to fit the size of the gel and activated by placing in 100% methanol, after which they were sandwiched with the gel, sponges and filter paper in a sandwich pad and set up in the same Tetra System with transfer buffer filled to the brim. The apparatus was run at 400 mA for 80 minutes on ice or 20-22 mV overnight (10 to 12 hours).

For transferring proteins smaller than 60 kDa the Trans-Blot Turbo Transfer System (Bio-Rad, 1704150) was used according to manufacturer's instructions.

Transfer efficiency was tested by dipping the membrane in Ponceau S solution (Sigma-Aldrich, P7170). The solution was washed off by gently swishing the membrane in TBS (Millipore, 524750-1EA).

10.6.5. Immunoblotting

Membranes were incubated with blocking buffer containing 5% milk (Tenak, A08300500) and 0.1% Tween 20 (Sigma-Aldrich, P1379) in TBS for an hour at room temperature or overnight at 4°C. Primary antibodies were diluted in blocking buffer (**Table 9.7**) and incubated with the membrane overnight at 4°C. The membrane was washed thrice with TBS containing 0.1% Tween 20 (5 minutes each) the next day, incubated with secondary antibodies in blocking buffer (**Table 9.7**) for an hour at room temperature, then washed thrice with 0.1% Tween 20 in TBS before storing at 4°C in

TBS. Images were acquired using the OdysseySa Li-Cor scanner at a resolution of 200 µm and processed using Image Studio Lite v5.2.5.

Primary antibody	Species	Dilution in blocking buffer	Product code
phospho-CHK2	rabbit monoclonal	1:500	2197
p21$^{Waf1/Cip1}$	rabbit monoclonal	1:500	CST, 2947T
APOL3	rabbit polyclonal	1:500	ABclonal, A13840
IFIT1	rabbit polyclonal	1:1000	Invitrogen, PA3-848
phospho-Rb$^{Ser807/811}$	rabbit monoclonal	1:500	CST, 8516T
α-tubulin	mouse monoclonal	1:500	Abcam, ab7291
γH2AX	rabbit monoclonal	1:1000	CST, 9718T
HSP90	mouse monoclonal	1:1000	NovusBio, NB100-1972
Secondary antibody	**Species**	**Dilution in blocking buffer**	**Product code**
IRDye® 800CW anti-Mouse IgG	Donkey	Licor 926-32210	1:10000
IRDye® 680RD anti-Rabbit IgG	Donkey	Licor 926-68071	1:10000

Table 9.7 Primary and secondary antibodies used for immunoblotting.

11. Microscopy

Fixed 2D cell culture samples were imaged using the Nikon Wide-field Live-Cell system comprising the Inverted Ti eclipse, an Andor Zyla sCMOS camera (2560 x 2160; 6.5 µm pixels) and an NIS-Elements acquisition software. Plan Fluor 40x oil (NA 1.3) objective was used with Quad emission filters for SpectraX LED excitation wavelengths of 395 nm, 470 nm, 561 nm and 640 nm.

Fixed 3D samples were imaged on the Nikon A1 Confocal system using a CFI Plan Fluor 10x (NA 0.3) objective with emission filters for excitation wavelengths of 405 nm, 488 nm, 561 nm and 640 nm.

Images were processed using custom Macros scripts on Fiji and quantified using custom pipelines generated on Cell Profiler. All data was assembled on Adobe Illustrator 2022.

12. Statistics

Statistical analyses were performed on GraphPad Prism 9 using means of technical replicates or biological replicates (as indicated in the figure legends) and graphs assembled on Adobe Illustrator 2022. Asterisks indicate significance where * is $p<0.05$, ** is $p<0.01$, *** is $p<0.001$ and **** is $p<0.0001$.

Bibliography

1. Abbas, T. and A. Dutta (2009). "p21 in cancer: intricate networks and multiple activities." Nat Rev Cancer 9(6): 400-414.

2. Abuetabh, Y., *et al*. (2022). "DNA damage response revisited: the p53 family and its regulators provide endless cancer therapy opportunities." Exp Mol Med 54(10): 1658-1669.

3. Agbor, T. A. and McCormick, B. A. (2011). “*Salmonella* effectors: important players modulating host cell function during infection.” Cell Microbiol, 13, 1858-69.

4. Ahmed, D., *et al*. (2013). "Epigenetic and genetic features of 24 colon cancer cell lines." Oncogenesis 2(9): e71.

5. Alphonse, N., *et al*. (2021). "Interferons: Tug of War Between Bacteria and Their Host." Front Cell Infect Microbiol 11: 624094.

6. Andrews, J. R. and E. T. Ryan (2015). "Diagnostics for invasive *Salmonella* infections: Current challenges and future directions." Vaccine 33 Suppl 3(0 3): C8-15.

7. Barrila, J., *et al*. (2017). "Three-dimensional organotypic co-culture model of intestinal epithelial cells and macrophages to study *Salmonella* enterica colonization patterns." NPJ Microgravity 3: 10.

8. Batra, S., *et al*. (2023). “A review on cyclin-dependent kinase 5: An emerging drug target for neurodegenerative diseases.” International journal of biological macromolecules, 230(123259).

9. Bauernfeind, F. G., *et al*. (2009). “Cutting edge: NF-kappaB activating pattern recognition and cytokine receptors license NLRP3 inflammasome activation by regulating NLRP3 expression.” J Immunol, 183, 787-91.

10. Beaurivage, C., *et al*. (2020). "Development of a human primary gut-on-a-chip to model inflammatory processes." Sci Rep 10(1): 21475.

11. Beddoe, T., *et al*. (2010). “Structure, biological functions and applications of the AB5 toxins.” Trends Biochem Sci, 35, 411-8.

12. Bell, A., et al. (2023). "Biochemical and structural basis of sialic acid utilization by gut microbes." J Biol Chem 299(3): 102989.

13. Bellett, G., *et al*. (2009). “Microtubule plus-end and minus-end capture at adherens junctions is involved in the assembly of apico-basal arrays in polarised epithelial cells.” Cell Motil Cytoskeleton, 66(10), 893-908.

14. Beuzon, C. R., *et al*. (2002). "Growth and killing of a *Salmonella* enterica serovar Typhimurium sifA mutant strain in the cytosol of different host cell lines." Microbiology (Reading) 148(Pt 9): 2705-2715.

15. Beuzón, C. R., Salcedo, S. P. & Holden, D. W. Growth and killing of a Salmonella enterica serovar Typhimurium sifA mutant strain in the cytosol of different host cell lines. Microbiology (Reading, Engl) 148, 2705–2715 (2002).

16. Bierschenk, D., *et al*. (2017). "*Salmonella*-induced inflammasome activation in humans." Mol Immunol 86: 38-43.

17. Blazie, S. M., *et al*. (2015). "Comparative RNA-Seq analysis reveals pervasive tissue-specific alternative polyadenylation in Caenorhabditis elegans intestine and muscles." BMC Biol 13: 4.

18. Blazkova, H., *et al*. (2010). “Bacterial intoxication evokes cellular senescence with persistent DNA damage and cytokine signalling.” J Cell Mol Med, 14, 357-67.

19. Boxx, G. M. and G. Cheng (2016). "The Roles of Type I Interferon in Bacterial Infection." Cell Host Microbe 19(6): 760-769.

20. Broz, P. and Dixit, V. M. (2016). “Inflammasomes: mechanism of assembly, regulation and signalling.” Nat Rev Immunol, 16, 407-20.

21. Broz, P. and Monack, D. M. (2013). “Newly described pattern recognition receptors team up against intracellular pathogens.” Nat Rev Immunol, 13, 551-65.

22. Burma, S., *et al*. (2001). “ATM phosphorylates histone H2AX in response to DNA double-strand breaks.” J Biol Chem, 276, 42462-7.

23. Carden, S., *et al*. (2015). “Non-typhoidal *Salmonella* Typhimurium ST313 isolates that cause bacteremia in humans stimulate less inflammasome activation than ST19 isolates associated with gastroenteritis.” Pathog Dis, 73.

24. Chang, S. J., et al. (2019). "Unique features in the intracellular transport of typhoid toxin revealed by a genome-wide screen." PLoS Pathog 15(4): e1007704.

25. Chang, S. J., J. Song and J. E. Galan (2016). "Receptor-Mediated Sorting of Typhoid Toxin during Its Export from Salmonella Typhi-Infected Cells." Cell Host Microbe 20(5): 682-689.

26. Chiou, S. J., *et al*. (2021). "The Double-Edged Sword of Beta2-Microglobulin in Antibacterial Properties and Amyloid Fibril-Mediated Cytotoxicity." Int J Mol Sci 22(12).

27. Chong, A., *et al*. (2017). “The Role of Typhoid Toxin in *Salmonella* Typhi Virulence.” Yale J Biol Med, 90, 283-290.

28. Chou, H. H., et al. (2002). "Inactivation of CMP-N-acetylneuraminic acid hydroxylase occurred prior to brain expansion during human evolution." Proc Natl Acad Sci U S A 99(18): 11736-11741.

29. Cimprich, K. A. and Cortez, D. (2008). “ATR: an essential regulator of genome integrity.” Nat Rev Mol Cell Biol, 9, 616-27.

30. Coppe, J. P., *et al*. (2006). “Secretion of vascular endothelial growth factor by primary human fibroblasts at senescence.” J Biol Chem, 281, 29568-74.

31. Coppe, J. P., *et al*. (2008). “Senescence-associated secretory phenotypes reveal cell-nonautonomous functions of oncogenic RAS and the p53 tumor suppressor.” PLoS Biol, 6, 2853-68.

32. Crump, J. A., *et al*. (2015). "Epidemiology, Clinical Presentation, Laboratory Diagnosis, Antimicrobial Resistance, and Antimicrobial Management of Invasive *Salmonella* Infections." Clin Microbiol Rev 28(4): 901-937.

33. Dalmasso, G., *et al*. (2014). “The bacterial genotoxin colibactin promotes colon tumor growth by modifying the tumor microenvironment.” Gut Microbes, 5, 675-80.

34. Dang, E. V., *et al*. (2017). "Oxysterol Restraint of Cholesterol Synthesis Prevents AIM2 Inflammasome Activation." Cell 171(5): 1057-1071 e1011.

35. de Vasconcelos, N., *et al*. (2018). “Single-cell analysis of pyroptosis dynamics reveals conserved GSDMD-mediated subcellular events that precede plasma membrane rupture.” Cell Death & Differentiation, 26, 146-161.

36. Decout, A., *et al*. (2021). "The cGAS-STING pathway as a therapeutic target in inflammatory diseases." Nat Rev Immunol 21(9): 548-569.

37. Del Bel Belluz, L., *et al*. (2016). “The Typhoid Toxin Promotes Host Survival and the Establishment of a Persistent Asymptomatic Infection.” PLoS Pathog, 12, e1005528.

38. den Bakker, H. C., *et al*. (2011). “Genome sequencing reveals diversification of virulence factor content and possible host adaptation in distinct subpopulations of *Salmonella enterica*.” BMC Genomics, 12, 425.

39. Deng, L., *et al*. (2014). “Host adaptation of a bacterial toxin from the human pathogen *Salmonella* Typhi.” Cell, 159(6):1290–1299.

40. Dhaliwal, W., *et al*. (2003). "Intestinal defensin gene expression in human populations." Mol Immunol 40(7): 469-475.

41. Dogterom M. and Koenderink G. H. (2019). “Actin-microtubule crosstalk in cell biology.” Nat Rev Mol Cell Biol, 20(1), 38-54.

42. Dougan, G. and Baker, S. (2014). “*Salmonella enterica* serovar Typhi and the pathogenesis of typhoid fever.” Annu Rev Microbiol, 68, 317-36.

43. Drost, J., *et al*. (2015). "Sequential cancer mutations in cultured human intestinal stem cells." Nature 521(7550): 43-47.

44. Dunphy, G., *et al*. (2018). "Non-canonical Activation of the DNA Sensing Adaptor STING by ATM and IFI16 Mediates NF-kappaB Signaling after Nuclear DNA Damage." Mol Cell 71(5): 745-760 e745.

45. Edmondson, R., *et al*. (2014). “Three-dimensional cell culture systems and their applications in drug discovery and cell-based biosensors.” Assay Drug Dev Technol, 12, 207-18.

46. ElGhazaly, M., *et al*. (2023). "Typhoid toxin hijacks Wnt5a to establish host senescence and *Salmonella* infection." Cell Rep 42(10): 113181.

47. Engeland, K. (2022). "Cell cycle regulation: p53-p21-RB signaling." Cell Death Differ 29(5): 946-960.

48. Erlich, Y., *et al*. (2008). "Alta-Cyclic: a self-optimizing base caller for next-generation sequencing." Nat Methods 5(8): 679-682.

49. Fabrega, A. and J. Vila (2013). "*Salmonella enterica* serovar Typhimurium skills to succeed in the host: virulence and regulation." Clin Microbiol Rev 26(2): 308-341.

50. Fagundes, R. and L. K. Teixeira (2021). “Cyclin E/CDK2: DNA Replication, Replication Stress and Genomic Instability.” Front Cell Dev Biol 9: 774845.

51. Fedor, Y., *et al*. (2013). “From single-strand breaks to double-strand breaks during S-phase: a new mode of action of the Escherichia coli Cytolethal Distending Toxin.” Cell Microbiol, 15, 1-15.

52. Feltrin, S., *et al*. (2020). "Sterol synthesis pathway inhibition as a target for cancer treatment." Cancer Lett 493: 19-30.

53. Finlay, B. B. and Brumell, J. H. (2000). “*Salmonella* interactions with host cells: in vitro to in vivo.” Philos Trans R Soc Lond B Biol Sci, 355, 623-31.

54. Fu, J., *et al*. (2023). "Mechanisms and regulation of defensins in host defense." Signal Transduct Target Ther 8(1): 300.

55. Galán, J. E. (2016). "Typhoid toxin provides a window into typhoid fever and the biology of *Salmonella* Typhi." Proc Natl Acad Sci U S A 113(23): 6338-6344.

56. Galanos, P., *et al*. (2016). "Chronic p53-independent p21 expression causes genomic instability by deregulating replication licensing." Nat Cell Biol 18(7): 777-789.

57. Gal-Mor, O. (2019). “Persistent Infection and Long-Term Carriage of Typhoidal and Nontyphoidal *Salmonellae*.” Clin Microbiol Rev, 32.

58. Gal-Mor, O., Boyle, E. C. and Grassl, G. A. (2014). “Same species, different diseases: how and why typhoidal and non-typhoidal *Salmonella enterica* serovars differ.” Front Microbiol, 5, 391.

59. Gal-Mor, O., *et al*. (2014). "Same species, different diseases: how and why typhoidal and non-typhoidal *Salmonella enterica* serovars differ." Front Microbiol 5: 391.

60. Gasem, M. H., *et al*. (1995). "Culture of *Salmonella* Typhi and *Salmonella* Paratyphi from blood and bone marrow in suspected typhoid fever." Trop Geogr Med 47(4): 164-167.

61. Gaudet, R. G., *et al.* (2021). "A human apolipoprotein L with detergent-like activity kills intracellular pathogens." Science 373(6552).

62. Geiser, P., *et al*. (2021). "*Salmonella enterica* Serovar Typhimurium Exploits Cycling through Epithelial Cells To Colonize Human and Murine Enteroids." mBio 12(1).

63. Giannella, R. A. (1996). “*Salmonella*.” In: TH & BARON, S. (eds.) Medical Microbiology. Galveston (TX).

64. Gibani, M. M., *et al*. (2019). “Investigation of the role of typhoid toxin in acute typhoid fever in a human challenge model.” Nat Med, 25, 1082-1088.

65. Gilman, R. H., *et al*. (1975). "Relative efficacy of blood, urine, rectal swab, bone-marrow, and rose-spot cultures for recovery of *Salmonella* Typhi in typhoid fever." Lancet 1(7918): 1211-1213.

66. Guen, V. J., *et al*. (2017). "The awakening of the CDK10/Cyclin M protein kinase." Oncotarget 8(30): 50174-50186.

67. Guerra, L., *et al*. (2011). “The biology of the cytolethal distending toxins.” Toxins (Basel), 3, 172-90.

68. Guidi, R. *et al*. (2013) “*Salmonella enterica* delivers its genotoxin through outer membrane vesicles secreted from infected cells.” Cell Microbiol 15, 2034–2050

69. Guidi, R., *et al*. (2013). “Chronic exposure to the cytolethal distending toxins of Gram-negative bacteria promotes genomic instability and altered DNA damage response.” Cell Microbiol, 15, 98-113.

70. Gut, A. M., *et al*. (2018). "*Salmonella* infection - prevention and treatment by antibiotics and probiotic yeasts: a review." Microbiology (Reading) 164(11): 1327-1344.

71. Haghjoo, E. and Galán, J. E. (2004). “*Salmonella* Typhi encodes a functional cytolethal distending toxin that is delivered into host cells by a bacterial-internalization pathway.” Proc Natl Acad Sci U S A, 101, 4614-9.

72. Hapfelmeier, S., et al. (2005). "The Salmonella pathogenicity island (SPI)-2 and SPI-1 type III secretion systems allow Salmonella serovar typhimurium to trigger colitis via MyD88-dependent and MyD88-independent mechanisms." J Immunol 174(3): 1675-1685.

73. Hardt, W. D., *et al*. (1998). "*S*. Typhimurium encodes an activator of Rho GTPases that induces membrane ruffling and nuclear responses in host cells." Cell 93(5): 815-826.

74. Haselbeck, A. H., *et al*. (2017). “Current perspectives on invasive nontyphoidal *Salmonella* disease.” Curr Opin Infect Dis, 30, 498-503.

75. Hatzmann, F. M., *et al*. (2021). "Quiescence, Stemness and Adipogenic Differentiation Capacity in Human DLK1(-)/CD34(+)/CD24(+) Adipose Stem/Progenitor Cells." Cells 10(2).

76. He, Y., Yin, X., Dong, J., Yang, Q., Wu, Y., & Gong, Z. (2021). Transcriptome Analysis of Caco-2 Cells upon the Exposure of Mycotoxin Deoxynivalenol and Its Acetylated Derivatives. Toxins, 13(2), 167.

77. Hedlund, M., et al. (2007). "N-glycolylneuraminic acid deficiency in mice: implications for human biology and evolution." Mol Cell Biol 27(12): 4340-4346.

78. Henley, S. A. and F. A. Dick (2012). "The retinoblastoma family of proteins and their regulatory functions in the mammalian cell division cycle." Cell Div 7(1): 10.

79. Holch, A., *et al*. (2020). "Respiratory ss-2-Microglobulin exerts pH dependent antimicrobial activity." Virulence 11(1): 1402-1414.

80. Hume, S., *et al*. (2020). “A unified model for the G1/S cell cycle transition.” Nucleic Acids Res 48(22), 12483-12501.

81. Ibler, A. E. M., *et al*. (2019). “Typhoid toxin exhausts the RPA response to DNA replication stress driving senescence and *Salmonella* infection.” Nat Commun, 10, 4040.

82. Illumina. (2023) Sequencing quality scores. Available at: https://www.illumina.com/science/technology/next-generation-sequencing/plan-experiments/quality-scores.html (Accessed: 26 October 2023).

83. Illumina. (2023) Sequencing Technology | Sequencing by synthesis. Available at: https://emea.illumina.com/science/technology/next-generation-sequencing/sequencing-technology.html (Accessed: 26 October 2023).

84. Isaacs, A. and Lindenmann, J. (1988) 'Virus Interference: I. The Interferon.' CA: A Cancer Journal for Clinicians, 38(5), pp. 280–290.

85. Ivashkiv, L. B. (2018). "IFNgamma: signalling, epigenetics and roles in immunity, metabolism, disease and cancer immunotherapy." Nat Rev Immunol 18(9): 545-558.

86. Jazayeri, A., *et al*. (2006). "ATM- and cell cycle-dependent regulation of ATR in response to DNA double-strand breaks." Nat Cell Biol, 8, 37-45.

87. Jiang, L., *et al*. (2011). "Synthetic spike-in standards for RNA-seq experiments." Genome Res 21(9): 1543-1551.

88. Jin, C., *et al*. (2017). "Efficacy and immunogenicity of a Vi-tetanus toxoid conjugate vaccine in the prevention of typhoid fever using a controlled human infection model of *Salmonella* Typhi: a randomised controlled, phase 2b trial." Lancet 390(10111): 2472-2480.

89. Ka, N. L., *et al*. (2021). "IFI16 inhibits DNA repair that potentiates type-I interferon-induced antitumor effects in triple negative breast cancer." Cell Rep 37(12): 110138.

90. Kent, L. N. and G. Leone (2019). "The broken cycle: E2F dysfunction in cancer." Nat Rev Cancer 19(6): 326-338.

91. Knodler, L. A., *et al*. (2010). "Dissemination of invasive *Salmonella* via bacterial-induced extrusion of mucosal epithelia." Proc Natl Acad Sci U S A 107(41): 17733-17738.

92. Kombade, S., and Kaur, N. (2021). “Pathogenicity Island in *Salmonella*.” IntechOpen. doi: 10.5772/intechopen.96443

93. Kortmann, J., *et al*. (2015). “Cutting Edge: Inflammasome Activation in Primary Human Macrophages Is Dependent on Flagellin.” J Immunol, 195, 815-9.

94. Kovalchuk, I., *et al*. (2013). “Genomic instability in liver cells caused by an LPS-induced bystander-like effect.” PLoS One, 8, e67342.

95. Kreienkamp, R., *et al*. (2018). "A Cell-Intrinsic Interferon-like Response Links Replication Stress to Cellular Aging Caused by Progerin." Cell Rep 22(8): 2006-2015.

96. Kumar, P. and R. Kumar (2017). "Enteric Fever." Indian J Pediatr 84(3): 227-230.

97. Lara-Tejero, M. and Galán, J. E. (2000). “A bacterial toxin that controls cell cycle progression as a deoxyribonuclease I-like protein.” Science, 290, 354-7.

98. Lara-Tejero, M. and J. E. Galán (2001). "CdtA, CdtB, and CdtC form a tripartite complex that is required for cytolethal distending toxin activity." Infect Immun 69(7): 4358-4365.

99. Lara-Tejero, M. and J. E. Galán (2002). "Cytolethal distending toxin: limited damage as a strategy to modulate cellular functions." Trends Microbiol 10(3): 147-152.

100. Lasry, A. and Ben-Neriah, Y. (2015). “Senescence-associated inflammatory responses: aging and cancer perspectives.” Trends Immunol, 36, 217-28.

101. Lee, S., *et al*. (2020). "*Salmonella* Typhoid Toxin PltB Subunit and Its Non-typhoidal *Salmonella* Ortholog Confer Differential Host Adaptation and Virulence." Cell Host Microbe 27(6): 937-949 e936.

102. Lees, E. A., *et al*. (2019). "Using Human Induced Pluripotent Stem Cell-derived Intestinal Organoids to Study and Modify Epithelial Cell Protection Against *Salmonella* and Other Pathogens." J Vis Exp(147).

103. Li, D. and M. Wu (2021). "Pattern recognition receptors in health and diseases." Signal Transduct Target Ther 6(1): 291.

104. Libby, S. J., et al. (2010). "Humanized nonobese diabetic-scid IL2rgammanull mice are susceptible to lethal Salmonella Typhi infection." Proc Natl Acad Sci U S A 107(35): 15589-15594.

105. Lim, S. and P. Kaldis (2013). "Cdks, cyclins and CKIs: roles beyond cell cycle regulation." Development 140(15): 3079-3093.

106. Liu, W., *et al*. (2017). "Cdk5 links with DNA damage response and cancer." Mol Cancer 16(1): 60.

107. Lorkowski, M., *et al*. (2014). "*Salmonella enterica* invasion of polarized epithelial cells is a highly cooperative effort." Infect Immun 82(6): 2657-2667.

108. Lueschow, S. R. and S. J. McElroy (2020). "The Paneth Cell: The Curator and Defender of the Immature Small Intestine." Front Immunol 11: 587.

109. Machado, L. R. and B. Ottolini (2015). "An evolutionary history of defensins: a role for copy number variation in maximizing host innate and adaptive immune responses." Front Immunol 6: 115.

110. Majowicz, S. E., *et al*. (2010). “The global burden of nontyphoidal *Salmonella* gastroenteritis.” Clin Infect Dis, 50, 882-9.

111. Man, S. M., *et al*. (2014). “Inflammasome activation causes dual recruitment of NLRC4 and NLRP3 to the same macromolecular complex.” Proc Natl Acad Sci U S A, 111, 7403-8.

112. Man, S. M., *et al*. (2015). "The transcription factor IRF1 and guanylate-binding proteins target activation of the AIM2 inflammasome by Francisella infection." Nat Immunol 16(5): 467-475.

113. Miao, E. A., *et al*. (2010). "Caspase-1-induced pyroptosis is an innate immune effector mechanism against intracellular bacteria." Nat Immunol 11(12): 1136-1142.

114. Miller, R. A., *et al*. (2018). “The Typhoid Toxin Produced by the Nontyphoidal *Salmonella enterica* Serotype Javiana Is Required for Induction of a DNA Damage Response In Vitro and Systemic Spread In Vivo.” mBio, 9.

115. Milligan, R., *et al*. (2018). "Vaccines for preventing typhoid fever." Cochrane Database Syst Rev 5(5): CD001261.

116. Misselwitz, B., *et al.* (2011). "Salmonella enterica serovar Typhimurium binds to HeLa cells via Fim-mediated reversible adhesion and irreversible type three secretion system 1-mediated docking." Infect Immun 79(1): 330-341.

117. Mitra, M., *et al*. (2016). "Efficacy and safety of vi-tetanus toxoid conjugated typhoid vaccine (PedaTyph) in Indian children: School based cluster randomized study." Hum Vaccin Immunother 12(4): 939-945.

118. Muñoz-Planillo, R., *et al*. (2013). “K(+) efflux is the common trigger of NLRP3 inflammasome activation by bacterial toxins and particulate matter.” Immunity, 38, 1142-53.

119. Natoli, M., *et al*. (2011). "Cell growing density affects the structural and functional properties of Caco-2 differentiated monolayer." J Cell Physiol 226(6): 1531-1543.

120. Naveed, M., *et al*. (2023). "Purification, Characterization and Bactericidal Action of Lysozyme, Isolated from Bacillus subtillis BSN314: A Disintegrating Effect of Lysozyme on Gram-Positive and Gram-Negative Bacteria." Molecules 28(3).

121. Nicolas, A., *et al.* (2021). "High throughput transepithelial electrical resistance (TEER) measurements on perfused membrane-free epithelia." Lab Chip 21(9): 1676-1685.

122. Nordahl, E. A., *et al*. (2004). "Activation of the complement system generates antibacterial peptides." Proc Natl Acad Sci U S A 101(48): 16879-16884.

123. Ohuchida, K., *et al*. (2004). “Radiation to stromal fibroblasts increases invasiveness of pancreatic cancer cells through tumor-stromal interactions.” Cancer Res, 64, 3215-22.

124. Oishi, Y. and Manabe, I. (2016). “Macrophages in age-related chronic inflammatory diseases.” NPJ Aging Mech Dis, 2, 16018.

125. Ookawa, K., *et al*. (2002). "Transcriptional activation of the MUC2 gene by p53." J Biol Chem 277(50): 48270-48275.

126. Panier, S. and Boulton, S. J. (2014). “Double-strand break repair: 53BP1 comes into focus.” Nat Rev Mol Cell Biol, 15, 7-18.

127. Parry, C. M., *et al*. (2002). "Typhoid fever." N Engl J Med 347(22): 1770-1782.

128. Phulphagar, K., *et al*. (2021). “Proteomics reveals distinct mechanisms regulating the release of cytokines and alarmins during pyroptosis.” Cell Rep, 34, 108826.

129. Pidugu, V. K., *et al*. (2019). "Emerging Functions of Human IFIT Proteins in Cancer." Front Mol Biosci 6: 148.

130. Pilgrim, C. R., *et al.* (2022). "A Review of Fetal Bovine Serum in the Culture of Mesenchymal Stromal Cells and Potential Alternatives for Veterinary Medicine." Front Vet Sci 9: 859025.

131. Pitzer, V.E. *et al*. (2014). “Predicting the Impact of Vaccination on the Transmission Dynamics of Typhoid in South Asia: A Mathematical Modeling Study.” PLoS Neglected Tropical Diseases, 8(1): e2642.

132. Platnich, J. M. and Muruve, D. A. (2019). “NOD-like receptors and inflammasomes: A review of their canonical and non-canonical signaling pathways.” Arch Biochem Biophys, 670, 4-14.

133. Polo, S. E. and Jackson, S. P. (2011). “Dynamics of DNA damage response proteins at DNA breaks: a focus on protein modifications.” Genes Dev, 25, 409-33.

134. Prabh, N. and C. Rodelsperger (2016). "Are orphan genes protein-coding, prediction artifacts, or non-coding RNAs?" BMC Bioinformatics 17(1): 226.

135. Prattichizzo, *et al*. (2016). “Senescence associated macrophages and "macroph-aging": are they pieces of the same puzzle?” Aging (Albany NY), 8, 3159-3160.

136. Qiao, W., *et al*. (2019). “Lipopolysaccharide-induced DNA damage response activates nuclear factor κB signalling pathway via GATA4 in dental pulp cells.” International Endodontic Journal, 52, 1704-1715.

137. Radoshevich, L., *et al*. (2015). "ISG15 counteracts Listeria monocytogenes infection." Elife 4.

138. Ramachandran, G., *et al*. (2015). “Invasive *Salmonella* Typhimurium ST313 with naturally attenuated flagellin elicits reduced inflammation and replicates within macrophages.” PLoS Negl Trop Dis, 9, e3394.

139. Rauch, I., *et al*. (2017). “NAIP-NLRC4 Inflammasomes Coordinate Intestinal Epithelial Cell Expulsion with Eicosanoid and IL-18 Release via Activation of Caspase-1 and -8.” Immunity, 46, 649-659.

140. Razavipour, S. F., *et al*. (2020). "p27 as a Transcriptional Regulator: New Roles in Development and Cancer." Cancer Res 80(17): 3451-3458.

141. Ribet, D. and Cossart, P. (2015). “How bacterial pathogens colonize their hosts and invade deeper tissues.” Microbes Infect, 17, 173-83.

142. Rodrigues N. R., *et al*. (1990). “p53 mutations in colorectal cancer.” Proc Natl Acad Sci U S A, 87(19), 7555-9.

143. Rossi, M. N. and F. Antonangeli (2015). "Cellular Response upon Stress: p57 Contribution to the Final Outcome." Mediators Inflamm 2015: 259325.

144. Sato, T., *et al*. (2009). "Single Lgr5 stem cells build crypt-villus structures in vitro without a mesenchymal niche." Nature 459(7244): 262-265.

145. Schnaar, R. L., R. Gerardy-Schahn and H. Hildebrandt (2014). "Sialic acids in the brain: gangliosides and polysialic acid in nervous system development, stability, disease, and regeneration." Physiol Rev 94(2): 461-518.

146. Schneider, W. M., *et al*. (2014). "Interferon-stimulated genes: a complex web of host defenses." Annu Rev Immunol 32: 513-545.

147. Scuron, M. D., *et al*. (2016). “The Cytolethal Distending Toxin Contributes to Microbial Virulence and Disease Pathogenesis by Acting As a Tri-Perditious Toxin.” Front Cell Infect Microbiol, 6, 168.

148. Secher, T., *et al*. (2013). “Escherichia coli producing colibactin triggers premature and transmissible senescence in mammalian cells.” PLoS One, 8, e77157.

149. Sellin, M. E., *et al*. (2014). "Epithelium-intrinsic NAIP/NLRC4 inflammasome drives infected enterocyte expulsion to restrict *Salmonella* replication in the intestinal mucosa." Cell Host Microbe 16(2): 237-248.

150. Sepe, L. P., *et al*. (2020). "Genotoxic Effect of *Salmonella* Paratyphi A Infection on Human Primary Gallbladder Cells." mBio 11(5).

151. Shakya, M., *et al*. (2019). "Phase 3 Efficacy Analysis of a Typhoid Conjugate Vaccine Trial in Nepal." N Engl J Med 381(23): 2209-2218.

152. Sharpless, N. E. and Sherr, C. J. (2015). “Forging a signature of in vivo senescence.” Nat Rev Cancer, 15, 397-408.

153. Shenker, B. J., *et al*. (2016). “The toxicity of the Aggregatibacter actinomycetemcomitans cytolethal distending toxin correlates with its phosphatidylinositol-3,4,5-triphosphate phosphatase activity.” Cell Microbiol, 18, 223-43.

154. Sherr, C. J. and J. M. Roberts (2004). “Living with or without cyclins and cyclin-dependent kinases.” Genes Dev 18(22): 2699-2711.

155. Shirahama, S., *et al*. (2020). "Long Non-coding RNAs Involved in Pathogenic Infection." Front Genet 11: 454.

156. Solier, S. and Pommier, Y. (2014). “The nuclear gamma-H2AX apoptotic ring: implications for cancers and autoimmune diseases.” Cell Mol Life Sci, 71, 2289-97.

157. Song, J., *et al.* (2010). "A mouse model for the human pathogen Salmonella typhi." Cell Host Microbe 8(4): 369-376.

158. Song, J., Gao, X. and Galán, J. E. (2013). “Structure and function of the *Salmonella* Typhi chimaeric A(2)B(5) typhoid toxin.” Nature, 499, 350-4.

159. Spano, S., *et al*. (2008). "Delivery of a *Salmonella* Typhi exotoxin from a host intracellular compartment." Cell Host Microbe 3(1): 30-38.

160. Stanaway, J., D., Parisi, A., *et al.,* (2019). “The global burden of non-typhoidal *Salmonella* invasive disease: a systematic analysis for the Global Burden of Disease Study 2017.” The Lancet Infectious Diseases, 19(12), pp.1312-1324. Doi: https://doi.org/10.1016/S1473-3099(19)30418-9.

161. Stanaway, J., D., Reiner, R., *et al.*, (2019). “The global burden of typhoid and paratyphoid fevers: a systematic analysis for the Global Burden of Disease Study 2017.” The Lancet Infectious Diseases, 19(4), pp.369-381. Doi: https://doi.org/10.1016/S1473-3099(18)30685-6.

162. Stewart, M. K. and Cookson, B. T. (2016). “Evasion and interference: intracellular pathogens modulate caspase-dependent inflammatory responses.” Nat Rev Microbiol, 14, 346-59.

163. Suarez, B., *et al*. (2020). "LncRNAs in the Type I Interferon Antiviral Response." Int J Mol Sci 21(17).

164. Tacconelli, E., *et al*. (2018). "Discovery, research, and development of new antibiotics: the WHO priority list of antibiotic-resistant bacteria and tuberculosis." Lancet Infect Dis 18(3): 318-327.

165. Takeuchi, A. (1967). "Electron microscope studies of experimental *Salmonella* infection. I. Penetration into the intestinal epithelium by *Salmonella* typhimurium." Am J Pathol 50(1): 109-136.

166. Thant, A. A., *et al*. (2008). "Role of caspases in 5-FU and selenium-induced growth inhibition of colorectal cancer cells." Anticancer Res 28(6A): 3579-3592.

167. Trietsch, S. J., *et al*. (2017). "Membrane-free culture and real-time barrier integrity assessment of perfused intestinal epithelium tubes." Nat Commun 8(1): 262.

168. Trimarchi, J. M. and J. A. Lees (2002). "Sibling rivalry in the E2F family." Nat Rev Mol Cell Biol 3(1): 11-20.

169. Turgeon, P., Murray, R. and Nesbitt, A. (2017). “Hospitalizations associated with salmonellosis among seniors in Canada, 2000-2010.” Epidemiol Infect, 145, 1527-1534.

170. Urban, N. and T. H. Cheung (2021). "Stem cell quiescence: the challenging path to activation." Development 148(3).

171. van Harten, R. M., *et al*. (2018). "Cathelicidins: Immunomodulatory Antimicrobials." Vaccines (Basel) 6(3).

172. Velge, P., *et al*. (2012). “Multiplicity of *Salmonella* entry mechanisms, a new paradigm for *Salmonella* pathogenesis.” Microbiologyopen, 1, 243-58.

173. Vladimer, G. I., *et al*. (2014). "IFITs: Emerging Roles as Key Anti-Viral Proteins." Front Immunol 5: 94.

174. Wain, J., *et al*. (2001). "Quantitation of bacteria in bone marrow from patients with typhoid fever: relationship between counts and clinical features." J Clin Microbiol 39(4): 1571-1576.

175. Wain, J., *et al*. (2015). “Typhoid fever.” Lancet, 385, 1136-45.

176. Walker, J., *et al*. (2023). "Assessing the global risk of typhoid outbreaks caused by extensively drug resistant *Salmonella* Typhi." Nat Commun 14(1): 6502.

177. Wang, Q., *et al*. (2023). "Targeting CDK1 in cancer: mechanisms and implications." NPJ Precis Oncol 7(1): 58.

178. Wang, X., *et al*. (2016). "Activation/Proliferation-associated Protein 2 (Caprin-2) Positively Regulates CDK14/Cyclin Y-mediated Lipoprotein Receptor-related Protein 5 and 6 (LRP5/6) Constitutive Phosphorylation." J Biol Chem 291(51): 26427-26434.

179. Wangdi, T., Winter, S. E. and Baumler, A. J. (2012). “Typhoid fever: "you can't hit what you can't see".” Gut Microbes, 3, 88-92.

180. Williams, W. M., *et al*. (2013). "Antimicrobial peptide beta-defensin-1 expression is upregulated in Alzheimer's brain." J Neuroinflammation 10: 127.

181. Winter, S. E., *et al*. (2014). “*Salmonella* enterica Serovar Typhi conceals the invasion-associated type three secretion system from the innate immune system by gene regulation.” PLoS Pathog, 10, e1004207.

182. Wold, M. S. (1997). “Replication protein A: a heterotrimeric, single-stranded DNA-binding protein required for eukaryotic DNA metabolism.” Annu Rev Biochem, 66, 61-92.

183. Wong, V. K., *et al*. (2015). “Phylogeographical analysis of the dominant multidrug-resistant H58 clade of *Salmonella* Typhi identifies inter- and intracontinental transmission events.” Nat Genet, 47, 632-9.

184. World Health Organization (2018). “Typhoid vaccines: WHO position paper – March 2018.” Weekly epidemiological record, doi:10.1186/1750-9378-2-15.Voir.

185. Yang, L., *et al*. (2004). "Cyclin L2, a novel RNA polymerase II-associated cyclin, is involved in pre-mRNA splicing and induces apoptosis of human hepatocellular carcinoma cells." J Biol Chem 279(12): 11639-11648.

186. Yang, Y. A., *et al*. (2018). "Why Is Eradicating Typhoid Fever So Challenging: Implications for Vaccine and Therapeutic Design." Vaccines (Basel) 6(3).

187. Yu, C. Y., *et al.* (2007). "A bipartite signal regulates the faithful delivery of apical domain marker podocalyxin/Gp135." Mol Biol Cell 18(5): 1710-1722.

188. Zellweger, R., *et al*. (2015). “Rad51-mediated replication fork reversal is a global response to genotoxic treatments in human cells.” Journal of Cell Biology, 208, 563-579.

189. Zhang, C., *et al*. (2019). "Down-regulation of CCNE1 expression suppresses cell proliferation and sensitizes gastric carcinoma cells to Cisplatin." Biosci Rep 39(6).

190. Zhang, W., *et al*. (2023). "The emerging roles of IFIT3 in antiviral innate immunity and cellular biology." J Med Virol 95(1): e28259.

191. Zhang, X., *et al*. (2011). "Cutting edge: Ku70 is a novel cytosolic DNA sensor that induces type III rather than type I IFN." J Immunol 186(8): 4541-4545.

192. Zhao, Y. and Shao, F. (2016). “Diverse mechanisms for inflammasome sensing of cytosolic bacteria and bacterial virulence.” Curr Opin Microbiol, 29, 37-42.

193. Zhao, Y., *et al*. (2011). “The NLRC4 inflammasome receptors for bacterial flagellin and type III secretion apparatus.” Nature, 477, 596-600.

194. Zhou, X., *et al*. (2013). "Interferon induced IFIT family genes in host antiviral defense." Int J Biol Sci 9(2): 200-208.

195. Zhou, Z., *et al*. (2020). "Granzyme A from cytotoxic lymphocytes cleaves GSDMB to trigger pyroptosis in target cells." Science 368(6494).

196. Ziegler, D. V., *et al*. (2024). "Cholesterol biosynthetic pathway induces cellular senescence through ERRalpha." NPJ Aging 10(1): 5.

197. Zito, G., *et al*. (2020). “Cellular Models and Assays to Study NLRP3 Inflammasome Biology.” Int J Mol Sci, 21.